Modeling Structural Brain Connectivity

Ambrosen, Karen Marie Sandø

Publication date:
2017

Document Version
Publisher's PDF, also known as Version of record

Modeling Structural Brain Connectivity

Karen Marie Sandø Ambrosen

Kongens Lyngby 2016

Technical University of Denmark
Department of Applied Mathematics and Computer Science
Richard Petersens Plads, building 324,
2800 Kongens Lyngby, Denmark
Phone +45 4525 3031
compute@compute.dtu.dk
www.compute.dtu.dk

Summary (English)

The human brain consists of a gigantic complex network of interconnected neurons. Together all these connections determine who we are, how we react and how we interpret the world. Knowledge about how the brain is connected can further our understanding of the brain's structural organization, help improve diagnosis, and potentially allow better treatment of a wide range of neurological disorders.

Tractography based on diffusion magnetic resonance imaging is a unique tool to estimate this "structural connectivity" of the brain non-invasively and *in vivo*. During the last decade, brain connectivity has increasingly been analyzed using graph theoretic measures adopted from network science and this characterization of the brain's structural connectivity has been shown to be useful for the classification of populations, such as healthy and diseased subjects. The structural connectivity of the brain estimated using tractography is, however, derived by integrating noisy estimates of the local fiber orientation in each voxel, entailing biases and limitations in the estimated connections and resulting in noisy graphs.

In this thesis, the ability of stochastic block models to extract the latent organization of structural brain connectivity graphs is investigated. It is found that both the stochastic block model and its non-parametric extension, the infinite relational model, are able to reliably extract a clustering that better accounts for structural connectivity than cortical atlases based solely upon surface morphology. Furthermore, a statistical prediction framework to quantify the ability of a cortical parcellation to account for structural connectivity is proposed. It is tested on two commonly used cortical atlases that are both based on surface

morphology, as well as on a recently proposed cortical parcellation by Glasser et al. (2016) that is based on both task and resting-state functional magnetic resonance imaging, cortical thickness and myelin. It is found that all three atlases capture the structural connectivity much better than random, but also that the parcellation based on multiple modalities is superior to those solely based on surface morphology.

The generation of structural brain connectivity graphs comprises a comprehensive processing pipeline, with various experimenter-defined parameters. The settings of these parameters are, however, unclear and this subjective aspect complicates the cross-comparison of studies investigating structural brain connectivity derived from tractography. Even though scan acquisition parameters, i.e. spatial resolution, angular resolution and b-value, are often discussed as possible factors influencing the final result, the impact of these factors on the derived structural connectivity graph has not yet been investigated. Herein, structural connectivity graphs, generated using different combinations of the three aforementioned acquisition parameters, are validated by comparison to a connectivity graph derived using invasive tracer injections in monkeys. It is found that the choice of acquisition parameters influences the derived structural connectivity graph and that higher angular resolution is always beneficial. Surprisingly, it is also found that higher spatial resolution does not improve the derived graph, but further investigation is needed to confirm this result.

Resumé (Danish)

Den humane hjerne består af et gigantisk netværk af forbundne nerveceller. Alle disse nerveforbindelser afgør tilsammen hvem vi er, hvordan vi reagerer og hvordan vi opfatter verden. Viden om hvordan hjernen er forbundet kan øge vores forståelse af hjernens strukturelle organisering, hjælpe med at forbedre diagnose og potentielt tillade bedre behandling af en lang række neorologiske sygdomme.

Traktografi baseret på diffusions-vægtet magnetisk resonans billeddannelse er et unikt redskab til at estimere hjernens strukturelle forbindelser non-invasivt og *in vivo*. Gennem det sidste årti har der været et stigende antal studier der analyserer hjernenetværk ved brug af graf teoretiske mål fra netværks teori. Karakterisering af hjernens strukturelle forbindelser har vist sig at være nyttig til at klassificere grupper, som for eksempel raske og syge. De strukturelle hjerne forbindelser, estimeret med traktografi, er imidlertid udledt fra støjfyldte estimater af den lokale fiber orientering i hver voxel. Dette påvirker og begrænser de estimerede forbindelser og resulterer i støjfyldte hjernenetværk.

I denne afhandling undersøges hvorvidt stokastiske blokmodeller er i stand til at udtrække den skjulte organisering i strukturelle hjernenetværk. Resultaterne viser at både den stokastiske blokmodel og dens ikke-parametriske forlængelse, *the infinite relational model*, er i stand til pålideligt at udtrække grupper der bedre beskriver hjernens strukturalle organisering end kortikale atlas udelukkende baseret på overflademorfologi. Endvidere præsenteres en statistisk prædiktiv metode til at kvantificere kortikale parcelleringers evne til at beskrive strukturelle hjerneforbindelser. Metoden er testet på to bredt anvendte kortikale atlas baseret på overflademorfologi, samt på en nylig foreslået parcellering af Glas-

ser et al. (2016), baseret på både *task* og *resting-state* funktional magnetisk resonans billeddannelse, cortex tykkelse og myelin. Resultaterne viser at alle tre atlas beskriver de strukturelle hjerneforbindelser meget bedre end en tilfældig parcellering, men også at parcelleringen baseret på flere modaliteter er bedre end dem baseret udelukkende på overflademorfologi.

Genereringen af strukturelle hjernenetværk består af en omfattende databehandlingsprocedure med mange forskellige parametre, der skal defineres af personen der genererer netværket. Dette subjektive aspekt komplicerer sammenligningen af resultater fra forskellige studier, der analyserer hjernenetværk baseret på traktografi. Selvom skanner specifikke parametre, såsom billedopløsning, antallet af diffusionsretninger og b-værdi, ofte nævnes som mulige faktorer der påvirker det endelige netværk, har effekten af dem endnu ikke været undersøgt. I denne afhandling sammenlignes strukturelle hjernenetværk genereret med forskellige kombinationer af de nævnte skannerparametre med et netværk genereret ved brug af sporstofinjektioner i aber. Vi finder at skannerparametrenes værdi har betydning for det genererede netværk og at flere diffusionsretninger altid er bedre. Overraskende finder vi, at højere billedopløsning ikke forbedrer det genererede netværk, men der kræves yderligere analyser for at beskræfte dette resultat.

Preface

This thesis was prepared partly at the department of Applied Mathematics and Computer Science, Technical University of Denmark (DTU Compute) and partly at the Danish Research Centre for Magnetic Resonance, Centre for Functional and Diagnostic Imaging and Research, Copenhagen University Hospital (DRCMR) in partial fulfilment of the requirements for acquiring the Ph.D. degree in engineering. The project was funded partly $\left(\frac{2}{3}\right)$ by a research grant from the Lundbeck Foundation given to Morten Mørup (grant no. R105-9813) and partly $\left(\frac{1}{3}\right)$ by DTU Compute. The project was carried out under the supervision of main supervisor Associate Professor Morten Mørup, DTU Compute, and co-supervisors Associate Professor Tim B. Dyrby, DRCMR and DTU Compute, and Associate Professor Mikkel N. Schmidt, DTU Compute.

The thesis deals with modelling of structural brain connectivity derived from tractography based on diffusion magnetic resonance imaging. The thesis consists of a summary report and a collection of two conference papers and two journal papers in preparation. The work was carried out between April 2013 and December 2016.

Lyngby, 15-December-2016

Karen Marie Sandø Ambrosen

Acknowledgements

I would like to thank my three supervisors Morten Mørup, Tim B. Dyrby and Mikkel N. Schmidt for guidance and discussions during the project. Without their help and support this work had not been possible.

Thanks to the Lundbeck Foundation and DTU Compute for co-funding this work. I received travel grants from the Otto Mønsted Foundation and funding for my external stay from the Otto Mønsted Foundation, the Augustinus Foundation and the the Oticon Foundation, which I am grateful for.

During my studies I visited the Computational Cognitive Neuroscience Lab, Department of Cognitive Artificial Intelligence, Donders Institute for Brain, Cognition and Behaviour, Radboud University for four months. I will like to thank Assistant Professor Marcel van Gerven for his invitation, hospitality and supervision as well as the rest of his group for making me feel welcome.

Thanks to all my collaborators; Kristoffer J. Albers, Matthew G. Liptrot, Tue Herlau, Max Hinne, Simon F. Eskildsen, Max Hinne, Marcel van Gerven, Henrik Lundell, Kristine Krug, Mikkel N. Schmidt, Tim B. Dyrby, and Morten Mørup. Thanks to the proofreaders; Matthew G. Liptrot, Tim B. Dyrby and Morten Mørup. In addition, thanks to all my colleagues in the Cognitive Systems Group at DTU Compute and at DRCMR, especially to all the members of the Microstructure and Plasticity Group (MAP).

A special thank to my husbond, Bjarne, for all his love and support, and to our son, Johannes. The two of you mean everything to me.

Manuscripts included in the thesis

Paper A

Ambrosen, K. S., Herlau, T., Dyrby, T. B., Schmidt, M. N., Mørup, M. (2013), 'Comparing Structural Brain Connectivity by the Infinite Relational Model', part of: Proceedings of the 3rd International Workshop on Pattern Recognition in Neuroimaging (PRNI 2013) (ISBN: 978-0-7695-5061-9), pages: 50-53, 2013, IEEE.
Presented at: 3rd International Workshop on Pattern Recognition in NeuroImaging (PRNI 2013), 2013, Philadelphia, PA
DOI: http://dx.doi.org/10.1109/PRNI.2013.22

Paper B

Ambrosen, K. S., Albers, K. J., Dyrby, T. B., Schmidt, M. N., Mørup, M. (2014), 'Nonparametric Bayesian Clustering of Structural Whole Brain Connectivity in Full Image Resolution', part of: Proceedings of the 4th International Workshop on Pattern Recognition in Neuroimaging (PRNI 2014) (ISBN: 978-1-4799-4149-0), 2014, IEEE.
Presented at: 4th International Workshop on Pattern Recognition in Neuroimaging (PRNI 2014), 2014, Tübingen

Paper C

Ambrosen, K. S.*, Albers, K. J.*, Liptrot, M. G., Dyrby, T. B., Schmidt, M. N., Mørup, M. (2016), 'Predictive Validation of Human Brain Parcellations', *in preparation*
** These authors contributed equally to the manuscript.*

Paper D

Ambrosen, K. S., Eskildsen, S. F., Hinne, M., Krug, K., Lundell, H., Schmidt, M. N., van Gerven, M. A. J., Mørup, M., Dyrby, T. B., 'Validation of Structural Brain Connectivity Networks', *in preparation*

Symbols and abbreviations

Abbreviations

ADC	Apparent diffusion coefficient
AUC	Area under curve
CC	Corpus callosum
CRP	Chinese restaurant process
dMRI	Diffusion weighted magnetic resonance imaging
DRCMR	Danish Research Centre for Magnetic Resonance
DT	Diffusion tensor
DTI	Diffusion tensor imaging
EPI	Echo-planar imaging
FA	Fractional anisotropy
FLNe	Extrinsic fraction of labeled neurons
fMRI	Functional magnetic resonance imaging
FSL	FMRIB Software Library
GM	Gray matter
HCP	Human Connectome Project
HCP_MMP1.0	Human Connectome Project Multi-Modal Parcellation
IRM	Infinite relational model
MCMC	Markov Chain Monte Carlo
MD	Mean diffusivity
MI	Mutual information
MRI	Magnetic resonance imaging
NMI	Normalized mutual information
pdf	Probability density function

PGSE	Pulsed gradient spin-echo
RF	Radio frequency
ROC	Receiver operating characteristic
SBM	Stochastic block model
SNR	Signal-to-noise ratio
SPM	Statistical Parametric Mapping
TE	Echo time
TR	Repetition time
VDM	Voxel displacement map
WM	White matter

Notation

x	Scalar
$\boldsymbol{x}$	Vector
x_i	i-th element of $\boldsymbol{x}$
$\boldsymbol{X}$	Matrix
X_{ij}	(i, j)-th element of $\boldsymbol{X}$

Fixed symbols

b	Diffusion encoding factor
Δ, t_d	Diffusion time
δ	Length of diffusion encoding gradient
G	Gradient strength
γ	Gyromagnetic ratio
D	Diffusion coefficient
$\lambda_{1,2,3}$	Eigenvalues
$\boldsymbol{A}$	Adjacency matrix
$\boldsymbol{A}^{(s)}$	Adjacency matrix for subject s
J	Number of nodes
K	Number of clusters
N^{+}_{lm}	Number of links between cluster l and m
N^{-}_{lm}	Number of non-links between cluster l and m
m_k	Number of nodes assigned to cluster k
$\boldsymbol{z}$	Cluster assignment vector
$\boldsymbol{z}_{\setminus i}$	Assignment of all nodes except node i

$\tilde{\boldsymbol{\alpha}}$	Hyperparameter for the Dirichlet distribution
α	Hyperparameter for the CRP
$\boldsymbol{\pi}$	Hyperparameter for the categorical distribution
β^+	Hyperparameter for the beta distribution
β^-	Hyperparameter for the beta distribution
$\boldsymbol{\eta}$	Cluster link probability matrix
$\boldsymbol{\theta}_j$	Relative connectivity probabilities
$\boldsymbol{V}$	Size of source regions
N_j	Total number of connections between all source regions and target region j
κ_j	Scaling factor
$\boldsymbol{\tau}_j$	Hyperparameter for the Dirichlet distribution
$\boldsymbol{a}_j$	Connections between source region i and target region j

Contents

Part I

Introduction

Chapter 1

Motivation, aim and overview

The brain is an exceptionally complex organ that controls many of the body's functions, processes and interprets information from the outside world, and embodies the essence of the mind and soul. Understanding the brain is therefore of the utmost importance for understanding human behaviour.

The brain is controlled by an enormous network of interconnected neurons, which are able to adapt to new situations, such as ageing [48, 124, 166, 158] and learning [128], or due to a wide variety of disorders, e.g. multiple sclerosis [131], Alzheimer's disease [91, 59] and neuropsychiatric disorders [133, 169]. Studying the healthy brain's structural organization helps us understand the network alterations in the abnormal brain. This in turn can improve the understanding of a wide range of diseases, and elucidate the nature of a disorder, its localization, clinical effects and its prognosis. Moreover, this can help diagnosis and allow better treatment, as well as understanding biological variations [164].

Diffusion magnetic resonance imaging (dMRI) is the only method allowing *in vivo* imaging of white matter tracts and estimation of the brain's structural connectivity. The generated mapping of the complex wiring system of the brain using tractography has been termed the connectome [51, 139]. However, the term *connectome* is now used at various scales ranging from the microscopic scale, mapping individual cells and synapses, to the macroscopic scale, mapping

white matter tracts between gray matter regions [139].

During the last decade there has been an increasing interest in modeling brain connectivity, both structural as well functional [134, 153]. The quantification of differences and similarities in the brain's structural organization between subjects has, however, been a challenge due to the great complexity of the brain's structural organization. The first analyses of structural whole brain connectivity applied graph theoretic measures adapted from network science, such as node degree, clustering coefficient and shortest path [14, 54, 53], concluding that the brain network is small world, though not scale free. The first attempt to classify groups of structural connectivity networks was performed on the global level, meaning that a single summary statistic, such as global efficiency, was extracted for each network. A simple test, such as a t-test was then performed to asses the between-group effects [15]. Though a single summary statistic can be useful to classify groups, it does not provide information about where in the networks the differences are located, and moreover, when aggregating the entire brain, details may be lost.

When describing the brain's organization using a graph, the nodes need to be defined. Depending on the scale, the nodes can represent anything from a single neuron to an entire brain region, such as those defined by a brain atlas [140]. When analysing structural brain connectivity derived from dMRI, the nodes are often defined by a cortical parcellation, but the coarseness of such a parcellation can range from $<$100 regions [57, 47, 58] to thousands of regions [54, 168]. A recent trend is to define the nodes by the voxels or vertices on the WM-GM boundary (Paper B) [10, 113]. Network measures from graph theory have been widely used to analyse brain networks, but unfortunately these measures have been shown to be sensitive to the employed brain parcellation, as well as a wide range of other methodological choices [168, 120]. The way the nodes are defined is therefore of crucial importance. Currently there is no commonly accepted parcellation and the optimal parcellation is likely to be application dependent. Thus, when performing network analyses, validation of the employed parcellation is important, yet it is unclear how to compare the quality of brain parcellations.

Due to the development of enhanced equipment, such as improved MRI scanner hardware, sequences and high performance computing, it is now possible to obtain structural brain connectivity networks in high resolution, i.e. employing a finer cortical parcellation, or using the cortical surface vertices as nodes in the network. A high resolution parcellation results in a huge, noisy and redundant network, which is both very computationally demanding and challenging to interpret [138]. In contrast, by using a too-coarse parcellation, individual differences disappear, complicating the classification and prediction of subjects and diseases [142, 138]. As the resolution of the structural networks increases, the

need arises for prominent statistical modeling tools that can extract the latent structure of the networks. A way to reduce the noise in these huge networks, without eliminating important information by applying a coarse parcellation, is to extract the information about the salient structural organization of the network. This organization can be derived by statistical modeling. Extracting the latent structure from the brain connectivity network in high resolution, i.e. voxel or vertex level, can contribute to the understanding of the underlying connectivity patterns in the brain.

Further complicating the analysis of structural connectivity networks is the fact that the comprehensive data processing pipeline for generating structural connectivity networks from dMRI includes numerous experimenter choices, such as dMRI sequence, correction of acquisition related artifacts, fiber reconstruction and streamline tractography [99, 95, 71, 73, 62, 120]. The fact that all these methodological choices impact the final network emphasizes the importance of validation of the derived network. For this purpose invasive tracers have been shown to be essential [36, 77, 143, 29, 151, 9, 32]. So far validation of tractography and structural connectivity networks have been focused on the validation of fiber model, tractography and their cross-comparison [16, 143, 154], as well as the impact of tractography specific parameters [16, 9, 29]. Although the presence of anatomical information in the images is crucial to extract the "true" structural connectivity network and the scan acquisition parameters have been suggested as being important for the derived network [9, 32], the impact of scan acquisition parameters has not yet been investigated. Indeed, Zhan et al. [170] showed that the final structural connectivity network is affected by the acquired spatial and angular resolutions.

1.1 The aim of this thesis

The aim of this thesis is to use statistical modeling to quantify and validate the brain's structural organization. First, the structural organization of the brain is quantified using stochastic block modeling (Paper A-B). Second, a validation scheme for quantifying a brain parcellations' ability to account for structural connectivity is developed (Paper C). Third, the influence of some of the important methodological choices for constructing structural connectivity networks, particularly the scan acquisition parameters, are quantified (Paper D).

1.2 The structure of this thesis

The first part of this thesis (Chapters 1-5) gives an introduction to the topics necessary to understand the manuscripts included in the second part. Chapter 2 gives an introduction to basic principles of the diffusion process, neuroanatomy, diffusion magnetic resonance imaging and tractography, and an explanation of how to combine these to derive a structural connectivity graph of the brain. Also described are the choices and considerations important for generating structural connectivity graphs, as well as a description of a connectivity graph derived from retrograde invasive tracer injections in monkeys. Chapter 3 describes the statistical models used to derive the salient organization of the structural connectivity graphs, together with link prediction and similarity measures used to evaluate model performances and quality of the derived structural connectivity graphs. Chapter 4 gives a summary of the manuscripts included in the second part of this thesis. Finally, Chapter 5 concludes the thesis with a general discussion and future perspectives.

Chapter 2

Imaging structural brain connectivity

This chapter describes how diffusion weighted magnetic resonance imaging (dMRI) can be used to estimate the structural organization of the brain non-invasively and *in vivo* on the macroscale [139]. To understand what is measured by dMRI and how this can provide insight into the connectivity of the brain, this chapter will go through the basic principles of diffusion, anatomy and how to link these two to obtain an estimate of the brain's structural connectivity.

2.1 Basic principles of diffusion

All particles that are suspended in a fluid are subject to Brownian motion. Brownian motion was first observed by Robert Brown (1773-1858) in 1827, who noticed how pollen grains moved through water, but without being able to determine the mechanism that caused the motion [22]. It was not until later, in 1905, Albert Einstein (1879-1955) described this phenomena theoretically [39].

The diffusion process can quantitatively be described by Fick's first law which describes the net flux (J) of molecules proportional to the negative concentration

gradient (∇C)

$$J = -D\nabla C. \tag{2.1}$$

The proportional constant (D) is the diffusion coefficient which depends on the viscosity and the temperature of the fluid, the size and weight of the molecules and the micro-structural environment[1]. In steady-state there is no net flux, but the molecules are still subject to Brownian motion.

In the case of free diffusion, i.e. diffusion in a homogeneous, barrier-free environment, the diffusion can be described by a Gaussian distribution, where the probability p depends on the diffusion time t_d and the displacement of water molecules r [39].

$$p(r, t_d) = \frac{\exp(-r^2/4Dt_d)}{(4\pi Dt_d)^{3/2}}, \tag{2.2}$$

where $< r^2 >= 2nDt_d$ is the mean-square displacement of water molecules in n-dimensions also known as "Einstein's equation".

2.2 Anatomy of the brain

Brain tissue consists of neurons and glial cells. A neuron consists of a soma (i.e. cell body), dendrites and an axon (i.e. nerve fiber) as illustrated in Figure 2.1. The soma contains the nucleus, which contains the genetic information and controls the cell activity by regulating gene expression and protein synthesis. The communication between cells is facilitated by the dendrites and axons. The dendrites branch out from the soma, like branches on a tree and receive excitatory and inhibitory signals from other neurons through their axons. The intra-cellular space is surrounded by the cell membrane and contains the cytoskeleton, macromolecules, proteins and mitochondria, whereas the extracellular space is the space surrounding the cells, axons and dendrites. The glial cells can be divided into astrocytes, oligodendrocytes and microglia. The oligodendrocytes wrap around axons and form a myelin sheath that increases the conduction speed of the signal propagating along the axons and enables fast signal transmission to other neurons and dendrites [156].

[1]The diffusion coefficient of water at body temperature ($37°C$) is $3 \times 10^{-3} mm^2 s^{-1}$

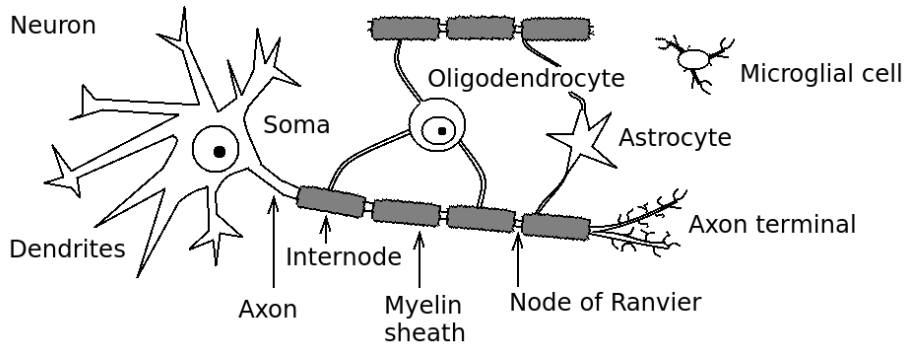

Figure 2.1: An illustration of a neuron, its axon and dendrites. The Oligodendrocyte wraps around the axon, forming segments (i.e. internodes) of insulating myelin. The internodes are separated by small amyelinated regions called nodes of Ranvier. The white matter also contains Astrocytes, that are star-shaped cells maintaining the extracellular ion balance and supporting the blood-brain barrier function, as well as Microglial cells, that are the immune cells of the central nervous system. Inspired by [37].

Brain tissue can be divided into gray matter (GM) and white matter (WM). The GM contains the somas, dendrites and short range intra-cortical axons. The diameter of the dendrites in the GM range from 0.2-3 μm [41]. The GM on the surface of the cerebrum is called the cerebral cortex while collections of neurons within the cerebrum are called subcortical regions. The cerebral cortex is highly folded and these folds are called gyri and the grooves between folds are called sulci. The major cerebral foldings are the same across all subjects, but the details differ from subject to subject. Based on these foldings, the cerebrum can be divided into four lobes: frontal, occipital, temporal and parietal. The WM contains the inter-cortical myelinated axons connecting distal GM regions. Glial cells are found in both GM and WM. The cerebrum comprises approximately a hundred billion neurons connected by several thousand trillion synapses [20, 105]. The WM can be further subdivided into deep WM and superficial WM (WM just beneath the cortical GM). The superficial WM is very dense due to the very high density of short association fibers (u-fibers) [126, 122] connecting adjacent regions of the cortex. U-fibers run along the WM/GM boundary (WGB), and are more tangential to it in sulcal regions than in gyral regions.

A bundle of axons sharing the same major trajectory is called a brain connection (i.e. fiber fascicle). All the brain connections form a brain network and the mapping of these connections has been termed the human connectome [51, 139].

Within a brain fiber fascicle, the axons are mainly running in parallel to one another. This organization facilitates the estimation of brain connections by measuring the anisotropic diffusion of water using dMRI.

2.3 Diffusion weighted magnetic resonance imaging

DMRI utilizes the principle of Brownian motion. In the body water molecules are not subject to free diffusion, but are restricted by cell membranes and hindered by macromolecules and proteins. The diffusion coefficient can be estimated by magnetic resonance imaging (MRI) by applying diffusion sensitive gradients. Due to the hindered and restricted diffusion of water molecules in biological tissue, the estimated diffusion coefficient D depends on the microstructural environment. The estimation of D can be used to infer the properties of biological tissue, such as orientation of fiber bundles and axon diameters [3]. Hence, by measuring the movement of the water molecules in the brain the microstructure of the brain is revealed. DMRI is a key non-invasive method to provide contrast to the micro-structure of the brain. For a general introduction to MRI physics, see e.g. [159].

When acquiring dMRI, D is not measured directly, but is inferred from measurements of the displacement of water molecules over a given time period, the diffusion time, see Equation (2.2). When the water molecules are subject to hindrances, e.g. macromolecules, the average displacement will decrease compared to free diffusion. The estimated value of D will be lower due to the hindrances in the tissue and is therefore called the apparent diffusion coefficient (ADC) [82].

A widely used sequence in dMRI is the Stejskal-Tanner: Pulsed gradient spin-echo (PGSE) [141]. The MRI sequence is outlined in Figure 2.2. When applying a diffusion gradient, the spins of the water molecules are tagged according to their spatial position, by inducing a spatial dependent phase shift along the direction of the gradient, resulting in phase dispersion. After some time, i.e. the diffusion time, a second gradient of the same amplitude and duration, that will rephase the spins, is applied. If the water molecules have not moved, their phase will be fully recovered when applying the second gradient. On the other hand, if the water molecules have moved the phase of the spins will not be fully recovered. The larger the mean displacement of the water molecules between the gradients, the greater the phase dispersion of the spins of the water molecules and hence a greater loss of signal coherence and reduction of signal amplitude. For a given voxel of tissue, the size of the phase dispersion and hence the signal loss, depends on the strength of the gradient $G[mT/m]$, the duration of the

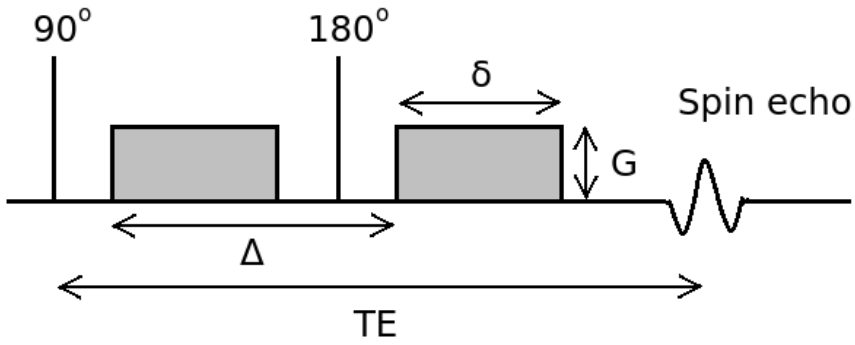

Figure 2.2: The pulsed gradient spin-echo (PGSE) sequence used to measure molecular diffusion. After the 90° RF excitation pulse is applied, the first diffusion encoding gradient with strength G and duration δ is applied. After some time Δ a refocusing pulse inverting the phase shifts is applied and a second diffusion encoding gradient with same strength and duration is applied to rephase the spins. The signal is read out after TE as a spin echo.

gradient $\delta[s]$, and the time interval between applying the gradients $\Delta[s]$. These three factors can be combined into a single parameter describing the degree of diffusion weighting, the so-called b-value [81, 83]. For a PGSE experiment the b-value is given by

$$b = \gamma^2 G^2 \delta^2 \left(\Delta - \frac{\delta}{3} \right), \tag{2.3}$$

where γ is the gyromagnetic ratio. For a PGSE sequence, the b-value can be divided into the q-value $q = \delta\gamma G$ and the diffusion time $t_d = \Delta - \frac{\delta}{3}$. The q-value is also called the wave-vector and it determines the length scale of maximum molecular displacement that can be measured. Increasing the q-value lowers the maximum displacement that we are sensitive to resulting in insensitivity to molecules in large geometries. When applying high q-values, only small geometries contribute to the signal. The diffusion time determines the micro-structural environments being probed and hence is the factor that controls which geometries the sequence is sensitive to. For short diffusion times the sequence will only be sensitive to small micro-structures because only diffusion within small geometries is restricted, but as the diffusion time increases the sequence will be sensitive to larger micro-structures as the water molecules have longer time to

diffuse and hence also get restricted by larger geometries.

The attenuation of the diffusion signal in the case of free diffusion is given by an exponential dependence on the b-value and the diffusion coefficient D

$$S_D = S_0 \exp^{-bD} \Leftrightarrow D = -\frac{\ln \frac{S_D}{S_0}}{b}, \tag{2.4}$$

where S_0 is a reference image obtained without diffusion encoding ($b = 0$). By acquiring such a reference image D can be estimated. This dependence is only true for Gaussian diffusion in the low b-value regime, but is always assumed to apply [70]. When acquiring dMRI the b-value has to be selected by the experimenter.

2.3.1 B-value

As described in the previous section, the b-value is a measure of q^2 and t_d. Measurements with low b-values are dominated by Gaussian diffusion and hence more sensitive to fast diffusion components (extracellular, interaxonal compartments). In contrast, higher b-values reduce the signal from the extracellular space, thus in theory provide higher contrast to fiber configurations. Higher b-values are more sensitive to subtle changes in the underlying fiber orientations and also more sensitive to small diffusion motions around small axons. In general, to be sensitive to slow diffusion and smaller geometries, higher b-values are needed. When acquiring dMRI data post mortem, the applied b-value should be approximately four times larger compared to dMRI data acquired *in vivo* [28]. In Paper D, the effect of different scan acquisition parameters is investigated, including the effect of varying b-values. Figure 2.3 shows three diffusion weighted images acquired from the same monkey brain (data used in Paper D) with three different b-values. Note how the SNR decreases when increasing the b-value, but at the same time the sensitivity to intracellular diffusion increases, seen by bright WM structures such as the corpus callosum.

2.3.2 Artifacts

When acquiring dMRI data, motion artifacts (e.g. head motion) are unavoidable introduced when scanning subjects *in vivo*. Movement artifacts, such as subject motion and pulsation artifacts can introduce ghosting along the phase-encoding direction or result in severe signal drop-out if the movement appears in the

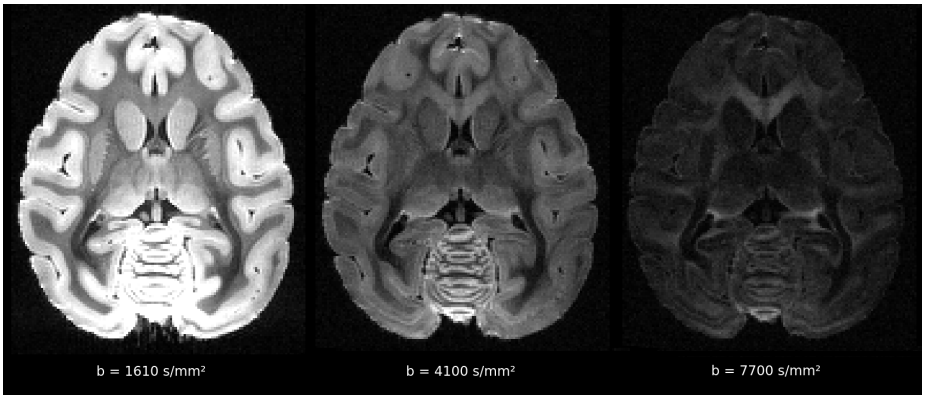

Figure 2.3: Diffusion weighted images acquired from the same monkey brain, using a b-value of 1610 s/mm^2 (left), 4100 s/mm^2 (middle) and 7700 s/mm^2 (right). The image for each b-value correspond to a single gradient direction and is averaged across three signal repetitions. Spatial resolution is 0.5 mm^3.

diffusion encoding time period. A way to minimize, yet not eliminate, the effect of movement artifacts is to apply a MRI sequence less prone to motion, such as echo-planer imaging (EPI), which is the standard for clinical dMRI. EPI is a fast imaging technique, where an image typically is acquired in the time frame around 100 ms, hence making motion within a volume negligible [84]. The motion between acquired volumes can be mollified by co-registering the images in the post-processing step. Unfortunately, EPI also have some drawbacks, for instance it is prone to eddy currents and susceptibility artifacts. Eddy currents are electrical currents that are induced by a changing magnetic field and arise when strong gradient pulses are switched rapidly. In general dMRI is especially affected by eddy currents during the diffusion encoding gradient duration δ. A way to minimize this effect previously was to use the twice-refocused spin echo sequence by Reese et al. [121], but due to improvement in scanner hardware, the effect of eddy currents is reduced. However, eddy currents still introduce linear transformations like shear, but these can be corrected in the post-processing step. Susceptibility artifacts are related to the differing magnetic properties of the imaged tissue which introduce local inhomogeneity in the static magnetic field at the borders between tissue types. By acquiring images with reversed phase-encoding, susceptibility artifacts can be reduced in the post-processing step by maximizing the similarity of the two images with opposite phase-encoding. After correcting for artifacts in the post-processing of the data, the diffusion encoding directions have to be updated accordingly [85, 4].

In paper B, the in house (DRCMR) diffusion processing pipeline was used to minimize motion artifacts, eddy current effects and susceptibility artifacts. The pipeline is implemented in SPM v. 8.429 (http://www.fil.ion.ucl.ac.uk/spm/) with Matlab 7.12 (The mathWorks, Inc., Natick, Massachusetts, USA), using plug-ins from FSL v. 5.0 (http://fsl.fmrib.ox.ac.uk/fsl/fslwiki/) [63, 161, 135] and Camino (http://camino.cs.ucl.ac.uk/) [26]. To minimize susceptibility artifacts, we applied a voxel displacement map (VDM) based on the acquired field map using the field map toolbox of SPM8 [66]. The voxel shifts for the VDM were estimated using the two reversed phase-encoding images, as implemented in FSL's topup tool [6, 135]. Motion artifacts (translation and rotation) were estimated using a rigid-body transformation. The transformation was expanded to a full affine transformation by including the six parameters from shear and zoom to minimize the eddy current effects. The images were aligned and resliced by applying this transformation, using normalised mutual information as cost function and 7th order B-spline interpolation [35]. To compensate for the applied transformation, the 61 non-collinear diffusion encoding gradient directions were updated accordingly using the same rotations and transformations, as suggested in [85, 4].

In Paper C, data provided by the Human Connectome Project (HCP) [153] was analyzed, thus the "minimal preprocessing pipeline" provided by the HCP [46] was used to minimize artifacts. First, the average b0 image was intensity normalized and EPI distortion correction was done using FSL's topup tool [135, 6]. Second, the eddy current distortions and movement artifacts were minimized using FSL's eddy tool [7], the images were corrected for gradient-nonlinearities [74] and an estimation of the effects of gradient-nonlinearities on the diffusion weighting and direction in each voxel were calculated [11, 137]. Third, the average b0 image was registered to the native structural T1w image with FSL's FLIRT BBR cost function and FreeSurfer's bbregister [50] and transformed to 1.25 mm structural space. Finally, the diffusion encoding directions and the gradient field tensor were updated using the b0 to T1w transformation [4].

In paper D the data was acquired from a post mortem monkey brain using the setup described in [34]. The setup uses a spin echo sequence that introduces minimal geometrical distortions. The dataset was visual inspected and revealed no need for any post processing.

2.4 Estimation of the fiber orientations

The water molecules in the brain are subject to hindered (extracellular space) and restricted diffusion (intracellular space). In the intracellular space the diffu-

sion is restricted by the cell membranes, macromolecules and the myelin sheaths surrounding the axons in the white matter. The molecules are restricted perpendicular to the axons, but to a much less extent along the axons. As the water molecules diffuse further along the axons than across axons, the movement of the water molecules can be used to describe the architecture of the brain. When measuring diffusion in regions with ordered tissue, i.e. anisotropic diffusion, the signal attenuation and hence the ADC is dependent on the direction of the applied gradients and can no longer be described by a single diffusion coefficient. To extend the description of anisotropic diffusion to 3D, the diffusion tensor DT can be used. When the diffusion of water molecules is restricted, the resulting signal is high, whereas the signal attenuates when the water molecules can move a longer distance, i.e. the amount of signal loss depends on the diffusion coefficient (D). To be able to estimate the connectivity of the brain the diffusion is measured along multiple non-collinear gradient directions.

2.4.1 The diffusion tensor model

The DT was originally proposed for use in MRI by Basser et al. [12, 13]. The DT is a 3×3 matrix as given by Equation 2.5, where the diagonal elements describe the diffusion along the main directions (orthogonal axes) and the off-diagonal elements describe the correlation between the mean displacements along the orthogonal axes. Thus, the DT can be viewed as a covariance matrix

$$DT = \begin{bmatrix} D_{xx} & D_{xy} & D_{xz} \\ D_{yx} & D_{yy} & D_{yz} \\ D_{zx} & D_{zy} & D_{zz} \end{bmatrix}. \tag{2.5}$$

As diffusion is non-directional, the DT is symmetric and hence has six unknown elements. To estimate the anisotropic diffusion in 3D at least six non-collinear and non-coplanar directions (plus one non-diffusion-weighted image) are required to calculate the DT. In diffusion tensor imaging (DTI) [13, 118], the diffusion signal in every voxel is estimated by a tensor. The most common measures computed from the estimated tensor are mean diffusivity (MD) and fractional anisotropy (FA) [117] given by

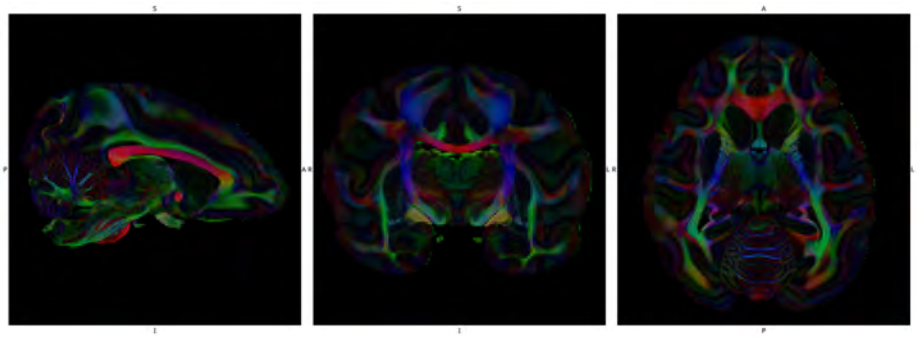

Figure 2.4: Color-coded FA map. The data is an average of three repetitions acquired using a b-value of 7700 s/mm^2, 180 directions and a spatial resolution of 0.5 mm^2. The colors indicate the orientation of the fiber bundles; red is left-right, green is anterior-posterior and blue is superior-inferior.

$$MD = \hat{\lambda} = \frac{\lambda_1 + \lambda_2 + \lambda_3}{3} \tag{2.6}$$

$$FA = \sqrt{\frac{3}{2}} \frac{\sqrt{(\lambda_1 - \hat{\lambda})^2 + (\lambda_2 - \hat{\lambda})^2 + (\lambda_3 - \hat{\lambda})^2}}{\sqrt{\lambda_1^2 + \lambda_2^2 + \lambda_3^2}}, \tag{2.7}$$

where $(\lambda_1, \lambda_2, \lambda_3)$ are the eigenvalues of the DT. MD is a measure of how unhindered the diffusion is with a MD of zero meaning no diffusion is present (static water molecules). MD is fairly uniform throughout parenchyma in the range of b-values typically applied in clinically studies ($b \leq 1500$ s/mm^2) [119]. For increasing b-values, WM has a lower MD compared to GM [165]. FA is normalized to take values from zero (isotropic diffusion) to one (diffusion restricted to be only along one axis). One major limitation of DTI is that it can only recover a single fiber orientation in each voxel and fail to estimate crossing fibers and is therefore not ideal to estimate the fiber orientations when performing tractography and connectivity mapping, because most voxels contain more than one fiber population [65]. The work presented herein uses tractography to estimate the structural brain connectivity and hence, DTI is only used to assess to quality of the data, such as checking the orientation of the major fiber bundles. Figure 2.4 shows a color-coded FA map of the dataset used in Paper D, acquired using a b-value of 7700 s/mm^2, 180 non-collinear uniformly distributed directions, and a spatial resolution of 0.5 mm^2. The dataset is an average of three signal repetitions.

2.4.2 Multi-fiber models

To be able to model multiple fibers in each voxel, multiple models that are capable of estimating more complex fiber configurations have been developed. These models include the multi-tensor model [148], that uses a mixture of Gaussian densities to model multiple fibers instead of a single Gaussian as in DTI. Another example of a model capable of modeling multiple fibers within a voxel is the ball and sticks (B&S) model by Behrens et al. [18, 17]. Because the choice of diffusion model has not been the primary focus in this study and in interest of time, only a single model of the diffusion data is employed in the work presented herein, namely the B&S model as implemented in FSL's BedpostX[2]. The B&S model has been shown to solve the problem of crossing fibers well [17], is widely used and is implemented in the open source FMRIB Software Library (FSL) [161, 135, 64]. But in fact multiple other models could have been applied to estimate the diffusion orientations, including persistent angular structure MRI [2], spherical deconvolution (SD) [146, 144], q-space imaging or diffusion spectrum imaging (DSI) [157], and Q-ball imaging [147]. An overview of these methods can be found in the book by Johansen-Berg et al. [67].

2.4.3 The ball and stick model

The B&S model [18] models the underlying fiber structure in each voxel as a two-compartment model, where the first compartment models the isotropic diffusion of free water (the ball) and the second compartment models the anisotropic diffusion within and around the axons along a single dominant direction (the stick). An extension of this model [17] models more complex fiber configurations by including multiple anisotropic compartments (multiple sticks). The parameters of the model are fitted using Bayesian estimation. To prevent the model from overfitting the data, i.e. allow multiple fibers in voxels that do not support multiple fibers, automatic relevance determination (ARD) [94] is applied. As opposed to other model selction techniques, such as cross-validation, ARD fits the most complex model, but ensures that only parameters supported by the data contribute to the likelihood. The marginal posterior distribution of the parameters given the model and the dMRI data is sampled using Metropolis Hastings Markov Chain Monte Carlo sampling as described in section 3.5.1. The posterior probabilities on the parameter estimates characterize the uncertainty in the parameters.

[2]BedpostX stands for: Bayesian Estimation of Diffusion Parameters Obtained using Sampling Techniques. The X stands for modelling crossing fibers.

2.4.4 Number of gradient directions

Theoretically, to be able to estimate the simple DT, six unique gradient directions and a non-diffusion weighted reference image are enough. However, to obtain a rotational invariant estimate of the tensor in the presence of noise more directions are required. Studies have shown that both 24 [112] and 30 [132] unique sampling directions outperform a scheme with only six directions. Furthermore, it has been shown that at least 30 unique evenly distributed gradient directions are needed to robustly determine mean diffusivity, fractional anisotropy and tensor orientation [68]. Even though 30 directions are sufficient in DTI it is recommended to use as many directions as time allows, especially for tractography applications [68]. The more complex the organization is, the more directions are needed to estimate the true underlying structure.

In Paper D three different gradient schemes are compared. The gradient schemes contain 20, 60 and 180 uniformly distributed directions, respectively. The gradient schemes were made specific for this study. To optimize the acquisition, the 20 directions is a subset of the 60 directions which in turn is a subset of the 180 directions. The directions were uniformly distributed on a unit sphere using the electrostatic repulsion algorithm as proposed in [72]. For the first gradient scheme, 20 uniformly directions are estimated. For the second gradient scheme, these 20 directions are kept fixed and 40 additional direction are estimated, such that all the 60 directions are as uniformly distributed as possible. For the third gradient scheme the same procedure is repeated: the initial 60 directions kept fixed and 120 additional directions are estimated to obtain a gradient scheme with 180 directions. Figure 2.5 shows the estimated points on a unit sphere for the three different gradient schemes.

2.4.5 Fiber configurations

When measuring the diffusion of water using dMRI, it is the average displacement of water molecules across a voxel that is measured. Usually dMRI is measured in a resolution in the order of cubic millimeters and state-of-the-art human dMRI data acquired by the HCP [153] has a resolution of 1.25 mm^3, whereas the diameter of human myelinated axons is in the range $0.3 - 10\mu m$ [49]. This means that a single voxel contains thousands of axons [152], which can have different trivial or non-trivial configurations, such as parallel, fanning, bending and crossing as shown in Figure 2.6 [86, 93, 109]. In such complex areas, it is difficult to estimate the true connections and furthermore, dMRI is not able to distinguish the anatomical polarity of the WM tracts. Models used to estimate the voxel-wise diffusion must be able to disentangle these configurations to obtain

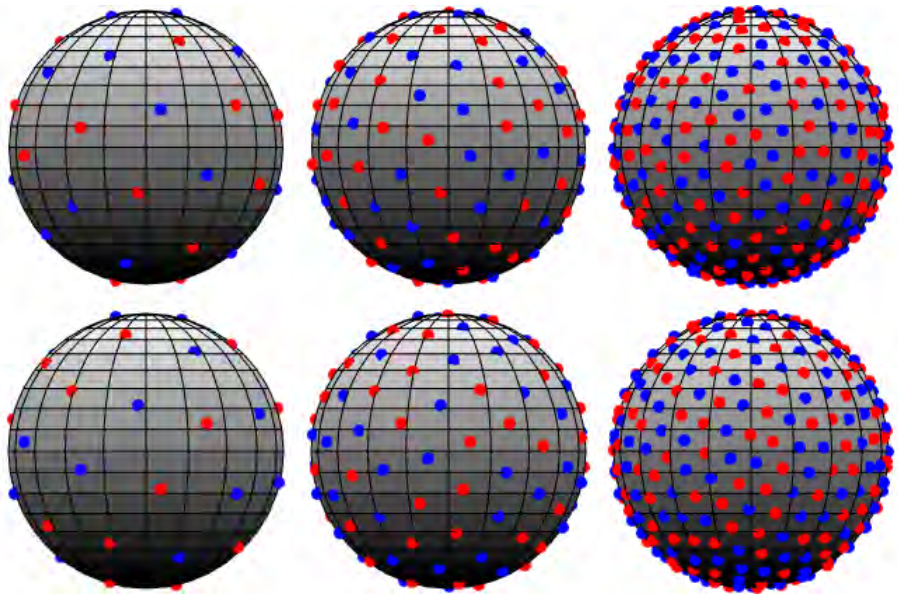

a **b** **c**

Figure 2.5: Three different gradient schemes with (a) 20, (b) 60, and (c) 180 uniformly distributed directions. The two rows show opposite views of the sphere. The red points are the actual directions measured, while the blue dots are the mirror images of the red dots.

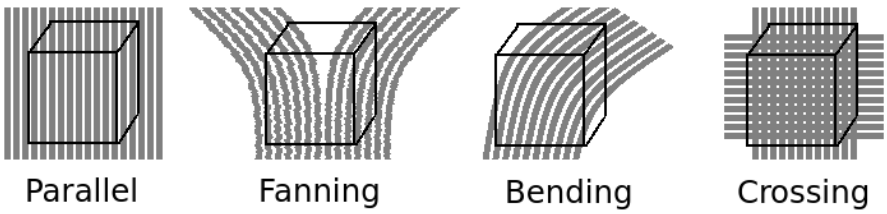

Figure 2.6: Illustation of different fiber configurations that can be present within a voxel. Inspired by [129].

the true information about the underlying microstructure. This limitation may be improved by higher spatial resolution, as investigated in Paper D, together with local multi-voxel spatial models as proposed by Savadjiev et al. [125, 152], but a dMRI resolution close to that of the axon diameters is unlikely to be attainable in the near future, if ever. The only way to infer connections between dMRI voxels is therefore to impose a model of local connections, as described in the following section.

2.5 Tractography

Tractography is a non-invasive technique to estimate and visually represent fiber tracts using dMRI. Tractography can be used to map brain connections, but it is important to keep in mind that it does not provide physiological information about the connections, such as conduction velocity and delays. The ability of tractography to estimate brain connections has been confirmed by tracer studies in post mortem minipigs [36], mice [162] and macaques [116]. Tractography algorithms are commonly divided into two types; deterministic [100, 149] and probabilistic [114, 115, 17] approaches, both generating continuous curves (i.e. streamlines) in space.

Deterministic tractography algorithms [25, 100, 102] generate a streamline by following the main direction in each voxel, without allowing for possible uncertainties in the fiber orientation. Hence, deterministic tractography always result in the same result, meaning that in regions with large uncertainties (e.g. crossing fibers), the most probable direction will always be selected.

Probabilistic tractography was developed to enable quantification of the uncertainty within a voxel related with estimation of brain connections. To quantify the uncertainty of a brain connection, a probabilistic tractography algorithm

generates streamlines by sampling the direction from the probability density function (pdf) of the estimated diffusion orientations, that models the uncertainty in a voxel. To obtain a distribution of fibers, every streamline is repeated a large number of times. When all streamlines have been estimated, a streamline count map is generated by counting the number of streamlines entering each voxel, together with a connectivity matrix providing information about how many streamlines connecting two regions of interest. Streamline counts obtained with tractography are not a quantitative measure of the strength of the estimated connections, nor a measure of the number of axons. The streamline counts depend on multiple factors, such as the amount of fibers aligned in a given orientation, local heterogeneity in fiber orientation, fiber diameters, length of the pathway (distance between regions), and uncertainties in each voxel. If one voxel along the trajectory is noisy this can reduce the number of streamlines between two regions significantly [73].

Probabilistic tractography has been shown to produce more false positives, but also more true positives than deterministic tractography [143]. The false positives produced by tractography can be mollified by applying a threshold, but unfortunately the choice of threshold is not a trivial task [61]. However, in paper C and D, the choice of threshold is investigated. Based on previous studies [16, 120], the tractography approach applied in the work herein is probabilistic tractography, explicitly FSL's probtrackX2 [18, 17].

2.5.1 Seeding strategy

To be able to construct a whole-brain connectivity map, seed and target masks, as well as termination and exclusion masks have to be defined in the tractography. In general consensus, the target mask is defined by the WM-GM boundary, either as voxels on the boundary or as vertices in the WM surface. The termination mask is defined by the boundary between GM and the cerebrospinal fluid (CSF) and exclusion masks often includes masks of the subcortical structures and ventricles. However, the definition of the seed mask is more questionable.

The seed mask defines where the streamlines are initiated and commonly two different strategies are applied. Either are streamlines initiated in all WM voxels (WM seeding) or at the WM-GM boundary (GM seeding). When performing WM seeding, any given tract is comprised of streamlines seeded from points along its entire length, which increases the chances of detecting long range connections. In WM seeding longer tracts will obtain higher streamline counts than short tracts as more streamlines are initialized within the course of the tract. In contrast, longer paths are more difficult to estimate when performing GM seeding as many steps are needed to go from region A to region B and hence

the possibility to end up in region B every time is smaller implying that longer tracts get lower streamline counts [88]. Thus, GM seeding is more susceptible to path length dependencies [90]. When thresholding the structural connectivity graphs based on the streamline counts, in order to remove false positives, more long tracts will be removed if GM seeding is performed.

In paper A, B and C, we used WM seeding, whereas in Paper D the effect of seeding strategy was investigated.

2.5.2 Number of streamlines

The number of streamlines initialized in each seed region needs to be high enough to fully sample the probability density function (pdf) of possible directions in each voxel. When the pdfs are fully sampled the streamline counts will increase, but the contrast in the probability map will be constant. However, when increasing the number of streamlines the generated connectivity matrix becomes more dense and a higher threshold is needed to attain the optimal trade-off between sensitivity and specificity. In general fewer streamlines are needed when performing WM seeding compared to GM seeding, because tracts are sampled along their entire length.

In Paper B, C and D, we showed that relatively few streamlines are needed when performing WM seeding and Donahue et al. [32] initializes as few as 100 streamlines/voxel.

2.6 Tract Tracing

During the late 1960s and early 1970s the use of naturally occuring cellular transport for fiber tracing gave rise to multiple tract tracing studies. These studies have contributed tremendously to the understanding of the anatomy of the brain [80].

Several tract tracing techniques exist, but most of them are based on active transport mechanisms in the living cell, making them unsuitable for studying the human brain [8]. However, some lipophilic substances such as carbocyanine derivates, that are transported passively by diffusion, can be applied to formalin-fixed tissue. However, as the diffusion in cold tissue is much slower than in fresh postmortem (not formalin-fixed tissue), only small fibers in the adult human brain have been studied using this technique [43].

Tract tracing can be divided into anterograde transport, directed from the cell body to the synapse, and retrograde transport, directed from the synapse back to the cell body. In contrast to tractography, tract tracing substances are transported within axons on the microtubules and are therefore not affected by sharp turning fibers, kissing and crossing fibers and other complex fiber configurations. Injections of tract tracing substances provide high resolution visualisation of the intracellular space only, whereas dMRI images both the intra- and the extracellular space. Tracer injections are therefore an important tool for validating tractography and often used as a gold standard. For ethical reasons it is not allowed to inject tract tracing substances into the living human brain, and hence studies comparing tract tracing and tractography are done in mice [23], minipigs [36] or monkeys [29, 97, 96, 143, 77, 151, 32, 9].

A state-of-the-art retrograde tracer study in monkeys was performed by Markov et al. [97, 96]. In this study 28 monkeys were employed. Single injections of fluorescent retrograde tracers, fast blue (FsB) and diamidino yellow (DY) were injected into 29 cortical regions and the labeled neurons in 91 cortical regions, covering the whole cortical surface, were counted. Thus, resulted in a 91×29 tracer connectivity graph. Two different tracers were injected to allow two injections in each brain without mixing up their projections. In Paper D, we acquired a high resolution dMRI dataset with multiple angular resolutions and multiple b-values using the ex vivo imaging pipeline proposed in [34]. By using the tracer connectivity graph by Markov et al. [97, 96] as a gold standard, the influence of different scan acquisition parameters on the structural connectivity graph generated using tractography was investigated.

2.7 Brain parcellations

For centuries people have tried to understand the brain. Maps are created of both white matter tracts [101, 111, 126] and cortical regions [21] to get a deeper insight into the brain; its function and organization. Parcellation of the brain has been based on a wide range of features, from gross anatomical landmarks, surface morphology [30, 42], structural connectivity (Paper B) [113, 10], functional activation [150, 47] to cyto- and myeloarchitecure [21] and combinations thereof [45, 40].

When analyzing whole-brain structural connectivity a cortical parcellation is often employed to define the nodes in the network, thus the resolution of the network depends on the employed parcellation. When analyzing structural brain connectivity using graph theoretic measures, the choice of parcellation has been shown to influence the results [168] and the optimal parcellation is likely to

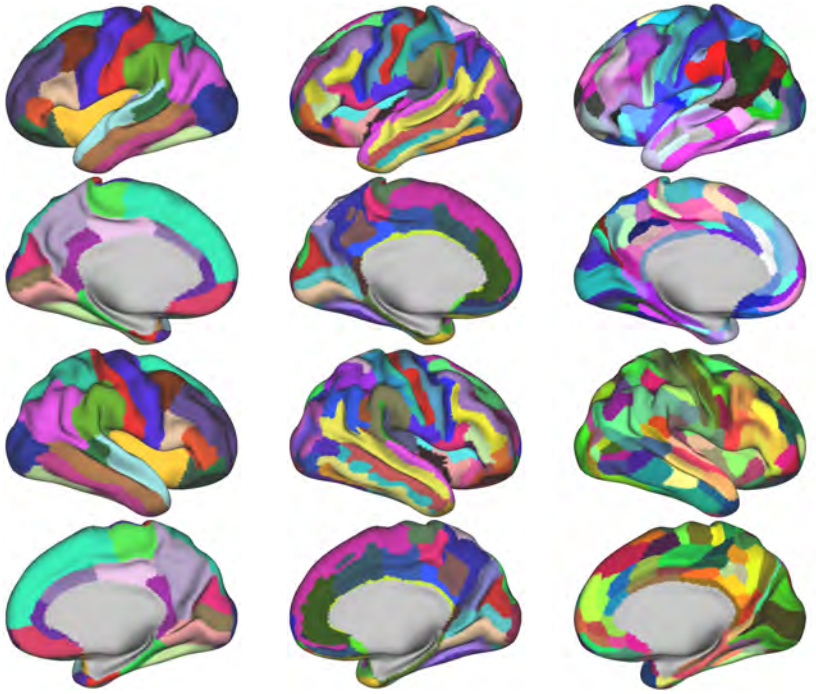

(a) (b) (c)

Figure 2.7: Cortical parcellations visualized on a inflated WM surface. (a) The Desikan-Killiany atlas with 68 regions [30]. (b) The Destrieux atlas with 148 regions [31]. (c) The Human Connectome Multi-Modal Parcellation with 360 regions [45].

be application specific. In paper C, we quantify two parcellations based on surface morphology and a multi-model parcellation based on task and resting-state functional MRI, myelin and cortical thickness by their ability to predict structural connectivity based on tractography. The three employed atlases are visualized in Figure 2.7.

Chapter 3

Statistical modeling of structural brain connectivity

This chapter defines a brain network (section 3.1) and describes the statistical models used for clustering brain networks to extract the latent information (section 3.2), including ward clustering (section 3.3), the stochastic block model and a non-parametric extension forming the infinite relational model (section 3.4). In addition, methods to evaluate model performances are described, including the area under the curve (AUC) of the receiver operator characteristics (section 3.6.2), predictive log-likelihood (section 3.6.1) and normalised mutual information (section 3.6.4). Finally, cross-entropy is presented as a similarity measure between the connectivity profiles of two brain networks (section 3.7).

3.1 Brain networks

The complex organization of the brain can be described using graph theory applicable to a broad range of applications from social science to neurobiology (adopted from network science). A graph consists of nodes connected by links and can be described by an adjacency matrix $\mathbf{A}$. If a link exists between node i and node j the adjacency matrix element A_{ij} takes on a value different from zero. If no links exist $A_{ij} = 0$. A graph can either be directed or undirected and

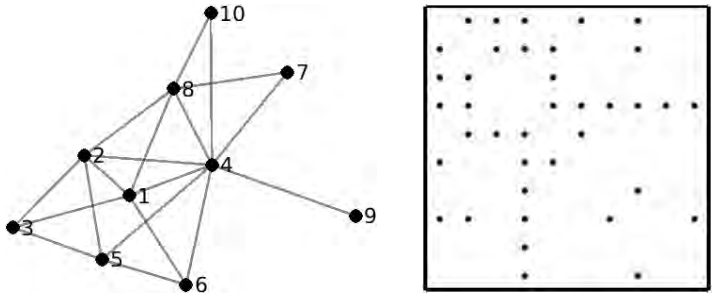

(a) (b)

Figure 3.1: A binary and undirected network (a) and its adjacency matrix $\boldsymbol{A}$ (b). Black dots in the adjacency matrix represent links.

either binary or weighted. A binary graph only contains zeros and ones, whereas the links in a weighted graph are given different weights. An undirected graph is symmetric ($A_{ij} = A_{ji}$), while a directed graph is asymmetric ($A_{ij} \neq A_{ji}$). Figure 3.1 shows an example of a binary undirected graph.

3.2 Clustering

Networks can be represented in a compressed form by clustering nodes according to their connectivity to the rest of the network. This compressed representation of the network reduces noise and the network gets more interpretable. A way to perform this is by clustering nodes, such that nodes are densely connected with the other nodes in the same cluster and only sparsely connected with nodes outside the cluster. Such dense connected clusters are known as communities. The degree of community structure exhibited by a given clustering can be measured using the modularity index [107]. Modularity measures the fraction of within-cluster links minus the expected fraction of within-cluster links in a random network with the same node degree. Hence, one way to cluster a network is by finding the partition with highest modularity [108, 87]. However, modularity is optimized by taking into account only the within cluster link density, regardless of the between cluster link-densities. Models accounting for both within cluster link-densities and between link-densities include Ward clustering (Paper C) [155, 10, 38, 142] and stochastic block models (Paper A, B and C) [160, 56, 110, 127, 5, 10]. These models are described in the following sections.

3.3 Ward clustering

Ward clustering was introduced in 1963 by Ward [155] and has previously been proposed for clustering neuroimaging data in [10, 38, 142]. Ward clustering is a hierarchical agglomerative approach, initiated by assigning all nodes to their own cluster. In every step the two clusters that minimizes the change in the value of the proximity measure are merged until all clusters have merged into a single cluster. To find the two clusters to be merged, the proximity measure must be evaluated for every possible combination of clusters. Different proximity measures can be employed, but in Paper C we used W_{ij}^2 as suggested in [10]

$$W_{ij} = \sqrt{\sum_{a \neq ij} (A_{ia} - A_{ja})^2 + \sum_{a \neq ij} (A_{ai} - A_{aj})^2}. \tag{3.1}$$

This proximity measure uses the dissimilarity between the connectivity patterns of any two elements of the connectivity matrix $\boldsymbol{A}$. In each step of the algorithm, the optimal pair of clusters to merge was found using the Lance-Williams dissimilarity update formula [79, 106]. How the clusters are merged can have different constraints, e.g. a constraint that only allows merging of adjacent clusters, as used in Paper C, to ensure that only neighbouring vertices in the WM surface are clustered together, as proposed in [10].

The result of a hierarchical clustering algorithm is often presented as a dendrogram. Figure 3.2 shows a binary undirected graph comprising 500 nodes, the resulting dendrogram when using the proximity measure given in Equation (3.1) and three sorted graphs obtained using different cut-off levels of the dendrogram.

3.4 Stochastic block-modeling

The general idea of block-modeling is to decompose a network into groups of nodes with similar properties, such as similar connectivity pattern to the rest of the network. In the following, two stochastic block models are described. The stochastic block model (SBM) (section 3.4.1) and the non-parametric extension of the SBM, the infinite relational model (IRM) (section 3.4.2). The models are here specified for undirected networks, as diffusion is non-directional and hence does not provide information about the direction of the connections.

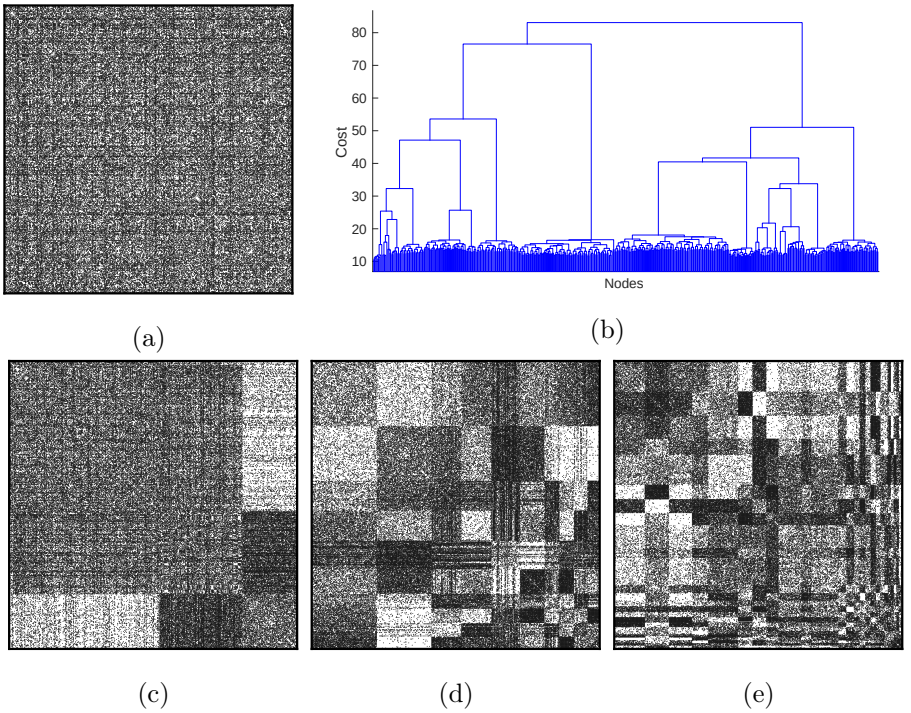

Figure 3.2: Ward clustering. (a) An unsorted binary undirected graph with 500 nodes. (b) The dendrogram showing the hierarchical tree. (c-e) Graphs sorted according to the ward clustering at three different cut-off levels, 3, 10 and 30 clusters, respectively.

3.4.1 The stochastic block model

The stochastic block model (SBM) (Paper C) [5, 110, 160, 56, 127] is a network model that can be used to cluster nodes into homogeneous cluster according to their connectivity to the rest of the network. The SBM models the existence of a link between two nodes dependent on the link density between the two clusters the nodes belong to. Let K be the number of clusters and $\mathbf{z}$ the clustering assignment vector for all nodes. Let z_j be the j-th element of $\mathbf{z}$, such that $z_j = l$ if the j-th node belongs to cluster l. The probability of a link between cluster l and m, η_{lm} is drawn from the beta distribution and the existence of a link between two nodes A_{ij} is drawn from the Bernoulli distribution with probability $\eta_{z_i z_j}$. This corresponds to tossing a coin given the link density between cluster l and m. To allow flexible cluster sizes the prior on the assignment matrix $\mathbf{z}$ is distributed according to the Dirichlet distribution. The generative model is

given by

$$\begin{aligned}
\text{Links between nodes} \quad & A_{ij} \sim Bernoulli(\eta_{z_i z_j}) && (3.2)\\
\text{Link densities between clusters} \quad & \eta_{lm} \sim Beta(\beta^+, \beta^-) && (3.3)\\
\text{Clustering} \quad & \mathbf{z} \sim Categorical(\boldsymbol{\pi}) && (3.4)\\
& \boldsymbol{\pi} \sim Dirichlet(\tilde{\boldsymbol{\alpha}}). && (3.5)
\end{aligned}$$

Let m_k be the number of nodes in cluster k, such that $\sum_{k=1}^{K} m_k = J$, then the joint prior is given by

$$\begin{aligned}
p(\mathbf{z}, \boldsymbol{\pi} \mid \tilde{\boldsymbol{\alpha}}) &= \left[\prod_{i=1}^{J} p(z_i \mid \boldsymbol{\pi})\right] p(\boldsymbol{\pi} \mid \tilde{\boldsymbol{\alpha}}) && (3.6)\\
&= \frac{1}{\mathcal{B}(\tilde{\boldsymbol{\alpha}})} \prod_{k=1}^{K} \pi_k^{m_k + \tilde{\alpha}_k - 1}, && (3.7)
\end{aligned}$$

where the normalizing constant $\mathcal{B}$ is the multivariate beta function

$$\mathcal{B}(\tilde{\boldsymbol{\alpha}}) = \frac{\prod_{k=1}^{K} \Gamma(\tilde{\alpha}_k)}{\Gamma(\sum_{k=1}^{K} \tilde{\alpha}_k)}, \quad \tilde{\boldsymbol{\alpha}} = (\tilde{\alpha}_1, ..., \tilde{\alpha}_K). \tag{3.8}$$

By imposing an equal concentration parameter on all clusters $\tilde{\alpha}_1 = ... = \tilde{\alpha}_k = \alpha/K$, such that $\sum_{k=1}^{K} \tilde{\alpha}_k = \alpha$, the marginalized joint prior is given by the so-called Pólya distribution

$$p(\mathbf{z} \mid \alpha) = \int p(\mathbf{z}, \boldsymbol{\pi} \mid \alpha) d\boldsymbol{\pi} = \frac{\Gamma(\alpha)}{\Gamma(\alpha + J)} \prod_{k=1}^{K} \frac{\Gamma\left(\frac{\alpha}{K} + m_k\right)}{\Gamma\left(\frac{\alpha}{K}\right)}. \tag{3.9}$$

The probability of a link between cluster l and m is drawn from the beta distribution with the hyperparameters β^+ and β^-

$$p(\boldsymbol{\eta} \mid \beta^+, \beta^-) = \prod_{l \geq m} \frac{1}{B(\beta^+, \beta^-)} \eta_{lm}^{\beta^+ - 1} (1 - \eta_{lm})^{\beta^- - 1}. \tag{3.10}$$

The probability of observing a link between node i and j follows the Bernoulli distribution resulting in the likelihood

$$p(\mathbf{A} \mid \boldsymbol{\eta}, \mathbf{z}) = \prod_{i>j} \eta_{z_i z_j}^{A_{ij}} (1 - \eta_{z_i z_j})^{1 - A_{ij}} = \prod_{l \geq m} \eta_{lm}^{N_{lm}^+} (1 - \eta_{lm})^{N_{lm}^-}, \tag{3.11}$$

where N_{lm}^+ and N_{lm}^- respectively denotes the total number of links and non-links between cluster l and m. When using the model on S subjects (Paper C), the probability of observing a link is given by the product over subjects [5], resulting in

$$p(\mathbf{A}^{(1)}, ..., \mathbf{A}^{(S)} \mid \boldsymbol{\eta}, \mathbf{z}) = \prod_{s=1}^{S} \prod_{i>j} \eta_{z_i z_j}^{A_{ij}^{(s)}} (1 - \eta_{z_i z_j})^{1 - A_{ij}^{(s)}} = \prod_{l \geq m} \eta_{lm}^{N_{lm}^+} (1 - \eta_{lm})^{N_{lm}^-}, \tag{3.12}$$

where N_{lm}^+ and N_{lm}^- now respectively denotes the total number of links and non-links between cluster l and m for all subjects. The joint likelihood is obtained by combining Equation 3.9- 3.11

$$\begin{aligned}
p(\mathbf{A}, \mathbf{z}, \boldsymbol{\eta} \mid \alpha, \beta^+, \beta^-) &= p(\mathbf{A} \mid \boldsymbol{\eta}, \mathbf{z}) p(\boldsymbol{\eta} \mid \beta^+, \beta^-) p(\mathbf{z} \mid \alpha) && (3.13) \\
&= \left[\prod_{l \geq m} \eta_{lm}^{N_{lm}^+} (1 - \eta_{lm})^{N_{lm}^-} \right] && (3.14) \\
&\times \left[\prod_{l \geq m} \frac{1}{B(\beta^+, \beta^-)} \eta_{lm}^{\beta^+ - 1} (1 - \eta_{lm})^{\beta^- - 1} \right] && (3.15) \\
&\times \left[\frac{\Gamma(\alpha)}{\Gamma(\alpha + J)} \prod_{k=1}^{K} \frac{\Gamma\left(\frac{\alpha}{K} + m_k\right)}{\Gamma\left(\frac{\alpha}{K}\right)} \right]. && (3.16)
\end{aligned}$$

Because the beta distribution is the conjugate prior to the Bernoulli distribution, the likelihood can be marginalized by integrating out $\boldsymbol{\eta}$

$$p(\mathbf{A}, \mathbf{z} \mid \alpha, \beta^+, \beta^-) = \int p(\mathbf{A}, \mathbf{z}, \boldsymbol{\eta} \mid \alpha, \beta^+, \beta^-) d\boldsymbol{\eta} \tag{3.17}$$

$$= p(\mathbf{z} \mid \alpha) \prod_{l \geq m} \frac{B(N_{lm}^+ + \beta^+, N_{lm}^- + \beta^-)}{B(\beta^+, \beta^-)}, \tag{3.18}$$

where $B(a, b) = \frac{\Gamma(a)\Gamma(b)}{\Gamma(a+b)}$ is the beta function.

By applying Bayes' theorem the conditional posterior distribution of the assignment of a single node z_i can be found as

$$p(z_i = l \mid \mathbf{A}, \mathbf{z}_{\setminus i}, \alpha, \beta^+, \beta^-) = \frac{p(\mathbf{A}, \mathbf{z}_{\setminus i}, z_i = l \mid \alpha, \beta^+, \beta^-)}{\sum_m^K P(\mathbf{A}, \mathbf{z}_{\setminus i}, z_i = m | \alpha, \beta^+, \beta^-)}, \tag{3.19}$$

where $\mathbf{z}_{\setminus i}$ is the assignment of all nodes except node i. In the inference $\mathbf{z}$ is sampled from the conditional posterior distribution using Markov Chain Monte Carlo (MCMC) sampling as described in section 3.5.1.

3.4.2 The infinite relational model

A limitation of the SBM is that it has a fixed finite number of clusters that has to be defined *a priori* by the experimenter or learned by model selection. By considering partitions rather than labels and taking the limit $K \to \infty$ of Equation (3.9), thus allowing an infinite number of clusters, we get [127]

$$\lim_{K \to \infty} p(\mathbf{z} \mid \alpha) = \frac{\alpha^K \Gamma(\alpha) \prod_k \Gamma(m_k)}{\Gamma(J + \alpha)}. \tag{3.20}$$

This distribution is also known as the Chinese restaurant process (CRP) [1]. The CRP is a process that generates a partition of a set of N objects. The CRP utilizes the principle of *rich gets richer* and can be described by how people is seated in a Chinese restaurant. Imagine a Chinese restaurant with an infinite

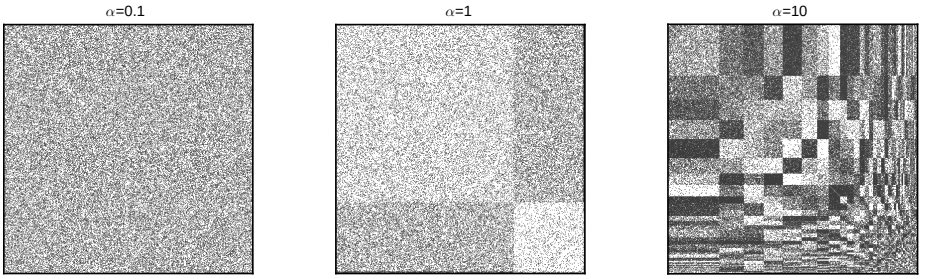

Figure 3.3: Effect of the hyperparameter α. Graphs with 500 nodes are generated with $\alpha = 0.1$ (left), $\alpha = 1$ (middle) and $\alpha = 10$ (right) and sorted according to the clustering. The other hyperparameters are kept fixed at $[\beta^+, \beta^-] = [1, 1]$.

number of tables with infinite capacity. When the first costumer arrives he is seated at table 1. When the second costumer arrives he is seated at table 1 with probability $\frac{1}{1+\alpha}$ or at an un-occupied table with probability $\frac{\alpha}{1+\alpha}$. In general, when the i-th costumer arrives he is seated at an un-occupied table with probability $\frac{\alpha}{i-1+\alpha}$ or at table k with probability $\frac{n_k}{i-1+\alpha}$, where n_k is the number of costumers already seated at table k. The CRP is exchangeable, meaning that the partitioning of nodes does not depend on the order the nodes are assigned to the clusters, but is only dependent on the size of the clusters, allowing the model to partition the nodes into as many clusters as necessary to explain the data. This non-parametric extension of the SBM is called the infinite relational model (IRM) and was first introduced by Kemp et al. [76, 163].

The hyperparameter α for the CRP is a hyper-parameter that controls the probability of generating a new cluster compared to the assignment of nodes to existing clusters. If α takes on a large value, a new cluster is more likely generated resulting in many small clusters. In contrast, if α takes on a small value nodes are more likely assigned to existing clusters, resulting in few large clusters. The effect of α when generating data using the IRM is illustrated in Figure 3.3.

The hyperparameters β^+ and β^- control the within and between cluster link-densities. β^+ is the pseudo link count within and between clusters and β^- is the pseudo non-link count within and between clusters. Figure 3.4 illustrates how the values of β^+ and β^- affect the structure of the generated graphs. The hyperparameters can be set *a priori* (Paper A and B) or be estimated using Metropolis-Hastings sampling (Paper C). The IRM can further be extended to account for integer weighted graphs by substituting the beta and Bernoulli distributions with gamma and Poisson distributions [127].

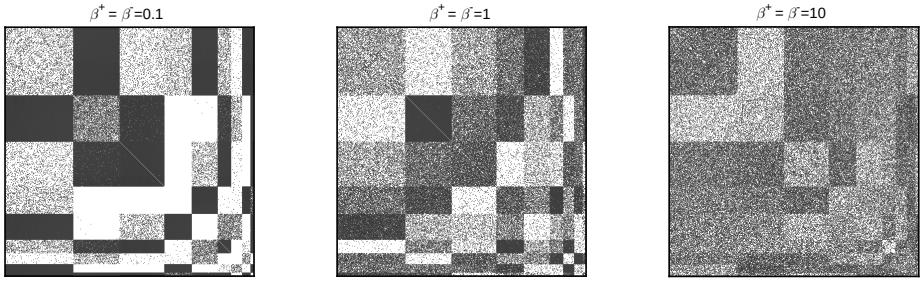

Figure 3.4: Effect of the hyperparameters β^+ and β^-. Graphs with 500 nodes are generated with $\beta^+ = \beta^- = 0.1$ (left), $\beta^+ = \beta^- = 1$ (middle) and $\beta^+ = \beta^- = 10$ (right) and sorted according to the clustering, which is kept fixed across graphs. Also, the hyperparameter α is kept fixed at $\alpha = 1$.

3.5 Model inference

The optimal partitioning of a graph is found by maximizing the likelihood function. The assignment vector $\mathbf{z}$ is inferred by Gibbs sampling as proposed in [75], in combination with split-merge sampling [60, 75, 104], each column at a time from the conditional posterior of the assignment of a single node as given by Equation (3.19). This section describes how the clustering of the networks can be inferred by sampling from the conditional posterior distribution.

3.5.1 The Metropolis-Hastings algorithm

The Metropolis-Hastings algorithm [55] is a MCMC approach to obtain a sequence of random samples from a probability distribution, when direct sampling is difficult. To obtain the sequence, samples are drawn from a proposal distribution $q(x)$, which is chosen to be sufficiently simple, such that samples can be drawn from it directly. The resulting sequence is used to approximate the true distribution $p(x)$ [19].

The algorithm is initialized by selecting an initial value x_i at random. A candidate value is drawn from the proposal distribution given the current state $q(x^*|x_i)$ and accepted with probability

$$A(x^*|x_i) = min\left(1, \frac{p(x^*)q(x_i|x^*)}{p(x_i)q(x^*|x_i)}\right). \tag{3.21}$$

If the candidate sample is accepted, then $x_{i+1} = x^*$, otherwise the candidate sample is discarded and $x_{i+1} = x_i$. When a candidate sample is discarded the previous value is copied with the result that the sequence has multiple copies of some samples. This sequence of samples form a Markov chain. Even if the candidate sample is discarded it is still used in the drawing of a new candidate sample $x^* = q(x|x_{i+1})$, in contrast to rejection sampling [19].

If the proposal distribution $q(x_A|x_B)$ is positive for any value of x_A and x_B, the distribution of samples tends to the true distribution as $i \to \infty$. The samples in the sequence obtained using the Metropolis-Hastings algorithm are not independent as consecutive samples are highly correlated, but independence is approximated by only keeping every N^{th} sample in the sequence [19].

3.5.2 Gibbs sampling

Gibbs sampling [44] is a special case of the Metropolis-Hastings algorithm. Gibbs sampling is applicable when the conditional distribution of each variable is easier to sample from than the joint distribution, such that a sample from the conditional posterior distribution of each variable can be sampled in turn [19]. When using Gibbs sampling to sample from the conditional posterior distributions, as given by Equation (3.19), each node's assignment is updated sequentially according to the conditional posterior distribution given all other nodes' assignments.

3.5.3 Split-merge sampling

Because one node is updated at a time in Gibbs sampling, it may be difficult to merge two clusters or split one cluster into two. To overcome this problem a Metropolis-Hastings split-merge procedure is applied [60, 76]. In the split-merge procedure two nodes are selected at random. If the nodes are in different clusters, a new partition where the two clusters are merged is proposed. If the nodes are in the same cluster, Gibbs sampling restricted to the nodes of the considered group is used to split all the nodes in the cluster into two new clusters. The two selected nodes are assigned to two empty clusters and the rest of the nodes can be assigned either by random to these clusters or based on their conditional probability [27]. This new partition is referred to as the launch state. The launch state can be refined through restricted Gibbs sweeps, such that the final sweep provides the split proposal that becomes the new state in the Markov chain, if it is accepted with the Metropolis-Hastings acceptance probability as given by Equation (3.21).

3.6 Model evaluation

When analyzing structural brain connectivity, we may have multiple graphs from rescans of the same subject or graphs from different subjects that can be useful for model evaluation. To evaluate model performance the ability to predict unseen data can be quantified by test log-likelihood and the area under curve (AUC) of the receiver operator characteristics (ROC) curve. Furthermore, the reproducibility of a clustering can be assessed by normalized mutual information (NMI). In this section the model evaluation measures are described.

3.6.1 Predictive log-likelihood

If a partitioning of a graph $\boldsymbol{A}$ is inferred using the IRM, the ability to predict an unseen graph $\boldsymbol{A}^*$ can be measured by the predictive log-likelihood. The expected predictive log-likelihood is given by

$$\langle \log L(\boldsymbol{A}^* | \mathbf{z}, \boldsymbol{\eta}) \rangle = \sum_{i>j} \left[A^*_{ij} \langle \log(\eta_{z_i z_j}) \rangle + (1 - A^*_{ij}) \langle \log(1 - \eta_{z_i z_j}) \rangle \right], \quad (3.22)$$

In Paper A, η_{lm} is distributed according to the beta distribution with the parameters $N^+_{lm} + \beta^+$ and $N^-_{lm} + \beta^-$ specified from the training graph $\boldsymbol{A}$. By defining $\beta = \beta^+ + \beta^-$ and $N_{lm} = N^+_{lm} + N^-_{lm}$, the expected value of $\log(\eta_{z_i z_j})$ is given by

$$\langle \log(\eta_{z_i z_j}) \rangle = \psi(N^+_{lm} + \beta^+) - \psi(N_{lm} + \beta), \quad (3.23)$$

and the expected value of $\log(1 - \eta_{z_i z_j})$ is given by

$$\langle \log(1 - \eta_{z_i z_j}) \rangle = \psi(N^-_{lm} + \beta^-) - \psi(N_{lm} + \beta). \quad (3.24)$$

3.6.2 Link prediction scoring

The area under curve (AUC) of the receiver operator characteristics (ROC) curve [24] can be used to quantify a parcellation's ability to predict unseen

structural connectivity graphs. The AUC enables quantification of how well a given parcellation accounts for the structure in unseen data and thereby also enables the comparison of different parcellations and quantification of the utility of the structural units, as well as comparison to alternative non-parametric link prediction measures.

When doing link prediction scoring, using a parcellation, we used the expected value of the link probability between clusters in Paper A and B, $s_{ij}^{\text{Parcellation}} = \langle \eta_{z_i z_j} \rangle = \frac{N_{lm}^{+}+\beta^{+}}{N_{lm}+\beta}$ and simply the density of the training graph in Paper C, $s_{ij}^{\text{Parcellation}} = \frac{N_{lm}^{+}}{N_{lm}}$. By using these scores, as well as the scores for non-parametric link prediction measures given in section 3.6.3, AUC can be used to quantify how well the two classes of links and non-links are separated in an unseen graph $\boldsymbol{A}^{*}$. By thresholding these probabilities at different levels, the ROC of true positives versus false positives can be made and the area under this curve is a measure of how well a given parcellation predicts unseen data. AUC is bounded by [0,1], where an AUC score of 1 indicates a perfect separation of links and non-links and an AUC score of 0.5 indicates prediction no better than chance. The AUC is invariant to class-imbalance issues and is therefore widely used as a measure of performance in link-prediction tasks [92].

3.6.3 Non-parametric link prediction measures

Given the $J \times J$ adjacency matrix $\boldsymbol{A}$, the following non-parametric measures can be used to score for the existence of a link between node i and j [89, 24]. We define $d_i = \sum_j A_{ij}$ to be the degree of node i.

$$s_{ij}^{\text{Common Neighbor}} = \sum_t A_{it} A_{jt} \tag{3.25}$$

$$s_{ij}^{\text{Jaccard}} = \frac{\sum_t A_{it} A_{jt}}{J - \sum_t (1 - A_{it})(1 - A_{jt})} \tag{3.26}$$

$$s_{ij}^{\text{Adamic/Adar}} = \sum_t \frac{A_{it} A_{jt}}{\log(d_t)} \tag{3.27}$$

$$s_{ij}^{\text{Preferential Attachment}} = d_i d_j \tag{3.28}$$

$$s_{ij}^{\text{ShortestPath}} = \frac{1}{\text{ShortestPath}(\mathbf{A}, \text{i}, \text{j})}, \tag{3.29}$$

where $\text{ShortestPath}(\mathbf{A}, i, j)$ gives the shortest path between two nodes in the

network. These scores are averaged across training subjects and can be evaluated on test data by the use of AUC [24] as described in the previous section.

3.6.4 Normalised mutual information

Normalised mutual information (NMI) can be used to quantify the similarity between two partitions $\mathbf{z}$ and $\mathbf{z}'$. The partitions can be different cortical parcellations or inferred partitions obtained from different subjects or scanning sessions or from different runs of the models. In Paper A and B, NMI is used to measure the reproducibility of the IRM, whereas in Paper B and C, NMI is used to quantify the similarity between different cortical parcellations. Mutual information (MI) is defined as

$$MI(\mathbf{z}, \mathbf{z}') = \sum_{kk'} P(k, k') \log \left(\frac{P(k, k')}{P(k)P(k')}) \right), \tag{3.30}$$

where $P(k, k')$ is the probability that a node in cluster k in the first partition is in cluster k' in the second partition. There is various ways to normalize MI [98], but the approach used in this work is given by

$$NMI(\mathbf{z}, \mathbf{z}') = \frac{2 \cdot MI(\mathbf{z}, \mathbf{z}')}{MI(\mathbf{z}, \mathbf{z}) + MI(\mathbf{z}', \mathbf{z}')}. \tag{3.31}$$

NMI takes values between zero and one where one indicates that a permutation of the groups exists such that the partitions are identical, and zero indicates that the partitions are perfectly independent.

3.7 Cross-entropy

Cross entropy [130, 78] is an information theoretic measure to measure the proximity of two probability distributions, by measuring the average information needed to encode data from a "true" distribution $p(x)$ using a "surrogate" distribution $q(x)$. The cross entropy (H) is given by

$$H(p(x), q(x)) = H(p(x)) + D_{KL}(p(x) \| q(x)) = -\sum_{x} p(x) \log(q(x)), \tag{3.32}$$

where $H(p(x))$ is the entropy of $p(x)$ and $D_{KL}(p(x)\|q(x))$ is the Kullback-Leibler divergence from $q(x)$ to $p(x)$.

In Paper D, cross entropy is used to measure the similarity between a probability distribution of relative connections from region j to all other regions derived from invasive tracer injections $\boldsymbol{\theta}_j^{tracer}$ and one derived from tractography $\boldsymbol{\theta}_j^{diffusion}$, where $\boldsymbol{\theta}_j^{tracer}$ is assumed ground truth. The cross-entropy between the distributions is given by

$$H(\boldsymbol{\theta}_j^{tracer}, \boldsymbol{\theta}_j^{diffusion}) = -\sum_i \theta_{ij}^{tracer} \log(\theta_{ij}^{diffusion}), \tag{3.33}$$

where the j index is the target region and the i index is the source region. The relative tracer probabilities $\boldsymbol{\theta}_j^{tracer}$ is given directly by the extrinsic fraction of labeled neurons (FLNe) provided in the tracer graph by Markov et al. [96]. The FLNe of a region is calculated as the total number of labeled neurons in that region relative to the total number of labeled neurons minus the number of labeled neurons intrinsic to the injected area. The distribution of relative streamline probabilities $\boldsymbol{\theta}_j^{diffusion}$ is derived from the structural connectivity graph. However, in order to calculate the cross entropy, the distribution has to be estimated robustly, as cross-entropy is not defined in regions with zero streamline probability. To solve this problem, Bayesian inference is used to infer $\boldsymbol{\theta}_j^{diffusion}$ in Paper D.

The prior probability of a streamline reaching one of the K regions is modelled by a Dirichlet distribution with the parameter $\boldsymbol{\tau}_j$ defined by the relative size $\boldsymbol{V}$ of the K source regions. The number of connections between source region i and target region j is modelled by a multinomial distribution, where each of the connections has the probability distribution $\boldsymbol{\theta}_j^{diffusion}$. The generative model is given by

$$\boldsymbol{\theta}_j^{diffusion} \sim Dir(\kappa_j \boldsymbol{\tau}_j), \qquad \tau_{ij} = \frac{V_i}{\sum_{i' \neq j} V_i'} \tag{3.34}$$

$$\mathbf{a}_j \sim Mult(\boldsymbol{\theta}_j^{diffusion}, N_j), \tag{3.35}$$

where κ_j is a scaling factor specifying the confidence of the prior and N_j is the total number of connections between all source regions and target region j. Since Dirichlet is the conjugate prior to the Multinomial distribution, $\boldsymbol{\theta}_j^{diffusion}$ can be integrated out analytically

$$p(\mathbf{a_j}|\kappa_j\boldsymbol{\tau}_j) = \int p(\mathbf{a}_j \mid \boldsymbol{\theta}_j^{diffusion}) p(\boldsymbol{\theta}_j^{diffusion} \mid \kappa_j\boldsymbol{\tau}_j) d\boldsymbol{\theta}_j^{diffusion} \tag{3.36}$$

$$= \frac{N_j!}{\prod_{i'\neq j} a_{i'j}!} \frac{B(\mathbf{a}_j + \kappa_j\boldsymbol{\tau}_j)}{B(\kappa_j\boldsymbol{\tau}_j)}. \tag{3.37}$$

The value of κ_j is found by optimizing $\log(p(\mathbf{a_j}|\kappa_j\boldsymbol{\tau}_j))$ using the minimum bound optimization *fminbnd* in Matlab v. 8.5.1 (The MathWorks Inc., Natick, MA, 2000). To ensure that κ_j always is positive and never has more influence than the diffusion data, κ_j is constrained to the interval $[0, \sum_{i'\neq j} a_{i'j}]$.

The posterior distribution of $\boldsymbol{\theta}_j^{diffusion}$ is found using Bayes' theorem

$$p(\boldsymbol{\theta}_j^{diffusion}|\mathbf{a}_j, \kappa_j, \boldsymbol{\tau}_j) = \frac{p(\mathbf{a}_j \mid \boldsymbol{\theta}_j^{diffusion}) p(\boldsymbol{\theta}_j^{diffusion} \mid \kappa_j\boldsymbol{\tau}_j)}{\int p(\mathbf{a}_j \mid \boldsymbol{\theta}_j^{diffusion}) p(\boldsymbol{\theta}_j^{diffusion} \mid \kappa_j\boldsymbol{\tau}_j) d\boldsymbol{\theta}_j^{diffusion}} \tag{3.38}$$

$$= Dir(\mathbf{a}_j + \kappa_j\boldsymbol{\tau}_j). \tag{3.39}$$

As an estimate of the of the relative streamline probabilities we used the expected value of $\boldsymbol{\theta}_j^{diffusion}$

$$\langle \boldsymbol{\theta}_j^{diffusion} \rangle = w_j\mathbf{r}_j + (1 - w_j)\boldsymbol{\tau}_j, \tag{3.40}$$

where

$$\tau_{ij} = \frac{V_i}{\sum_{i'\neq j} V_{i'}} \tag{3.41}$$

$$r_{ij} = \frac{a_{ij}}{\sum_{i'\neq j} a_{i'j}} \tag{3.42}$$

$$w_j = \frac{\sum_{i'\neq j} a_{i'j}}{\sum_{i'\neq j}(a_{i'j}) + \kappa_j} \tag{3.43}$$

$$(1 - w_j) = \frac{\kappa_j}{\sum_{i'\neq j}(a_{i'j}) + \kappa_j}. \tag{3.44}$$

Chapter 4

Summary of main results

This chapter describes the main findings of the four manuscripts included in this thesis.

4.1 Paper 1: Comparing Structural Brain Connectivity by the Infinite Relational Model

4.1.1 Motivation

During the last decades there has been a growing interest in modeling brain connectivity [134, 153], but until now the structural organization of the brain, derived using tractography, has primarily been characterized using graph theoretic measures [14, 54, 53] or using modularity [108, 87], that only consider the within-cluster link-densities instead of the full connectivity profile. With the growing focus on modeling whole-brain connectivity, there is a need for powerful and reliable statistical modeling tools that can extract the latent structure in the graphs, as well as compare connectivity graphs across subjects, scannings and modalities. In this paper we examine the Infinite Relational Model (IRM) as a tool to extract the latent structure in structural brain connectivity graphs

by comparing the structure derived from graphs from different subjects and the structure derived from the same subject, but from different scanning sessions.

4.1.2 Main findings

We proposed and demonstrated a framework for comparing brain connectivity graphs based on the structure inferred by the IRM. We used the IRM to extract the latent structure of six structural connectivity graphs from five different subjects. The similarity between the inferred structure both within and between subjects, as well as the predictive performance between subjects, are well above random, suggesting a common structural organization amongst subjects. The results indicate that the inferred structure is more consistent within subjects, i.e. between graphs from the same subject, than between subjects. However, the predictive performance of the model, assessed by predictive log-likelihood and AUC, is similar within and between subjects.

4.1.3 Considerations

The results presented herein are only based on six structural connectivity graphs from five different subjects, i.e. one re-scan. To confirm the result, that the structure within subjects is more similar than between subjects, more subjects and re-scans must be included. Furthermore, when using predictive performance to assess graph similarity, one should be aware that it is influenced by other factors, such as graph density.

The graphs used in this analysis were defined by a subdivision of a cortical atlas with 66 regions, resulting in 998 regions of interest [52]. Even if the initial number of nodes, i.e. 998, is above the number of cortical regions suggested by recent results [45], the employed parcellation may not be optimal to account for the brain's structural organization and hence may introduce a bias in the IRM-derived structure.

4.2 Paper 2: Nonparametric Bayesian Clustering of Structural Whole Brain Connectivity in Full Image Resolution

4.2.1 Motivation

Tractography based on dMRI enables estimation and mapping of the structural connectivity of the brain, the so-called connectome [51, 139]. To generate a structural connectivity graph, the nodes (i.e. regions of interest) have to be defined. Until now, the nodes have been defined by cortical atlases or subdivisions thereof. However, this may bias any structure derived using data-driven methods, as the employed parcellations may not optimally account for the structural connectivity of the brain. With the recent development in computational power, it is now possible to generate structural connectivity graphs at high resolution, i.e. defining the nodes by individual voxels on the GM-WM boundary, as opposed to grouping the voxels into larger parcels which are defined *a priori*. This approach, however, results in noisy and redundant graphs [138] and requires statistical models to extract this latent information. In this paper, we use the IRM to extract the latent structure of a high resolution graph, and investigate: 1) What is the statistically salient resolution of structural connectivity graphs? 2) How reliable can these salient structures be detected? 3) Are the derived structural units better at predicting connectivity than existing atlases?

4.2.2 Main findings

By using the IRM to extract the latent structure of high resolution brain connectivity graphs, we find that the statistically salient resolution is in the order of one thousand clusters. We also find that inferred structures are similar across repeated runs of the IRM, both within and between graphs, and also somewhat similar to two commonly used anatomical atlases, namely the Desikan-Kiliany [30] and the Destrieux atlas [31]. In addition, we find that the derived structure better predicts an independent structural connectivity graph derived from a re-scan of the same subject, than either the raw graph itself or the two anatomical atlases.

4.2.3 Considerations

We herein used the IRM to extract the latent structure of a structural connectivity graph at full image resolution. What full image resolution is can, however, be discussed as the structural T1-weighted image has higher spatial resolution than the diffusion weighted images. In the analysis only a single subject is included, as a one-to-one correspondence between subjects is needed to be able to compare subjects. When employing a cortical parcellation based on gross anatomical structures, the correspondance is a straight-forward problem, but as the resolution of the parcellation increases, a direct correspondence between subjects becomes challenging.

The estimated number of clusters is relatively high compared to recent suggestions [45]. This may indicate that the IRM overfits the data to some extent. Even though the IRM-extracted-structures predict a second connectivity graph from a re-scan of the same subject significantly better than both the raw (i.e. unclustered) graph and two anatomical atlases, the predictive performance when predicting an unseen subject was not investigated.

Furthermore, the MCMC sampler used in the inference procedure did not converge and the choice of the IRM hyperparameters was not investigated. Nonetheless the identified clusters were fairly robust to initialization, indicating that a better sampling strategy would not cause substantial changes in the results presented herein. Other factors that may influence the results are the quality of the data, i.e. spatial image resolution, angular resolution and b-value, as well as choice of diffusion model, tractography algorithm and parameters specific to those models.

4.3 Paper 3: Predictive Validation of Human Brain Parcellations

4.3.1 Motivation

Structural connectivity graphs derived using tractography are highly dependent on the cortical parcellation used to define the nodes [168]. It is very important to employ such a parcellation, either anatomically defined or data-driven, to eliminate noise and redundancy in brain connectivity graphs [138]. Multiple cortical parcellations exist, but the validation of these parcellations is difficult due to the absence of a true gold standard. In this paper we propose a framework

for quantitative validation of brain parcellations via statistical prediction on independent brain connectivity data. The framework is demonstrated on three cortical parcellations, namely two commonly used atlases based on surface morphology, the Desikan-Killiany [30] and the Destrieux atlas[31], and the recently proposed Human Connectome Project Multi-modality Parcellation [45], based on resting-state and task fMRI, cortical thickness and myelin. The parcellations are quantified by their ability to account for structural brain connectivity data and are compared to random parcellations and data-driven parcellations optimized to account for structural connectivity.

4.3.2 Main findings

In this paper we presented a statistical prediction framework to validate cortical brain parcellations and demonstrated its utility by testing it on three existing brain parcellations. We find that all three tested parcellations perform much better than random, but also that the multi-modal parcellation better accounts for the structural organization than the atlases based solely upon surface morphology, almost on par with the data-driven approaches optimized to account for structural connectivity. The performance of the data-driven approaches are on par with non-parametric link-predictors, indicating that no important information is lost when employing data-driven parcellations. Furthermore, the results show that structural connectivity inferred from a single subject has poor predictive performance compared to the structure inferred from a population. Finally, the results indicate that the structural connectivity is better characterized using more parcels than contained in the three tested atlases. The optimal resolution of a parcellation is, however, non-trivial as a broad range of resolutions provide similar predictive performance.

4.3.3 Considerations

The results presented herein may be biased by the data processing, such as the surface registration between subjects, and tractography biases. The structural connectivity graphs are derived from dMRI-based tractography which, just like any other connectivity estimation approach, has its challenges and limitations, which may influence the sensitivity and specificity of the estimated graph [69, 103, 84]. The impact of these biases is, however, hard to quantify, due to the lack of a gold-standard reference, and is undetectable by the presented framework, as they will be present in both training and test graphs. Despite all these challenges, we find that the three tested parcellations in general comply with

the structural connectivity data, suggesting a compliance between structural connectivity and other modalities.

As is common practice, the sensitivity/specificity balance is adjusted by thresholding the structural connectivity graphs [53, 54, 33]. However, as the ground truth is unknown, the optimal trade-off between the two cannot be assessed and unfortunately no threshold will result in both 100% sensitivity and 100% specificity [77, 167, 120, 36]. Nonetheless, the ranking of the three atlases is maintained across the three different threshold levels tested, suggesting that the proposed validation procedure is robust to the chosen threshold level.

4.4 Paper 4: Validation of Structural Brain Connectivity Networks

4.4.1 Motivation

The structural connectivity graphs generated with dMRI-based tractography are dependent on a comprehensive data processing pipeline [99, 71, 73, 62, 120]. In each step of the pipeline choices have to be made, from scanner acquisition-specific parameters through to fiber model, tractography algorithm and their respective parameters, to choices of thresholding and normalization of the structural connectivity graphs. Until now, the primary focus has been on the model-related parameter choices, i.e. fiber model, tractography algorithm, etc., though the possible influence of scanner acquisition parameters is also occasionally discussed [32, 9]. In this paper, we investigate how different scanner acquisition parameters, i.e. spatial resolution, angular resolution and b-value, influence the agreement between structural connectivity graphs derived from tractography and derived from retrograde invasive tracer injections in monkeys [96].

4.4.2 Main findings

We have quantified how structural connectivity graphs derived from tractography are dependent on chosen acquisition parameters, i.e. spatial resolution, angular resolution and b-value. We find that spatial resolution, angular resolution, as well as the interaction between the two and the interaction between spatial resolution and b-value, have a significant effect on the agreement with the tracer graph. Surprisingly, we find that structural connectivity graphs derived from low spatial resolution data is in better agreement with the tracer

graph, than those derived from high spatial resolution data. This suggests that the anatomical details available in the low spatial resolution data are sufficient to describe the tracer graph and the extra information available in the high spatial resolution data does not improve the agreement further. The result may be due to difference in the SNR, but further investigation is needed to confirm this claim. The similarity measure, cross entropy, used to compare the graphs from different modalities, show robustness to the level of threshold, whereas the optimal sensitivity/specificity trade-off is highly dependent on the applied threshold. Furthermore, we find that the agreement with the tracer graph is independent of the seeding strategy used.

4.4.3 Considerations

The results show that graphs derived from low spatial image resolution are in better agreement with the tracer graph, than those derived from high spatial resolution. The two resolutions are, however, difficult to compare directly as the SNR is different in the different datasets. Further investigation of how SNR influences the results are therefore needed to confirm or refute this result. In addition, the results may be improved by combining multiple spatial resolutions as suggested by [136], thereby utilizing the information available on all scales. Also, the integration step length in the tractography is different between spatial resolutions, though it did not seem to have a major influence on the results, in agreement with [29, 145].

Another consideration that may bias the result is the resolution of the employed parcellation, as it may be too coarse to differentiate appropriately between different combinations of the considered parameters. To rule out this effect, a tracer graph in higher resolution must be employed. The tracer graph by Markov et al. [96] used in this study is, however, the most detailed tracer connectivity study in monkeys currently available.

Chapter 5

General discussion and future perspectives

The work presented in this thesis shows the utility of statistical models to extract the latent structure from structural brain connectivity graphs derived from dMRI-based tractography. The parcellations derived using the SBM and the IRM are fairly robust, i.e. exhibit quite similar structure between restarts of the model, and account well for the structural connectivity, assessed by their ability to predict links in unseen structural connectivity graphs. The models are able to de-noise the structural connectivity graphs by aggregating nodes with similar connectivity patterns into homogeneous clusters. The de-noising is expressed by the superior predictive performance of the data-driven parcellations compared to the raw (unclustered) graph and two anatomical atlases based on surface-morphology (Paper B). It should, however, be noted that the sampler does not mix fully, which means that the optimal parcellation may not be found. This may be improved by better sampling strategies. Furthermore, the derived parcellations may be biased by a potential cortical parcellation employed to define the nodes in the graph (Paper A), as well as biases in the tractography. To overcome the biases introduced by an employed cortical parcellation, the structural connectivity graph can be generated in full image resolution, i.e. a node is defined as a voxel on the GM-WM boundary (Paper B) or as a vertex on the WM surface (Paper C). Such a high resolution structural connectivity graph is, however, noisy and possesses high redundancy [138]. The results presented

herein show that the infinite relational model is capable of extracting a structure that better complies with structural connectivity than two anatomical atlases based solely upon surface morphology (Paper B). Additionally, we proposed a predictive validation framework for quantifying cortical parcellations, by their ability to account for structural connectivity, and tested it on three cortical parcellations (Paper C). It was found that all three atlases better account for structural connectivity than random parcellations, but also that the recently proposed multi-modal parcellation, based on task and resting-state fMRI, cortical thickness and myelin [45] has superior predictive performance over those based solely upon surface morphology. This suggests that the organization of structural connectivity is in compliance with other modalities. A limitation is that the tractography biases cannot be estimated by the predictive framework proposed herein, as they are present in both training and test graphs.

One way to quantify the tractography biases, as well as the impact of other methodological choices in the generation of structural brain connectivity graphs, is to validate the tractography results against results from invasive tracers. Tracer studies are, for ethical reasons, limited to animals studies, but can provide insight into the accuracy of the tractography derived graphs [36, 77, 143, 29, 151, 9, 32]. Multiple parameters of the processing pipeline used to generate structural brain connectivity graphs have already been investigated. These include, amongst others, choice of fiber model [143, 154], tractography algorithm [16] and FA threshold [16, 9, 29], and it was found that most of the parameters impact the derived network. Herein we have validated how different scan acquisition parameters, i.e. spatial resolution, angular resolution and b-value, influence the generated structural connectivity graph (Paper D). The results presented herein show, as expected, that the derived structural connectivity graph depends on the chosen scan acquisition parameters. Surprisingly, the results indicate that higher spatial resolution not improves the final structural connectivity graph. This indicate that the anatomical information available in low image resolution sufficiently describe the connections in the tracer graph. This may be because large WM tracts are identified in both spatial resolutions, because the low resolution data has higher SNR or because the analysis was performed using a coarse cortical parcellation. A possible way to improve the structural connectivity graphs derived from tractography is to combine to two spatial resolutions, thereby utilizing all the information available on both scales, as suggested in [136]. In addition, the combination of the three b-values may also very well improve the derived graph.

Because no commonly accepted pipeline for generating structural connectivity graphs exists, the results between studies are difficult to compare. Such a common pipeline may, however, not be reasonable to adapt as most of the methodological choices depend on the specific data. The choice of fiber model and tractography algorithm is likely to be dependent on the specific data. This

makes cross-comparison of studies difficult as one model may perform better in one dataset than in another. Also, one can speculate that the same fiber model or tractography algorithm is not appropriate for all values of the tested scan acquisition parameters. To validate the derived structural connectivity graph, the result of every step in the pipeline should be validated, such that data obtained with each combination of the scan acquisition parameters are modelled using the most appropriate model, and thus for each step the parameter choices for the specific data in hand should be optimized. In addition, it has been shown that the optimal settings depend on the specific WM tract under investigation [143].

5.1 Tractography biases

Structural connectivity graphs are derived from dMRI data by integrating the local estimates of fiber orientations obtained with tractography. Due to noise in the data and the aggregation of anatomical information into voxels, the derived structural connectivity graphs contain numerous false positives and false negatives, which are difficult to quantify in the absence of a gold-standard reference.

To minimize the number of false positive connections, we applied a uniform streamline count threshold, as common practice [53, 54, 33]. However, it is known that varying the threshold value changes the balance between the sensitivity and the specificity of the graph [77, 167, 120, 36]. Another recently suggested approach is to threshold the graphs based on the appearance of a streamline across a population, instead of thresholding based on the streamline counts [123]. The results presented herein (Paper C and D) show, however, the same general results, independent of a wide range of applied thresholds.

Another known tractography bias is the tendency of streamlines to terminate in gyral crowns instead of sulcal walls, the so-called gyral bias [152, 122], which is not seen when mapping connectivity using invasive tracers [152]. To further complicate matters, the structural connectivity graphs estimated using tractography are in general more sparse than those derived using invasive tracers, because of the very dense superficial WM that prevents the detection of long range connections [122]. Although it has been shown that the gyral bias exists, correcting for this bias, as done in [32], only results in a minor increase in the sensitivity/specificity trade-off. Specifically a trade-off occurring at 65% for GM seeding and 67% for WM seeding. In comparison, the results in Paper D, without correction for gyral bias, were between 59-63% for both seeding strategies, depending on the specific combination of scan acquisition parameters. Thus, correction of this bias may improve accuracy, but it does not seem to be a bias with great influence on the derived structural connectivity graph. One expla-

nation why correction of the gyral bias does not seem to have a great impact may be due to the fact that the employed cortical parcellation is very coarse and hence the bias is averaged out across a region.

5.2 Future perspectives

Even though dMRI-based tractography is limited and quantification of the inevitable biases is difficult, it forms an important window into the structural connectivity of the brain and I believe that knowledge obtained from tractography studies can help improve diagnosis and treatment of diseases owing to white matter changes. In this work I investigated how different scan acquisition parameters influenced the derived structural connectivity graph. However, further investigation of how different parameters influence the derived graph and validation hereof is still needed, as well as further development of MRI hardware, sequences, models and more extensive tracer studies to validate the derived structural connectivity graphs.

I believe that the statistical models and the proposed prediction framework presented herein are promising tools for de-noising brain connectivity graphs, identifying the brain's structural organization and for comparing brain connectivity data in general. In future work, the data-driven parcellations should be derived on a larger cohort of subjects using multi-modalities, as the inclusion of other modalities may reduce some of the tractography biases. Furthermore, I envision to evaluate future prospective atlases using the prediction framework potentially including other modalities. In addition, future development of the prediction framework may be useful in the comparison and classification of populations, as well as assessing longitudinal effects of, for example, ageing, maturation and medical treatment.

Bibliography

[1] Aldous, D. Exchangeability and related topics. *École d'Été de Probabilités de Saint-Flour XIII—1983* (1985), 1–198.

[2] Alexander, D. C. Maximum entropy spherical deconvolution for diffusion MRI. *Biennial International Conference on Information Processing in Medical Imaging 19* (2005), 76–87.

[3] Alexander, D. C., Hubbard, P. L., Hall, M. G., Moore, E. A., Ptito, M., Parker, G. J. M., and Dyrby, T. B. Orientationally invariant indices of axon diameter and density from diffusion MRI. *NeuroImage 52*, 4 (2010), 1374–1389.

[4] Alexander, D. C., Pierpaoli, C., Basser, P. J., and Gee, J. C. Spatial transformations of diffusion tensor magnetic resonance images. *IEEE Trans Med Imaging 20*, 11 (2001), 1131–1139.

[5] Andersen, K. W., Madsen, K. H., Siebner, H. R., Schmidt, M. N., Mørup, M., and Hansen, L. K. Non-parametric Bayesian graph models reveal community structure in resting state fMRI. *NeuroImage 100* (2014), 301–315.

[6] Andersson, J. L. R., Skare, S., and Ashburner, J. How to correct susceptibility distortions in spin-echo echo-planar images: Application to diffusion tensor imaging. *NeuroImage 20*, 2 (2003), 870–888.

[7] Andersson, J. L. R., and Sotiropoulos, S. N. An integrated approach to correction for off-resonance effects and subject movement in diffusion MR imaging. *NeuroImage 125* (2015), 1063–1078.

[8] Axer, H. Invasive methods for tracing white matter architecture. *Diffusion MRI: Theory, Methods, and Applications* (2011), 31–42.

[9] Azadbakht, H., Parkes, L. M., Haroon, H. A., Augath, M., Logothetis, N. K., de Crespigny, E., D'Arceuil, H. E., Parker, G. J. M., Logothetis, N. K., Eschenko, O., and Others. Validation of High-Resolution Tractography Against In Vivo Tracing in the Macaque Visual Cortex. *Cerebral Cortex 45* (2015), 134–136.

[10] Baldassano, C., Beck, D. M., and Fei-Fei, L. Parcellating connectivity in spatial maps. *PeerJ 3* (2015), e784.

[11] Bammer, R., Markl, M., Barnett, A., Acar, B., Alley, M. T., Pelc, N. J., Glover, G. H., and Moseley, M. E. Analysis and generalized correction of the effect of spatial gradient field distortions in diffusion-weighted imaging. *Magnetic Resonance in Medicine 50*, 3 (2003), 560–569.

[12] Basser, P., Mattiello, J., and Lebihan, D. Estimation of the Effective Self-Diffusion Tensor from the NMR Spin Echo, 1994.

[13] Basser, P., Mattiello, J., and LeBihan, D. MR Diffusion Tensor Spectroscopy and Imaging. *Biophysical journal 66*, 1 (1994), 259–267.

[14] Bassett, D. S., and Bullmore, E. Small-world brain networks. *NEUROSCIENTIST 12*, 6 (2006), 512–523.

[15] Bassett, D. S., Bullmore, E. T., Meyer-Lindenberg, A., Apud, J. a., Weinberger, D. R., and Coppola, R. Cognitive fitness of cost-efficient brain functional networks. *Proceedings of the National Academy of Sciences of the United States of America 106*, 28 (2009), 11747–52.

[16] Bastiani, M., Shah, N. J., Goebel, R., and Roebroeck, A. Human cortical connectome reconstruction from diffusion weighted MRI: the effect of tractography algorithm. *Neuroimage 62*, 3 (2012), 1732–1749.

[17] Behrens, T., Berg, H., Jbabdi, S., Rushworth, M., and Woolrich, M. Probabilistic diffusion tractography with multiple fibre orientations: What can we gain? *NeuroImage 34*, 1 (2007), 144–55.

[18] Behrens, T. E. J., Woolrich, M. W., Jenkinson, M., Johansen-Berg, H., Nunes, R. G., Clare, S., Matthews, P. M., Brady, J. M., and Smith, S. M. Characterization and propagation of uncertainty in diffusion-weighted MR imaging. *Magnetic resonance in medicine 50*, 5 (2003), 1077–1088.

[19] Bishop, C. M. *Pattern recognition and machine learning*. Springer, 2006.

[20] Braitenberg, V., and Schüz, A. *Anatomy of the cortex: Statistics and geometry.* Springer-Verlag Publishing, 1991.

[21] Brodmann, K. *Vergleichende Lokalisationslehre der Groshirnrinde.* Barth, 1909.

[22] Brown, R. Xxvii. a brief account of microscopical observations made in the months of june, july and august 1827, on the particles contained in the pollen of plants; and on the general existence of active molecules in organic and inorganic bodies. *Philosophical Magazine Series 2 4*, 21 (1828), 161–173.

[23] Calabrese, E., Badea, A., Cofer, G., Qi, Y., and Johnson, G. A. A Diffusion MRI tractography connectome of the mouse brain and comparison with neuronal tracer data. *Cerebral Cortex 25*, 11 (2015), 4628–4637.

[24] Clauset, A., Moore, C., and Newman, M. E. J. Hierarchical structure and the prediction of missing links in networks. *Nature 453*, 7191 (2008), 98–101.

[25] Conturo, T. E., Lori, N. F., Cull, T. S., Akbudak, E., Snyder, A. Z., Shimony, J. S., McKinstry, R. C., Burton, H., and Raichle, M. E. Tracking neuronal fiber pathways in the living human brain. *Proceedings of the National Academy of Sciences of the United States of America 96*, 18 (1999), 10422–7.

[26] Cook, P. a., Bai, Y., Seunarine, K. K., Hall, M. G., Parker, G. J., and Alexander, D. C. Camino: Open-Source Diffusion-MRI Reconstruction and Processing. *14th Scientific Meeting of the International Society for Magnetic Resonance in Medicine 14* (2006), 2759.

[27] Dahl, D. B. Sequentially-allocated merge-split sampler for conjugate and nonconjugate Dirichlet process mixture models. *Journal of Computational and Graphical Statistics 11* (2005).

[28] D'Arceuil, H. E., Westmoreland, S., and de Crespigny, A. J. An approach to high resolution diffusion tensor imaging in fixed primate brain. *NeuroImage 35*, 2 (2007), 553–565.

[29] Dauguet, J., Peled, S., Berezovskii, V., Delzescaux, T., Warfield, S. K., Born, R., and Westin, C.-F. Comparison of fiber tracts derived from in-vivo DTI tractography with 3D histological neural tract tracer reconstruction on a macaque brain. *Neuroimage 37*, 2 (2007), 530–538.

[30] Desikan, R. S., Ségonne, F., Fischl, B., Quinn, B. T., Dickerson, B. C., Blacker, D., Buckner, R. L., Dale, A. M., Maguire, R. P., Hyman, B. T., and Others. An automated labeling system for subdividing the human cerebral cortex on MRI scans into gyral based regions of interest. *Neuroimage 31*, 3 (2006), 968–980.

[31] Destrieux, C., Fischl, B., Dale, A., and Halgren, E. Automatic parcellation of human cortical gyri and sulci using standard anatomical nomenclature. *Neuroimage 53*, 1 (2010), 1–15.

[32] Donahue, C. J., Sotiropoulos, S. N., Jbabdi, S., Hernandez-Fernandez, M., Behrens, T. E., Dyrby, T. B., Coalson, T., Kennedy, H., Knoblauch, K., Essen, D. C. V., and Glasser, M. F. Using Diffusion Tractography to Predict Cortical Connection Strength and Distance: A Quantitative Comparison with Tracers in the Monkey. *The Journal of Neuroscience 36*, 25 (2016), 6758–6770.

[33] Drakesmith, M., Caeyenberghs, K., Dutt, A., Lewis, G., David, A. S., and Jones, D. K. Overcoming the effects of false positives and threshold bias in graph theoretical analyses of neuroimaging data. *NeuroImage 118* (2015), 313–333.

[34] Dyrby, T. B., Baaré, W. F. C., Alexander, D. C., Jelsing, J., Garde, E., and Søgaard, L. V. An ex vivo imaging pipeline for producing high-quality and high-resolution diffusion-weighted imaging datasets. *Human Brain Mapping 32*, 4 (2011), 544–563.

[35] Dyrby, T. B., Lundell, H. M., Liptrot, M. G., Burke, M. W., Ptito, M., and Siebner, H. R. Interpolation of DWI prior to DTI reconstruction, and its validation. In *Proc. Intl. Soc. Mag. Reson. Med* (2011), vol. 19.

[36] Dyrby, T. B., Søgaard, L. V., Parker, G. J., Alexander, D. C., Lind, N. M., Baaré, W. F. C., Hay-Schmidt, A., Eriksen, N., Pakkenberg, B., Paulson, O. B., and Jelsing, J. Validation of in vitro probabilistic tractography. *NeuroImage 37*, 4 (2007), 1267–1277.

[37] Edgar, J. M., and Griffiths, I. R. *White Matter Structure. A Microscopist's View.*, second ed. Elsevier, 2013.

[38] Eickhoff, S. B., Bzdok, D., Laird, A. R., Roski, C., Caspers, S., Zilles, K., and Fox, P. T. Co-activation patterns distinguish cortical modules, their connectivity and functional differentiation. *Neuroimage 57*, 3 (2011), 938–949.

[39] Einstein, a. Über die von der molekularkinetischen Theorie der Wärme geforderte Bewegung von in ruhenden Flüssigkeiten suspendierten Teilchen. *Ann. d. Phys. 322*, 8 (1905), 549–560.

[40] Fan, L., Li, H., Zhuo, J., Zhang, Y., Wang, J., Chen, L., Yang, Z., Chu, C., Xie, S., Laird, A. R., and Others. The Human Brainnetome Atlas: A New Brain Atlas Based on Connectional Architecture. *Cerebral Cortex* (2016), bhw157.

[41] Fiala, J. C., and Harris, K. M. *Dendrite structure*. Oxford University Press Inc., NY, NY, 1999.

[42] Fischl, B., van der Kouwe, A., Destrieux, C., Halgren, E., Ségonne, F., Salat, D. H., Busa, E., Seidman, L. J., Goldstein, J., Kennedy, D., and Others. Automatically parcellating the human cerebral cortex. *Cerebral cortex 14*, 1 (2004), 11–22.

[43] Friedman, D. I., Kelly Johnson, J., Chorsky, R. L., and Stopa, E. G. Labeling of human retinohypothalamic tract with the carbocyanine dye, DiI. *Brain Research 560*, 1-2 (1991), 297–302.

[44] Geman, S., and Geman, D. Stochastic relaxation, Gibbs distributions, and the Bayesian restoration of images. *IEEE Transactions on Pattern Analysis and Machine Intelligence 6*, 1 (1984), 721–741.

[45] Glasser, M. F., Coalson, T. S., Robinson, E. C., Hacker, C. D., Harwell, J., Yacoub, E., Ugurbil, K., Andersson, J., Beckmann, C. F., Jenkinson, M., Smith, S. M., and Van Essen, D. C. A multi-modal parcellation of human cerebral cortex. *Nature 536*, 7615 (2016), 171–8.

[46] Glasser, M. F., Sotiropoulos, S. N., Wilson, J. A., Coalson, T. S., Fischl, B., Andersson, J. L., Xu, J., Jbabdi, S., Webster, M., Polimeni, J. R., and Others. The minimal preprocessing pipelines for the Human Connectome Project. *Neuroimage 80* (2013), 105–124.

[47] Gong, G., He, Y., Concha, L., Lebel, C., Gross, D. W., Evans, A. C., and Beaulieu, C. Mapping anatomical connectivity patterns of human cerebral cortex using in vivo diffusion tensor imaging tractography. *Cerebral cortex 19*, 3 (2009), 524–536.

[48] Gong, G., Rosa-Neto, P., Carbonell, F., Chen, Z. J., He, Y., and Evans, A. C. Age- and gender-related differences in the cortical anatomical network. *The Journal of Neuroscience 29*, 50 (2009), 15684–93.

[49] Graf, v. K. D., and Schramm, U. Diameter of axons and thickness of myelin sheaths of the pyramidal tract fibres in the adult human medullary pyramid. *Anatomischer Anzeiger 157*, 2 (1983), 97–111.

[50] Greve, D. N., and Fischl, B. Accurate and robust brain image alignment using boundary-based registration. *NeuroImage 48*, 1 (2009), 63–72.

[51] Hagmann, P. *From diffusion MRI to brain connectomics*. PhD thesis, Institut de traitement des signaux PROGRAMME DOCTORAL EN INFORMATIQUE ET COMMUNICATIONS POUR L'OBTENTION DU GRADE DE DOCTEUR {È}S SCIENCES PAR Docteur en médecine, Université de Lausanne, 2005.

[52] Hagmann, P., Cammoun, L., Gigandet, X., Meuli, R., Honey, C., Wedeen, V., and Sporns, O. Mapping the structural core of human cerebral cortex. *PLoS biology 6*, 7 (2008), e159.

[53] Hagmann, P., Cammoun, L., Gigandet, X., Meuli, R., Honey, C. J., Wedeen, V. J., and Sporns, O. Mapping the structural core of human cerebral cortex. *PLoS biology 6*, 7 (2008), e159.

[54] Hagmann, P., Kurant, M., Gigandet, X., Thiran, P., Wedeen, V. J., Meuli, R., and Thiran, J.-P. Mapping human whole-brain structural networks with diffusion MRI. *PloS one 2*, 7 (2007), e597.

[55] Hastings, W. K. Monte Carlo Sampling Methods Using Markov Chains and Their Applications. *Biometrika 57*, 1 (1970), 97–109.

[56] Holland, P. P. W., Laskey, K. K. B., and Leinhardt, S. Stochastic blockmodels: First steps. *Social Networks 5*, 2 (1983), 109–137.

[57] Iturria-Medina, Y., Canales-Rodríguez, E. J., Melie-García, L., Valdés-Hernández, P. A., Martínez-Montes, E., Alemán-Gómez, Y., and Sánchez-Bornot, J. M. Characterizing brain anatomical connections using diffusion weighted MRI and graph theory. *NeuroImage 36*, 3 (2007), 645–660.

[58] Iturria-Medina, Y., Sotero, R. C., Canales-Rodríguez, E. J., Alemán-Gómez, Y., and Melie-García, L. Studying the human brain anatomical network via diffusion-weighted MRI and Graph Theory. *Neuroimage 40*, 3 (2008), 1064–1076.

[59] Jahanshad, N., Nir, T. M., Toga, A. W., Jack, C. R., Bernstein, M. A., Weiner, M. W., and Thompson, P. M. Seemingly unrelated regression empowers detection of network failure in dementia. *Neurobiology of Aging 36*, S1 (2015), S103–S112.

[60] Jain, S., and Neal, R. M. R. A Split-Merge Markov Chain Monte Carlo Procedure for the Dirichlet Process Mixture Model. *Journal of Computational and Graphical Statistics 13*, 1 (2004), 158–182.

[61] Jbabdi, S., and Johansen-Berg, H. Tractography: Where Do We Go from Here? *Brain Connectivity 1*, 3 (2011), 169–183.

[62] Jbabdi, S., Sotiropoulos, S. N., Haber, S. N., Van Essen, D. C., Behrens, T. E., Essen, D. C. V., and Behrens, T. E. Measuring macroscopic brain connections in vivo. *Nature Neuroscience 18*, 11 (2015), 1546–1555.

[63] Jenkinson, M., Beckmann, C. F., Behrens, T. E. J., Woolrich, M. W., and Smith, S. M. Fsl. *Neuroimage 62*, 2 (2012), 782–790.

[64] Jenkinson, M., Beckmann, C. F., Behrens, T. E. J., Woolrich, M. W., and Smith, S. M. Fsl. *NeuroImage 62*, 2 (2012), 782–790.

[65] Jeurissen, B., Leemans, A., Tournier, J. D., Jones, D. K., and Sijbers, J. Investigating the prevalence of complex fiber configurations in white matter tissue with diffusion magnetic resonance imaging. *Human Brain Mapping 34*, 11 (2013), 2747–2766.

[66] Jezzard, P., and Balaban, R. S. Correction for geometric distortion in echo planar images from B0 field variations. *Magnetic resonance in medicine 34*, 1 (1995), 65–73.

[67] Johansen-Berg, H., and Behrens, T. E. *Diffusion MRI: from quantitative measurement to in vivo neuroanatomy*. Academic Press, 2013.

[68] Jones, D. K. The Effect of Gradient Sampling Schemes on Measures Derived from Diffusion Tensor MRI: A Monte Carlo Study. *Magnetic Resonance in Medicine 51*, 4 (2004), 807–815.

[69] Jones, D. K. Challenges and limitations of quantifying brain connectivity in vivo with diffusion MRI. *Imaging in Medicine 2*, 3 (2010), 341–355.

[70] Jones, D. K., and Basser, P. J. "Squashing peanuts and smashing pumpkins": How noise distorts diffusion-weighted MR data. *Magnetic Resonance in Medicine 52*, 5 (2004), 979–993.

[71] Jones, D. K., and Cercignani, M. Twenty-five pitfalls in the analysis of diffusion MRI data. *NMR in Biomedicine 23*, 7 (2010), 803–820.

[72] Jones, D. K., Horsfield, M. A., and Simmons, A. Optimal strategies for measuring diffusion in anisotropic systems by magnetic resonance imaging. *Magnetic Resonance in Medicine 42*, 3 (1999), 515–525.

[73] Jones, D. K., Knösche, T. R., and Turner, R. White matter integrity, fiber count, and other fallacies: the do's and don'ts of diffusion MRI. *Neuroimage 73* (2013), 239–254.

[74] Jovicich, J., Czanner, S., Greve, D., Haley, E., Van Der Kouwe, A., Gollub, R., Kennedy, D., Schmitt, F., Brown, G., MacFall, J., Fischl, B., and Dale, A. Reliability in multi-site structural MRI

studies: Effects of gradient non-linearity correction on phantom and human data. *NeuroImage 30*, 2 (2006), 436–443.

[75] Kemp, C., Tenenbaum, J., Griffiths, T., Yamada, T., and Ueda, N. Learning systems of concepts with an infinite relational model. *Proceedings of the national conference on artificial intelligence 21*, 1 (2006), 381–388.

[76] Kemp, C., Tenenbaum, J. B., Griffiths, T. L., Yamada, T., and Ueda, N. Learning systems of concepts with an infinite relational model. In *AAAI* (2006), vol. 3, p. 5.

[77] Knösche, T. R., Anwander, A., Liptrot, M., and Dyrby, T. B. Validation of tractography: Comparison with manganese tracing. *Human Brain Mapping 36*, 10 (2015), 4116–4134.

[78] Kullback, S., and Leibler, R. A. On information and sufficiency. *The annals of mathematical statistics 22*, 1 (1951), 79–86.

[79] Lance, G. N., and Williams, W. T. A general theory of classificatory sorting strategies. I. Hierarchical systems. *Computer Journal 9*, 4 (1967), 373–380.

[80] Lanciego, J. L., and Wouterlood, F. G. Neuroanatomical tract-tracing methods beyond 2000: What's now and next. *Journal of Neuroscience Methods 103*, 1 (2000), 1–2.

[81] Le Bihan, D., and Breton, E. Imagerie de diffusion in-vivo par résonance magnétique nucléaire. *Comptes-Rendus de l'Académie des Sciences 93*, 5 (1985), 27–34.

[82] Le Bihan, D., Breton, E., Lallemand, D., Grenier, P., Cabanis, E., and Laval-Jeantet, M. Mr imaging of intravoxel incoherent motions: application to diffusion and perfusion in neurologic disorders. *Radiology 161*, 2 (1986), 401–407.

[83] Le Bihan, D., Breton, E., Lallemand, D., Grenier, P., Cabanis, E., and Laval-Jeantet, M. MR imaging of intravoxel incoherent motions: application to diffusion and perfusion in neurologic disorders. *Radiology 161* (1986), 401–407.

[84] Le Bihan, D., Poupon, C., Amadon, A., and Lethimonnier, F. Artifacts and pitfalls in diffusion MRI. *Journal of magnetic resonance imaging 24*, 3 (2006), 478–488.

[85] Leemans, A., and Jones, D. K. The B-matrix must be rotated when correcting for subject motion in DTI data. *Magnetic Resonance in Medicine 61*, 6 (2009), 1336–1349.

[86] Leergaard, T. B., White, N. S., De Crespigny, A., Bolstad, I., D'Arceuil, H., Bjaalie, J. G., and Dale, A. M. Quantitative histological validation of diffusion MRI fiber orientation distributions in the rat brain. *PLoS ONE 5*, 1 (2010), 1–8.

[87] Lehmann, S., and Hansen, L. K. Deterministic modularity optimization. *European Physical Journal B 60*, 1 (2007), 83–88.

[88] Li, L., Rilling, J. K., Preuss, T. M., Glasser, M. F., and Hu, X. The effects of connection reconstruction method on the interregional connectivity of brain networks via diffusion tractography. *Human Brain Mapping 33*, 8 (2012), 1894–1913.

[89] Liben-Nowell, D., and Kleinberg, J. The link prediction problem for social networks. *International Conference on Information and Knowledge Management, Proceedings*, November 2003 (2003), 556–559.

[90] Liptrot, M. G., Sidaros, K., and Dyrby, T. B. Addressing the path-length-dependency confound in white matter tract segmentation. *PLoS ONE 9*, 5 (2014).

[91] Lo, C.-y., Wang, P.-n., Chou, K.-h., Wang, J., He, Y., and Lin, C.-p. Diffusion Tensor Tractography Reveals Abnormal Topological Organization in Structural Cortical Networks in Alzheimer's Disease. *Journal of Neuroscience 30*, 50 (2010), 16876–16885.

[92] Lu, L., Zhou, T., and Lü, L.; Zhou, T. Link Prediction in Complex Networks: A Survey. *Physica A: Statistical Mechanics and its Applications 390*, 6 (2011), 1150–1170.

[93] Lundell, H., Nielsen, J. B., Ptito, M., and Dyrby, T. B. Distribution of collateral fibers in the monkey cervical spinal cord detected with diffusion-weighted magnetic resonance imaging. *NeuroImage 56*, 3 (2011), 923–929.

[94] Mackay, D. Probable networks and plausible predictions—a review of practical Bayesian methods for supervised neural networks. *Network: Computation in Neural Systems 6*, 3 (1995), 469–505.

[95] Maier-Hein, K., Neher, P., Houde, J.-C., Cote, M.-A., Garyfallidis, E., Zhong, J., Chamberland, M., Yeh, F.-C., Lin, Y. C., Ji, Q., Reddick, W. E., Glass, J. O., Chen, D. Q., Feng, Y., Gao, C., Wu, Y., Ma, J., Renjie, H., Li, Q., Westin, C.-F., Deslauriers-Gauthier, S., Gonzalez, J. O. O., Paquette, M., St-Jean, S., Girard, G., Rheault, F., Sidhu, J., Tax, C. M. W., Guo, F., Mesri, H. Y., David, S., Froeling, M., Heemskerk, A. M., Leemans, A., Bore, A., Pinsard, B., Bedetti, C., Desrosiers, M., Brambati,

S., Doyon, J., Sarica, A., Vasta, R., Cerasa, A., Quattrone, A., Yeatman, J., Khan, A. R., Hodges, W., Alexander, S., Romascano, D., Barakovic, M., Auria, A., Esteban, O., Lemkaddem, A., Thiran, J.-P., Cetingul, H. E., Odry, B. L., Mailhe, B., Nadar, M., Pizzagalli, F., Prasad, G., Villalon-Reina, J., Galvis, J., Thompson, P., Requejo, F., Laguna, P., Lacerda, L., Barrett, R., Dell'Acqua, F., Catani, M., Petit, L., Caruyer, E., Daducci, A., Dyrby, T., Holland-Letz, T., Hilgetag, C., Stieltjes, B., Descoteaux, M., Hein, K. H. M., Neher, P., Christophe, J., and Alexandre, M. Tractography-based connectomes are dominated by false-positive connections. *bioRxiv* (2016), 1–23.

[96] Markov, N. T., Ercsey-Ravasz, M. M., Ribeiro Gomes, A. R., Lamy, C., Magrou, L., Vezoli, J., Misery, P., Falchier, A., Quilodran, R., Gariel, M. A., Sallet, J., Gamanut, R., Huissoud, C., Clavagnier, S., Giroud, P., Sappey-Marinier, D., Barone, P., Dehay, C., Toroczkai, Z., Knoblauch, K., Van Essen, D. C., and Kennedy, H. A weighted and directed interareal connectivity matrix for macaque cerebral cortex. *Cerebral Cortex 24*, 1 (2012), 17–36.

[97] Markov, N. T., Misery, P., Falchier, A., Lamy, C., Vezoli, J., Quilodran, R., Gariel, M. A., Giroud, P., Ercsey-Ravasz, M., Pilaz, L. J., Huissoud, C., Barone, P., Dehay, C., Toroczkai, Z., Van Essen, D. C., Kennedy, H., and Knoblauch, K. Weight consistency specifies regularities of macaque cortical networks. *Cerebral Cortex 21*, 6 (2011), 1254–1272.

[98] Martin, L. C., Gloor, G. B., Dunn, S. D., and Wahl, L. M. Using information theory to search for co-evolving residues in proteins. *Bioinformatics 21*, 22 (2005), 4116–4124.

[99] Meskaldji, D. E., Fischi-Gomez, E., Griffa, A., Hagmann, P., Morgenthaler, S., and Thiran, J. P. Comparing connectomes across subjects and populations at different scales. *NeuroImage 80* (2013), 416–425.

[100] Mori, S., Crain, B. J., Chacko, V. P., and Van Zijl, P. C. M. Three-dimensional tracking of axonal projections in the brain by magnetic resonance imaging. *Annals of Neurology 45*, 2 (1999), 265–269.

[101] Mori, S., Oishi, K., Jiang, H., Jiang, L., Li, X., Akhter, K., Hua, K., Faria, A. V., Mahmood, A., Woods, R., Toga, A. W., Pike, G. B., Neto, P. R., Evans, A., Zhang, J., Huang, H., Miller, M. I., van Zijl, P., and Mazziotta, J. Stereotaxic white matter atlas

based on diffusion tensor imaging in an ICBM template. *NeuroImage 40*, 2 (2008), 570–582.

[102] Mori, S., and van Zijl, P. Fiber tracking: principles and strategies - a technical review. *NMR in biomedicine 15*, 7-8 (2002), 468–480.

[103] Morris, D. M., Embleton, K. V., and Parker, G. J. M. Probabilistic fibre tracking: differentiation of connections from chance events. *Neuroimage 42*, 4 (2008), 1329–1339.

[104] Mørup, M., Madsen, K., Dogonowski, A., Siebner, H., and Hansen, L. Infinite relational modeling of functional connectivity in resting state fMRI. *Neural Information Processing Systems 23* (2010).

[105] Murre, J. M. J., and Sturdy, D. P. F. The connectivity of the brain: multi-level quantitative analysis. *Biological cybernetics 73*, 6 (1995), 529–545.

[106] Murtagh, F. A Survey of Recent Advances in Hierarchical Clustering Algorithms. *The Computer J. 26*, 4 (1983), 354–359.

[107] Newman, M., and Girvan, M. Finding and evaluating community structure in networks. *Physical Review E 69*, 2 (2004), 1–16.

[108] Newman, M. E. J. Modularity and community structure in networks. *Proceedings of the national academy of sciences 103*, 23 (2006), 8577–8582.

[109] Nilsson, M., Lätt, J., Ståhlberg, F., Westen, D., and Hagslätt, H. The importance of axonal undulation in diffusion mr measurements: a monte carlo simulation study. *NMR in Biomedicine 25*, 5 (2012), 795–805.

[110] Nowicki, K., and Snijders, T. A. B. Estimation and prediction for stochastic blockstructures. *Journal of the American Statistical Association 96*, 455 (2001), 1077–1087.

[111] Oishi, K., Zilles, K., Amunts, K., Faria, A., Jiang, H., Li, X., Akhter, K., Hua, K., Woods, R., Toga, A. W., Pike, G. B., Rosa-Neto, P., Evans, A., Zhang, J., Huang, H., Miller, M. I., van Zijl, P. C. M., Mazziotta, J., and Mori, S. Human brain white matter atlas: Identification and assignment of common anatomical structures in superficial white matter. *NeuroImage 43*, 3 (2008), 447–457.

[112] Papadakis, N. G., Xing, D., Houston, G. C., Smith, J. M., Smith, M. I., James, M. F., Parsons, A. A., Huang, C. L. H., Hall, L. D., and Carpenter, T. A. A study of rotationally invariant and symmetric indices of diffusion anisotropy. *Magnetic Resonance Imaging 17*, 6 (1999), 881–892.

[113] Parisot, S., Arslan, S., Passerat-Palmbach, J., Wells, W. M., and Rueckert, D. Group-wise parcellation of the cortex through multi-scale spectral clustering. *NeuroImage* (2016).

[114] Parker, G., Haroon, H., and Wheeler-Kingshott, C. A framework for a streamline-based probabilistic index of connectivity (PICo) using a structural interpretation of MRI diffusion measurements. *Journal of magnetic resonance imaging 18*, 2 (2003), 242–254.

[115] Parker, G. J. M., and Alexander, D. C. Probabilistic anatomical connectivity derived from the microscopic persistent angular structure of cerebral tissue. *Philosophical transactions of the Royal Society of London. Series B, Biological sciences 360*, 1457 (2005), 893–902.

[116] Parker, G. J. M., Stephan, K. E., Barker, G. J., Rowe, J. B., MacManus, D. G., Wheeler-Kingshott, C. a. M., Ciccarelli, O., Passingham, R. E., Spinks, R. L., Lemon, R. N., and Turner, R. Initial demonstration of in vivo tracing of axonal projections in the macaque brain and comparison with the human brain using diffusion tensor imaging and fast marching tractography. *NeuroImage 15*, 4 (2002), 797–809.

[117] Pierpaoli, C., and Basser, P. J. Toward a quantitative assessment of diffusion anisotropy. *Magnetic resonance in medicine : official journal of the Society of Magnetic Resonance in Medicine / Society of Magnetic Resonance in Medicine 36*, 6 (1996), 893–906.

[118] Pierpaoli, C., Jezzard, P., Basser, P. J., Barnett, A., and Di Chiro, G. Diffusion tensor mr imaging of the human brain. *Radiology 201*, 3 (1996), 637–648.

[119] Pierpaoli, C., Jezzard, P., Basser, P. J., Barnett, A., and Di Chiro, G. Diffusion tensor MR imaging of the human brain. *Radiology 201*, 3 (1996), 637–48.

[120] Qi, S., Meesters, S., Nicolay, K., ter Haar Romeny, B. M., and Ossenblok, P. The influence of construction methodology on structural brain network measures: A review. *Journal of Neuroscience Methods 253*, 500 (2015), 170–182.

[121] Reese, T. G., Heid, O., Weisskoff, R. M., and Wedeen, V. J. Reduction of eddy-current-induced distortion in diffusion MRI using a twice-refocused spin echo. *Magnetic Resonance in Medicine 49*, 1 (2003), 177–182.

[122] Reveley, C., Seth, A. K., Pierpaoli, C., Silva, A. C., Yu, D., Saunders, R. C., Leopold, D. a., and Ye, F. Q. Superficial white

matter fiber systems impede detection of long-range cortical connections in diffusion MR tractography. *Proceedings of the National Academy of Sciences* (2015), 201418198.

[123] Roberts, J. A., Perry, A., Roberts, G., Mitchell, P. B., and Breakspear, M. Consistency-based thresholding of the human connectome. *NeuroImage* (2016).

[124] Robinson, E. C., Hammers, A., Ericsson, A., Edwards, A. D., and Rueckert, D. Identifying population differences in whole-brain structural networks: A machine learning approach. *NeuroImage 50*, 3 (2010), 910–919.

[125] Savadjiev, P., Campbell, J. S. W., Descoteaux, M., Deriche, R., Pike, G. B., and Siddiqi, K. Labeling of ambiguous subvoxel fibre bundle configurations in high angular resolution diffusion MRI. *NeuroImage 41*, 1 (2008), 58–68.

[126] Schmahmann, J. D., and Pandya, D. *Fiber pathways of the brain.* OUP USA, 2009.

[127] Schmidt, M. N., and Morup, M. Nonparametric Bayesian Modeling of Complex Networks: An Introduction. *Signal Processing Magazine, IEEE 30*, 3 (2013), 110–128.

[128] Scholz, J., Klein, M. C., Behrens, T. E., and Johansen-Berg, H. Training induces changes in white-matter architecture. *Nat Neurosci 12*, 11 (2009), 1370–1371.

[129] Seunarine, K. K., and Alexander, D. C. *Multiple Fibers. Beyond the Diffusion Tensor.*, second ed. Elsevier, 2013.

[130] Shannon, C. E. A Mathematical Theory of Communication. *Bell System Technical Journal 5*, 3 (1948), 3.

[131] Shu, N., Liu, Y., Li, K., Duan, Y., Wang, J., Yu, C., Dong, H., Ye, J., and He, Y. Diffusion tensor tractography reveals disrupted topological efficiency in white matter structural networks in multiple sclerosis. *Cerebral Cortex 21*, 11 (2011), 2565–2577.

[132] Skare, S., Hedehus, M., Moseley, M. E., and Li, T. Q. Condition number as a measure of noise performance of diffusion tensor data acquisition schemes with MRI. *Journal of magnetic resonance 147*, 2 (2000), 340–52.

[133] Skudlarski, P., Jagannathan, K., Anderson, K., Stevens, M. C., Calhoun, V. D., Skudlarska, B. A., and Pearlson, G. Brain Connectivity Is Not Only Lower but Different in Schizophrenia: A Combined

Anatomical and Functional Approach. *Biological Psychiatry 68*, 1 (2010), 61–69.

[134] Smith, S. Introduction to the NeuroImage Special Issue "Mapping the Connectome". *NeuroImage 80*, Complete (2013).

[135] Smith, S. M., Jenkinson, M., Woolrich, M. W., Beckmann, C. F., Behrens, T. E. J., Johansen-Berg, H., Bannister, P. R., De Luca, M., Drobnjak, I., Flitney, D. E., Niazy, R. K., Saunders, J., Vickers, J., Zhang, Y., De Stefano, N., Brady, J. M., and Matthews, P. M. Advances in functional and structural MR image analysis and implementation as FSL. *NeuroImage 23*, SUPPL. 1 (2004), 208–219.

[136] Sotiropoulos, S. N., Jbabdi, S., Andersson, J. L., Woolrich, M. W., Ugurbil, K., and Behrens, T. E. J. RubiX: Combining spatial resolutions for bayesian inference of crossing fibers in diffusion MRI. *IEEE Transactions on Medical Imaging 32*, 6 (2013), 969–982.

[137] Sotiropoulos, S. N., Jbabdi, S., Xu, J., Andersson, J. L., Moeller, S., Auerbach, E. J., Glasser, M. F., Hernandez, M., Sapiro, G., Jenkinson, M., Feinberg, D. A., Yacoub, E., Lenglet, C., Van Essen, D. C., Ugurbil, K., and Behrens, T. E. J. Advances in diffusion MRI acquisition and processing in the Human Connectome Project. *NeuroImage 80* (2013), 125–143.

[138] Sporns, O. The human connectome: A complex network. *Annals of the New York Academy of Sciences 1224*, 1 (2011), 109–125.

[139] Sporns, O., Tononi, G., and Kötter, R. The human connectome: a structural description of the human brain. *PLoS computational biology 1*, 4 (2005), e42.

[140] Sporns, O., Tononi, G., and Kötter, R. The human connectome: A structural description of the human brain. *PLoS computational biology 1*, 4 (2005), e42.

[141] Stejskal, E. O., and Tanner, J. E. Spin diffusion measurements: spin echoes in the presence of a time-dependent field gradient. *The journal of chemical physics 42*, 1 (1965), 288–292.

[142] Thirion, B., Varoquaux, G., Dohmatob, E., and Poline, J.-B. Which fMRI clustering gives good brain parcellations? *Frontiers in neuroscience 8*, 167 (2014), 13.

[143] Thomas, C., Frank, Q. Y., Irfanoglu, M. O., Modi, P., Saleem, K. S., Leopold, D. A., and Pierpaoli, C. Anatomical accuracy of

brain connections derived from diffusion MRI tractography is inherently limited. *Proceedings of the National Academy of Sciences 111*, 46 (2014), 16574–16579.

[144] Tournier, J. D., Calamante, F., and Connelly, A. Robust determination of the fibre orientation distribution in diffusion MRI: Non-negativity constrained super-resolved spherical deconvolution. *NeuroImage 35*, 4 (2007), 1459–1472.

[145] Tournier, J. D., Calamante, F., and Connelly, A. MRtrix: Diffusion tractography in crossing fiber regions. *International Journal of Imaging Systems and Technology 22*, 1 (2012), 53–66.

[146] Tournier, J. D., Calamante, F., Gadian, D. G., and Connelly, A. Direct estimation of the fiber orientation density function from diffusion-weighted MRI data using spherical deconvolution. *NeuroImage 23*, 3 (2004), 1176–1185.

[147] Tuch, D. S. Q-ball imaging. *Magnetic Resonance in Medicine 52*, 6 (2004), 1358–1372.

[148] Tuch, D. S., Reese, T. G., Wiegell, M. R., Makris, N., Belliveau, J. W., and Van Wedeen, J. High angular resolution diffusion imaging reveals intravoxel white matter fiber heterogeneity. *Magnetic Resonance in Medicine 48*, 4 (2002), 577–582.

[149] Tuch, D. S., Reese, T. G., Wiegell, M. R., and Wedeen, V. J. Diffusion MRI of Complex Neural Architecture. *Neuron 40*, 5 (2003), 885–895.

[150] Tzourio-Mazoyer, N., Landeau, B., Papathanassiou, D., Crivello, F., Etard, O., Delcroix, N., Mazoyer, B., and Joliot, M. Automated anatomical labeling of activations in SPM using a macroscopic anatomical parcellation of the MNI MRI single-subject brain. *Neuroimage 15*, 1 (2002), 273–289.

[151] van den Heuvel, M. P., de Reus, M. A., Feldman Barrett, L., Scholtens, L. H., Coopmans, F. M. T., Schmidt, R., Preuss, T. M., Rilling, J. K., and Li, L. Comparison of diffusion tractography and tract-tracing measures of connectivity strength in rhesus macaque connectome. *Human Brain Mapping 36*, 8 (2015), 3064–3075.

[152] Van Essen, D. C., Jbabdi, S., Sotiropoulos, S. N., Chen, C., Dikranian, K., Coalson, T., Harwell, J., Behrens, T. E. J., and Glasser, M. F. *Mapping Connections in Humans and Non-Human Primates: Aspirations and Challenges for Diffusion Imaging*, second ed. No. January 2014. Elsevier, 2014.

[153] Van Essen, D. C., Smith, S. M., Barch, D. M., Behrens, T. E. J., Yacoub, E., and Ugurbil, K. The WU-Minn human connectome project: an overview. *Neuroimage 80* (2013), 62–79.

[154] Villalon-Reina, J. E., Nir, T. M., Zhan, L., Mcmahon, K. L., Zubicaray, G. I. D., Wright, M. J., Jahanshad, N., and Thompson, P. M. Reliability of Structural Connectivity Examined with Four Different Diffusion Reconstruction Methods at Two Different Spatial and Angular Resolutions. In *Computational Diffusion MRI and Brain Connectivity* (2014), pp. 219–231.

[155] Ward Jr, J. H. Hierarchical grouping to optimize an objective function. *Journal of the American statistical association 58*, 301 (1963), 236–244.

[156] Waxman, S., and Bennett, M. V. Relative conduction velocities of small myelinated and non-myelinated fibres in the central nervous system. *Nature 238*, 85 (1972), 217–219.

[157] Wedeen, V., Reese, T., Tuch, D., Weigel, M., Dou, J., Weiskoff, R., and Chessler, D. Mapping fiber orientation spectra in cerebral white matter with Fourier-transform diffusion MRI. *Proc. Intl. Sot. Mag. Reson. Med. 8 8* (2000), 5627–5627.

[158] Wen, W., Zhu, W., He, Y., Kochan, N. A., Reppermund, S., Slavin, M. J., Brodaty, H., Crawford, J., Xia, A., and Sachdev, P. Discrete Neuroanatomical Networks Are Associated with Specific Cognitive Abilities in Old Age. *Journal of Neuroscience 31*, 4 (2011), 1204–1212.

[159] Westbrook, C., and Roth, C. K. *MRI in Practice*. John Wiley & Sons, 2011.

[160] White, H. C., Boorman, S. A., and Breiger, R. L. Social structure from multiple networks. I. Blockmodels of roles and positions. *American journal of sociology* (1976), 730–780.

[161] Woolrich, M. W., Jbabdi, S., Patenaude, B., Chappell, M., Makni, S., Behrens, T., Beckmann, C., Jenkinson, M., and Smith, S. M. Bayesian analysis of neuroimaging data in FSL. *NeuroImage 45*, 1 (2009), S173–S186.

[162] Wu, D., and Zhang, J. In vivo mapping of macroscopic neuronal projections in the mouse hippocampus using high-resolution diffusion MRI. *NeuroImage 125* (2016), 84–93.

[163] Xu, Z., Tresp, V., Yu, K., and Kriegel, H. Infinite hidden relational models. *In Proceedings of the 22nd Inter- national Conference on Uncertainity in Artificial Intelligence* (2006).

[164] Yeh, F.-C., Vettel, J., Singh, A., Poczos, B., Grafton, S., Erickson, K., Tseng, W.-Y. I., and Verstynen, T. Quantifying Differences and Similarities in Whole-brain White Matter Architecture Using Local Connectome Fingerprints. *bioRxiv* (2016), 043778.

[165] Yoshiura, T., Wu, O., Zaheer, A., Reese, T. G., and Gregory Sorensen, A. Highly diffusion-sensitized MRI of brain: Dissociation of gray and white matter. *Magnetic Resonance in Medicine 45*, 5 (2001), 734–740.

[166] Ystad, M., Hodneland, E., Adolfsdottir, S., Haász, J., Lundervold, A. J., Eichele, T., and Lundervold, A. Cortico-striatal connectivity and cognition in normal aging: A combined DTI and resting state fMRI study. *NeuroImage 55*, 1 (2011), 24–31.

[167] Zalesky, A., Fornito, A., Cocchi, L., Gollo, L. L., van den Heuvel, M., and Breakspear, M. Connectome sensitivity or specificity: which is more important? *NeuroImage* (2016).

[168] Zalesky, A., Fornito, A., Harding, I. H., Cocchi, L., Yücel, M., Pantelis, C., and Bullmore, E. T. Whole-brain anatomical networks: does the choice of nodes matter? *Neuroimage 50*, 3 (2010), 970–983.

[169] Zalesky, A., Fornito, A., Seal, M. L., Cocchi, L., Westin, C. F., Bullmore, E. T., Egan, G. F., and Pantelis, C. Disrupted axonal fiber connectivity in schizophrenia. *Biological Psychiatry 69*, 1 (2011), 80–89.

[170] Zhan, L., Franc, D., Patel, V., Jahanshad, N., Jin, Y., Mueller, B., Bernstein, M., Borowski, B. J., Jack Jr, C. R., Toga, A. W., and Others. How do spatial and angular resolution affect brain connectivity maps from diffusion MRI? In *Biomedical Imaging (ISBI), 2012 9th IEEE International Symposium on* (2012), IEEE, pp. 1–4.

Part II

Manuscripts

Paper A

Ambrosen, K. S., Herlau, T., Dyrby, T. B., Schmidt, M. N., Mørup, M. (2013), 'Comparing Structural Brain Connectivity by the Infinite Relational Model', part of: Proceedings of the 3rd International Workshop on Pattern Recognition in Neuroimaging (PRNI 2013) (ISBN: 978-0-7695-5061-9), pages: 50-53, 2013, IEEE.

2013 3rd International Workshop on Pattern Recognition in Neuroimaging

Comparing Structural Brain Connectivity by the Infinite Relational Model

Karen S. Ambrosen*†, Tue Herlau*, Tim Dyrby†, Mikkel N. Schmidt* and Morten Mørup*

*Department of Applied Mathematics and Computer Science, Technical University of Denmark, Lyngby, Denmark
†Danish Research Centre for Magnetic Resonance, Copenhagen University Hospital Hvidovre, Hvidovre, Denmark
Email: kmsa@dtu.dk, tuhe@dtu.dk, timd@drcmr.dk, mnsc@dtu.dk, mmor@dtu.dk

***Abstract*—The growing focus in neuroimaging on analyzing brain connectivity calls for powerful and reliable statistical modeling tools. We examine the Infinite Relational Model (IRM) as a tool to identify and compare structure in brain connectivity graphs by contrasting its performance on graphs from the same subject versus graphs from different subjects. The inferred structure is most consistent between graphs from the same subject; however, the model is able to predict links in graphs from different subjects on par with results within a subject. The framework proposed can be used as a statistical modeling tool for the identification of structure and quantification of similarity in graphs of brain connectivity in general.**

***Keywords*-Neuroimaging, Bayesian Methods, Structural Connectivity, Relational Modelling**

I. Introduction

The human connectome [1], [2] constitutes a formidable network formed by trillions of connections between billions of neurons [1]. While current technologies cannot measure the full human connectome, functional and diffusion magnetic resonance imaging are key non-invasive techniques for measuring brain connectivity at a spatial resolution in the order of cubic-millimeters. Functional connectivity can be estimated by quantifying similarity between blood oxygen level dependent (BOLD) responses between brain regions [3], [4], whereas structural connectivity between gray-matter regions can be derived from tractography approaches, see also [5].

Using tools from network science, researchers have analyzed graphs of brain connectivity in terms of their functional segregation and integration as quantified by graph measures such as the clustering coefficient and shortest path properties, see also [4], [6]. In [7] structural connectivity graphs were derived between 998 regions of interests (ROI) spanning the whole brain for five subjects (one subject was scanned twice) using tractography based on diffusion spectrum imaging. These graphs were found to include a structural core as well as distinct structural modules [7].

With the growing focus in neuroimaging on modeling graphs of brain connectivity, there is a need for powerful and reliable statistical modeling tools that can identify latent structure. A further challenge is to compare different connectivity graphs, e.g. to assess similarities across different subjects, measuring modalities, etc. The Infinite Relational Model (IRM) [8]–[10] is a probabilistic generative model of structure in relational data (graphs), in which the nodes of the graph are partitioned into groups with statistically similar connectivity patterns. The number of groups is automatically inferred from data. The IRM can be used to quantify how similar two brain connectivity graphs are either by comparing the group structure estimated for two graphs or by fitting the model on one graph and using the result to predict the other graph, where a low prediction error indicates that the graphs are similar.

In this paper we discuss the following question: *Can the infinite relational model reliably be used to estimate latent group structure and quantify the similarity between brain connectivity graphs?* We address this by contrasting the performance of the IRM on graphs from the same subject versus graphs from different subjects, expecting that similarity should be greater on graphs from the same subject than on graphs from different subjects. As the inference in the IRM is based on Markov chain Monte Carlo (MCMC) we use multiple restarts to assess potential mixing issues of the sampler. To compare graphs we examine normalized mutual information as a measure of consistency of the inferred group structure and predictive log-likelihood and area under curve (AUC) of the receiver operator characteristic to estimate how well a model fitted on one graph can predict another graph. The proposed framework extends to the modeling of other types of brain networks and forms a principled statistical modeling tool for quantifying both the number of functional and structural units in brain networks as well as comparing brain connectivity in general.

II. Methods

The infinite relational model is a non-parametric Bayesian generative model for complex networks independently proposed in [8], [9]. The model is an extension of the stochastic block model [11] to include an unbounded number of clusters based on the Chinese Restaurant Process (CRP) (see also [12] for an introduction to the IRM.) The generative model for the IRM is given by

$$\begin{aligned} \boldsymbol{z} &\sim \mathrm{CRP}(\alpha), && \textit{Groups} \\ \eta_{lm} &\sim \mathrm{Beta}(\beta^+, \beta^-), && \textit{Interactions} \\ A_{ij} &\sim \mathrm{Bernoulli}(\eta_{z_i,z_j}), && \textit{Links}. \end{aligned}$$

978-0-7695-5061-9/13 $26.00 © 2013 IEEE
DOI 10.1109/PRNI.2013.22

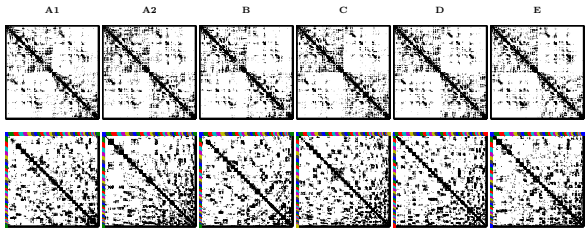

(a) Inferred structure

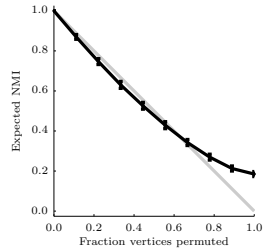

(b) Decrease in NMI

Figure 1: *Left:* Graphs before and after ordering into the maximum likelihood grouping. *Right:* NMI between grouping and itself after a fraction of vertices has been permuted. NMI roughly correspond to the fraction of permuted vertices.

The model partitions the nodes into groups $\boldsymbol{z}$ ($z_i = m$ means node i is assigned to group m). Links are formed between nodes in groups l and m independently with probability η_{lm}, and α, β^+, and β^- are hyperparameters of the model. As the beta prior on $\boldsymbol{\eta}$ is conjugate to the Bernoulli likelihood this parameter can be collapsed such that

$$p(\boldsymbol{A}, \boldsymbol{z}|\beta^+, \beta^-, \alpha) = \int d\boldsymbol{\eta}\ p(\boldsymbol{A}|\boldsymbol{z}, \boldsymbol{\eta}) p(\boldsymbol{z}, \boldsymbol{\eta}|\beta^+, \beta^-, \alpha)$$

$$= \left[\prod_{l \geq m} \frac{\mathrm{B}(n^+_{lm} + \beta^+, n^-_{lm} + \beta^-)}{\mathrm{B}(\beta^+, \beta^-)}\right] \left[\frac{\Gamma(\alpha)\alpha^K}{\Gamma(\alpha + I)} \prod_{k=1}^{K} \Gamma(n_k)\right],$$

where $\mathrm{B}(a, b) = \frac{\Gamma(a)\Gamma(b)}{\Gamma(a+b)}$ is the normalization constant of the beta distribution, n_m is the number of nodes in group m, and $n^+_{lm} = \sum_{ij} A_{ij}\delta_{l,z_i}\delta_{m,z_j}/2^{\delta_{lm}}$ (and similar for n^-_{lm} with A_{ij} replaced by $(1 - A_{ij})$) denotes the number of links and non-links between group l and m. We use the notation $\beta = \beta^+ + \beta^-$ and $n_{lm} = n^+_{lm} + n^-_{lm}$. Based on this, $\boldsymbol{z}$ can be inferred by MCMC. We use Gibbs sampling in combination with split-merge moves similar to [8].

A. Quantifying graph similarity by the IRM

To compare the similarity of graphs based on the IRM, the estimated group structure can be compared directly, or by exploiting that the IRM model is a generative model, a model fitted on one graph can be used to predict other graphs. We compare the following three measures to assess similarity between graphs: normalized mutual information (NMI) between the inferred clustering structure of the graphs, the predictive log-likelihood, and the area under curve (AUC) of the receiver operator characteristic. These three approaches are described below.

1) Normalized Mutual Information (NMI): The NMI between two group structures $\boldsymbol{z}$ and $\boldsymbol{z}^*$ is given by

$$\mathrm{NMI}(\boldsymbol{z}, \boldsymbol{z}^*) = \frac{2\mathrm{I}(\boldsymbol{z}, \boldsymbol{z}^*)}{\mathrm{I}(\boldsymbol{z}, \boldsymbol{z}) + \mathrm{I}(\boldsymbol{z}^*, \boldsymbol{z}^*)},$$

where $\mathrm{I}(\cdot, \cdot)$ is the mutual information defined by $\mathrm{I}(\boldsymbol{z}, \boldsymbol{z}^*) = \prod_{l,m} p(l, m) \log\left(\frac{p(l,m)}{p(l)p(m)}\right)$ and $p(l, m)$ is the probability that a node in cluster l in $\boldsymbol{z}$ is in cluster m in $\boldsymbol{z}^*$. For $\mathrm{I}(\boldsymbol{z}, \boldsymbol{z})$ this reduces to the entropy $H(\boldsymbol{z}) = -\sum_m p(m) \log p(m)$. An important property of mutual information is that it is invariant to permutation of the extracted groups. NMI is bounded by [0,1] where 0 indicates that the two group assignments are independent whereas 1 indicates the two groupings are identical up to permutation [13].

2) Predictive log-likelihood: To quantify how similar the structure of links are in two graphs we can evaluate how well the IRM inferred on graph $\boldsymbol{A}$ predicts the graph $\boldsymbol{A}^*$. The expected predictive log-likelihood for a given group structure $\boldsymbol{z}$ is given by

$$\langle \log p(\boldsymbol{A}^*|\boldsymbol{z}, \boldsymbol{A}, \beta^+, \beta^-, \alpha)\rangle_{p(\boldsymbol{\eta}|\boldsymbol{A},\boldsymbol{z})} =$$

$$\sum_{i>j} A^*_{ij} \langle \log \eta_{z_i,z_j}\rangle_{p(\boldsymbol{\eta}|\boldsymbol{A},\boldsymbol{z})} + (1 - A^*_{ij}) \langle \log(1 - \eta_{z_i,z_j})\rangle_{p(\boldsymbol{\eta}|\boldsymbol{A},\boldsymbol{z})}$$

where the expectations are $\langle \log(\eta_{z_i,z_j})\rangle = \psi(n^+_{lm} + \beta^+) - \psi(n_{lm} + \beta)$ and $\langle \log(1 - \eta_{z_i,z_j})\rangle = \psi(n^-_{lm} + \beta^-) - \psi(n_{lm} + \beta)$ and ψ is the digamma function $\psi(x) = \frac{d \log \Gamma(x)}{dx}$. Averaged over the posterior samples from the MCMC run, this can be used as a predictive similarity measure.

3) Area Under Curve (AUC): An alternative measure for prediction is based on the extend to which the probabilities of generating links inferred by the IRM in graph $\boldsymbol{A}$ can be used to separate the class of links and non-links in graph $\boldsymbol{A}^*$. The expected probability of generating a link between node i and j is given by

$$\langle p(A^*_{ij} = 1|\boldsymbol{z}, \boldsymbol{A}, \beta^+, \beta^-, \alpha)\rangle_{p(\boldsymbol{\eta}|\boldsymbol{A},\boldsymbol{z})} = \frac{n^+_{lm} + \beta^+}{n_{lm} + \beta}.$$

This probability can be used as a scoring function ($s(i, j)$) for computing the AUC which is bounded by [0,1] where 1 corresponds to a perfect separation of the link and non-links by the scoring function $s(i, j)$ whereas 0.5 means that the scoring function is no better than chance. A benefit of the AUC is that it is invariant to class-imbalance issues. The AUC is therefore widely used as measure of performance in link-prediction tasks, see also [14].

B. Data and experimental setup

The human cortex connectivity dataset [7] available from http://cmtk.org/viewer/datasets is used. The dataset consists

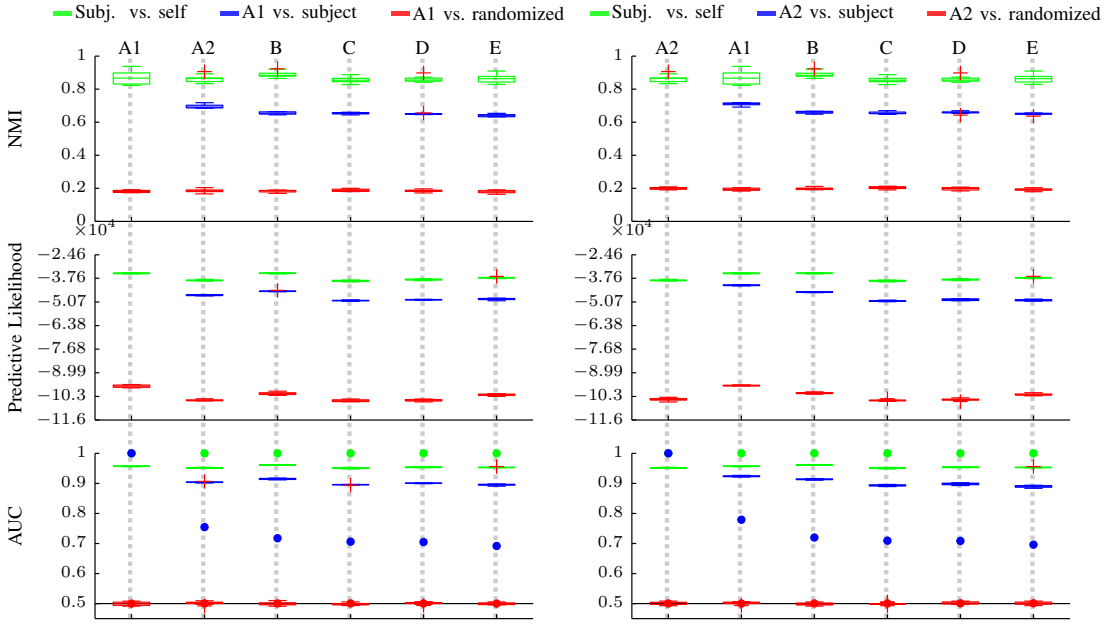

Figure 2: Each column indicates similarity between scan A1 (or A2) and the other scans according to NMI, predictive likelihood and AUC. The green boxes indicate variability across the 10 MCMC restarts, the blue boxes how well subject A1 (or A2) generalize across the other scans and the red is a baseline given by random permutations. The red crosses are outliers. The dots in the lower row correspond to naively predicting $\boldsymbol{A}^* = \boldsymbol{A}$.

of six structural connectivity graphs obtained from tractography based on diffusion spectrum imaging (DSI) from five subjects [7]. Graph A1 and A2 are obtained from two different scans of the same subject. The graphs have $J = 998$ nodes and were symmetrized and binarized before our analysis. The number of links and the graph densities are listed in Table I. The MCMC inference is initialized at random and is run for 50 000 iterations. Every 25th sample is saved, resulting in 2 000 samples. 10 MCMC restarts are made for each graph. The priors are selected as $\beta^+ = \beta^- = 1$ and $\alpha = \log(J)$. The number of clusters is initialized uniformly at random between 1 and 200.

Subject	No. of links	Graph density [%]
A1	27 040	2.71
A2	29 730	2.98
B	28 444	2.86
C	29 866	3.00
D	29 702	2.98
E	28 744	2.89

Table I: The number of links and density of the 6 graphs.

III. Results

The similarity of the groupings of nodes is found by calculating the NMI between the assignment matrices from MCMC restart 1 and 2, 2 and 3, ..., 10 and 1. The NMI for each subject versus itself is shown in Figure 2 as green boxes indicating an upper bound on the similarity. Instead of averaging NMI over the posterior distribution, we use the single posterior sample with the highest likelihood, thus the NMI for a graph versus itself should in theory be equal to one. The blue boxes are the NMI for MCMC restart 1 between subject A1 (A2 in second column) and all the other subjects—this indicates the estimated similarity between subjects. The red boxes show NMI between A1 (A2) and a random permutation of each subject indicating a lower bound on the similarity. The NMI within a subject is around 0.85 corresponding to a fraction of 10% of the nodes are permuted, as shown in Figure 1b. The reason why the NMI within a subject is less than 1 can be attributed to lack of mixing of the MCMC sampler making it unable to identify the same highest likelihood solution. This indicates that the MCMC sampler should either be run for a much larger number of iterations, which may be impractical, or that more efficient inference procedures should be devised. Nonetheless, the results gives an indication of the magnitude of error due to lack of mixing. The NMI between subject A1 and A2 is slightly higher than NMI between any other combinations. This indicates that the graph structure is more similar within a subject across scans than between subjects, but further investigations are needed to confirm the result.

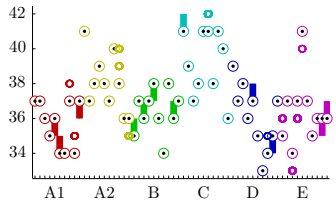

Figure 3: Boxplot of the number of groups in each of the 10 MCMC restarts per subject.

The NMI between subjects is well above random, suggesting a common latent structure between subjects.

The predictive log-likelihood and the AUC between subject A1 (A2 in second column) and the other subjects are found using every 25th sample of the last 25 000 samples using subject A1 (A2) as training data. The predictive log-likelihood and AUC is shown as blue boxes, the green boxes indicate how a subject predicts its own graph, and the red boxes show how A1 (A2) predicts the other graphs randomly permuted. For reference, the dots in the AUC plot indicate baseline results when naively predicting that graphs are equal. The predicted log-likelihood and AUC between subjects is well above random, again supporting a common latent structure; however, when training the model on subject A1 (left column), subject B has the highest predictive log-likelihood and AUC. This might be due to differences in graph density since A1 has the lowest graph density and graph B the second lowest density, but it also shows that predictive performance should be used with caution to assess graph similarity. When training the model on subject A2 (right column), subject A1 has the highest predictive log-likelihood and AUC: Here, as expected, the predictive performance is best within a subject.

Figure 3 shows a boxplot of the number of clusters in each MCMC restart where the color indicates the different subjects. Each box shows the distribution of the number of clusters from every 25th sample of the last 25 000 samples; however, most are centered on a single number again indicating that the MCMC sampler does not mix properly. Nevertheless, both within each subject and across subjects the number of components is fairly consistent.

IV. Conclusion

We proposed a framework for comparing graphs of brain connectivity based on the structure inferred by the infinite relational model. We tested the framework on six benchmark structural connectivity graphs derived from diffusion spectrum imaging and found that all the networks were consistent both within and between subjects. The inferred structure appeared to be slightly more consistent as quantified by NMI within a subject than from this subject to the other four subjects. However, it was observed that the inferred models predict structural connectivity equally well within a subject as across subjects. In particular, the structure inferred were significantly more consistent than would be expected by random and also more consistent than predicting on the raw graphs. We believe the proposed framework has promising applications for identifying structure and comparing brain connectivity data in general.

V. Acknowledgement

This work is funded by the Lundbeck Foundation.

References

[1] O. Sporns, G. Tononi, and R. Kötter, "The human connectome: a structural description of the human brain," *PLoS computational biology*, vol. 1, no. 4, p. e42, 2005.

[2] P. Hagmann, "From diffusion mri to brain connectomics," Ph.D. dissertation, 2005.

[3] E. Bullmore and O. Sporns, "Complex brain networks: graph theoretical analysis of structural and functional systems," *Nature Reviews Neuroscience*, vol. 10, no. 3, pp. 186–198, 2009.

[4] M. Rubinov and O. Sporns, "Complex network measures of brain connectivity: uses and interpretations," *Neuroimage*, vol. 52, no. 3, pp. 1059–1069, 2010.

[5] A. Daducci, S. Gerhard, A. Griffa, A. Lemkaddem, L. Cammoun, X. Gigandet, R. Meuli, P. Hagmann, and J.-P. Thiran, "The connectome mapper: An open-source processing pipeline to map connectomes with mri," *PLoS ONE*, vol. 7, 12 2012.

[6] D. S. Bassett and E. Bullmore, "Small-world brain networks," *The neuroscientist*, vol. 12, no. 6, pp. 512–523, 2006.

[7] P. Hagmann, L. Cammoun, X. Gigandet, R. Meuli, C. J. Honey, V. J. Wedeen, and O. Sporns, "Mapping the structural core of human cerebral cortex," *PLoS biology*, vol. 6, no. 7, p. e159, 2008.

[8] C. Kemp, J. B. Tenenbaum, T. L. Griffiths, T. Yamada, and N. Ueda, "Learning systems of concepts with an infinite relational model," in *Proceedings of the national conference on artificial intelligence*, vol. 21, no. 1. Menlo Park, CA; Cambridge, MA; London; AAAI Press; MIT Press; 1999, 2006, p. 381.

[9] Z. Xu, V. Tresp, K. Yu, and H.-P. Kriegel, "Learning infinite hidden relational models," in *Proceedings of the 22nd International Conference on Uncertainty in Artificial Intelligence*, 2006.

[10] K. W. Andersen, M. Morup, H. Siebner, K. H. Madsen, and L. K. Hansen, "Identifying modular relations in complex brain networks," in *Machine Learning for Signal Processing (MLSP), 2012 IEEE International Workshop on*. IEEE, 2012, pp. 1–6.

[11] K. Nowicki and T. A. B. Snijders, "Estimation and prediction for stochastic blockstructures," *Journal of the American Statistical Association*, vol. 96, no. 455, pp. 1077–1087, 2001.

[12] M. N. Schmidt and M. Mørup, "Non-parametric bayesian modeling of complex networks," *Signal Processing Magazine, IEEE*, vol. 30, no. 3, pp. 110–128, 2013.

[13] N. X. Vinh, J. Epps, and J. Bailey, "Information theoretic measures for clusterings comparison: Variants, properties, normalization and correction for chance," *The Journal of Machine Learning Research*, vol. 11, pp. 2837–2854, 2010.

[14] L. Lü and T. Zhou, "Link prediction in complex networks: A survey," *Physica A: Statistical Mechanics and its Applications*, vol. 390, no. 6, pp. 1150–1170, 2011.

Paper B

Ambrosen, K. S., Albers, K. J., Dyrby, T. B., Schmidt, M. N., Mørup, M. (2014), 'Nonparametric Bayesian Clustering of Structural Whole Brain Connectivity in Full Image Resolution', part of: Proceedings of the 4th International Workshop on Pattern Recognition in Neuroimaging (PRNI 2014) (ISBN: 978-1-4799-4149-0), 2014, IEEE.

Nonparametric Bayesian Clustering of Structural Whole Brain Connectivity in Full Image Resolution

Karen Sandø Ambrosen*†, Kristoffer Jon Albers*, Tim B. Dyrby†, Mikkel N. Schmidt*, and Morten Mørup*
*Department of Applied Mathematics and Computer Science, Technical University of Denmark, Lyngby, Denmark
†Danish Research Centre for Magnetic Resonance, Copenhagen University Hospital Hvidovre, Hvidovre, Denmark

***Abstract*—Diffusion magnetic resonance imaging enables measuring the structural connectivity of the human brain at a high spatial resolution. Local noisy connectivity estimates can be derived using tractography approaches and statistical models are necessary to quantify the brain's salient structural organization. However, statistically modeling these massive structural connectivity datasets is a computational challenging task. We develop a high-performance inference procedure for the infinite relational model (a prominent non-parametric Bayesian model for clustering networks into structurally similar groups) that defines structural units at the resolution of statistical support. We apply the model to a network of structural brain connectivity in full image resolution with more than one hundred thousand regions (voxels in the gray-white matter boundary) and around one hundred million connections. The derived clustering identifies in the order of one thousand salient structural units and we find that the identified units provide better predictive performance than predicting using the full graph or two commonly used atlases. Extracting structural units of brain connectivity at the full image resolution can aid in understanding the underlying connectivity patterns, and the proposed method for large scale data driven generation of structural units provides a promising framework that can exploit the increasing spatial resolution of neuro-imaging technologies.**

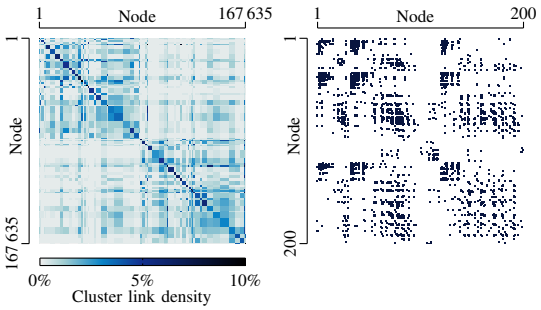

Fig. 1. Complex network of structural brain connectivity with 167 635 nodes and around one hundred million links obtained using 5000 streamlines per seed voxel. Left: Link density in each pair of the 68 regions of interest in the Desikan-Killiany atlas. Right: Links between the first 200 regions.

I. Introduction

Diffusion magnetic resonance imaging (dMRI) is an important non-invasive technique for studying the brain's structural organization. By tracking the diffusion of mainly water molecules that align with the orientation of the fibers in the brain, local estimates of fiber orientation can be obtained. These estimates are aggregated by tractography to derive maps of structural connectivity between cortical gray matter regions [5]. For the current dMRI technology these maps in full image resolution constitute complex networks of structural connectivity in the order of one hundred thousand regions and one hundred million links (see Fig. 1).

While the quantified fiber orientation within small regions of the brain as well as the subsequently derived local connectivity estimates are very noisy, these estimates can be aggregated to derive networks of whole brain connectivity within larger regions of structural units. These structural units have traditionally been based on automatic subdivision of the human brain into a fixed number of pre-specified neuroanatomical regions of interests (ROIs) [13], [7]. The Destrieux atlas [13], [8] currently has around 150 ROIs whereas the Desikan-Killiany atlas [7] has 68 ROIs. While these ROIs can be arbitrarily subdivided to provide additional regions [14] they are not explicitly based on the evidence obtained by the structural connectivity data and may therefore not optimally reflect the latent connectivity patterns of structural connectivity. Rather than fixing the structural units to a predefined atlas, we set out to learn the number of structural units and their spatial representations from the raw high resolution networks obtained using tractography. To accomplish this we develop a large scale implementation of a prominent statistical network model, the infinite relational model (IRM) [17], [24]. The IRM is able to infer structurally consistent units at a resolution which is determined based on statistical evidence. While structural connectivity graphs have previously been clustered based on IRM [3] as well as other tools such as modularity [14], this is to the best of our knowledge the first attempt at modelling structural connectivity at the full image resolution of current dMRI technology.

This paper examines the capabilities of a large scale implementation of the IRM to identify structure in high-resolution structural brain connectivity graphs. We study to what extend we can perform inference on such large scale networks and whether it is feasible to reliably detect the structural units in a data driven manner using our implementation. In particular, we investigate: i) *What is the statistically salient resolution of structural connectivity graphs*, i.e., how many clusters are used to represent high resolution structural connectivity data? ii) *How reliable can these salient structures be detected*, i.e. how consistent are the structural units with respect to initialization and convergence of the sampler as well as the number of streamlines? iii) *Are the derived structural units better at predicting connectivity than existing atlases*, i.e. how well does the connectivity patterns derived from the structural units of one graph predict the connectivity of another graph obtained from another set of whole brain diffusion weighted images from the same subject?

978-1-4799-4149-0/14/$31.00

II. Statistical model and inference

A. Infinite Relational Modelling

The Infinite Relational Model (IRM) [17], [24] is a non-parametric extension of the stochastic block model [19] in which vertices in a graph are grouped into homogenous blocks according to their structural similarity. The IRM uses the Chinese Restaurant Process (CRP) [2], [20] as prior for the partitioning of vertices to groups thereby allowing for an arbitrary number of groups. The IRM is defined by the following generative process:

$$\boldsymbol{z} \sim \mathrm{CRP}(\alpha), \qquad \text{groups}, \tag{1}$$

$$\eta_{lm} \sim \mathrm{Beta}(\beta^+, \beta^-), \qquad \text{interactions}, \tag{2}$$

$$A_{ij} \sim \mathrm{Bernoulli}(\eta_{z_i z_j}), \qquad \text{links}, \tag{3}$$

where $\boldsymbol{z}$ is the group assignment, $\boldsymbol{\eta}$ is the probability of links between each pair of groups, and $\boldsymbol{A}$ is the adjacency matrix of the graph. As the beta prior on the elements of $\boldsymbol{\eta}$ is conjugate to the Bernoulli likelihood these parameters can be analytically integrated to form the joint distribution:

$$P(\boldsymbol{A}, \boldsymbol{z}|\alpha, \beta^+, \beta^-) = \int P(\boldsymbol{A}, \boldsymbol{z}, \boldsymbol{\eta}|\alpha, \beta^+, \beta^-) d\boldsymbol{\eta} \tag{4}$$

$$= \frac{\alpha^K \Gamma(\alpha) \prod_k \Gamma(n_k)}{\Gamma(J+\alpha)} \prod_{l \leq m} \frac{\mathrm{B}(N_{lm}^+ + \beta^+, N_{lm}^- + \beta^-)}{\mathrm{B}(\beta^+, \beta^-)},$$

where K is the number of groups, J is the number of vertices, n_k is the number of vertices assigned to the k'th group, N_{lm}^+ and N_{lm}^- are the number of links and non-links between group l and m, and $B(a,b) = \frac{\Gamma(a)\Gamma(b)}{\Gamma(a+b)}$ is the beta function.

B. Inference by Markov Chain Monte Carlo (MCMC)

To infer the posterior distribution, $P(\boldsymbol{z}|\boldsymbol{A}, \alpha, \beta^+, \beta^-)$, we use an MCMC procedure combining Gibbs and split-merge sampling [17]. In Gibbs sampling the posterior conditional distribution of placing one vertex at a time in any of the existing groups or in a new empty group is evaluated and the vertex is assigned according to this distribution. The probability of assigning a vertex i to group ℓ is given by:

$$P(z_i = \ell | \boldsymbol{A}, \boldsymbol{z}_{\setminus i}, h) = \frac{P(\boldsymbol{A}, \boldsymbol{z}_{\setminus i}, z_i = \ell | h)}{\sum_{\ell'=1}^{K+1} P(\boldsymbol{A}, \boldsymbol{z}_{\setminus i}, z_i = \ell' | h)}, \tag{5}$$

where $h = \{\beta^+, \beta^-, \alpha\}$ denotes the hyperparameters.

Rather than considering the assignment of a single vertex at a time split-merge sampling as presented in [15] attempts to merge or split existing clusters. Here, two vertices i and j are selected at random. If they are currently assigned to two different groups $z_i \neq z_j$, it is proposed to merge the two groups. Else it is proposed to split the single group in two. The procedure makes use of Gibbs sampling restricted to the nodes of the considered group(s) in order to define an intermediate launch state as well as to define the final split configuration and its transition probability $q(z|z^*)$. For a split configuration $q(z|z^*)$ is derived as the product of the individual transition probabilities of the vertices to move from the launch state to the final split configuration. As a merge transition is deterministic the transition from a split to a merge configuration has probability 1. Proposals are rejected or accepted according to the Metropolis-Hastings acceptance probability:

$$\alpha(z^*|z) = \min\left[1, \frac{P(\boldsymbol{A}, \boldsymbol{z}^*|\beta^+, \beta^-, \alpha) q(z|z^*)}{P(\boldsymbol{A}, \boldsymbol{z}|\beta^+, \beta^-, \alpha) q(z^*|z)}\right]. \tag{6}$$

C. Large scale computation

To get the computational performance necessary for the IRM to model structural connectivity in full image resolution we used a dedicated implementation optimized towards fully utilizing the memory structure and processor architecture of modern computers (see [1] for details). As the restricted Gibbs sweeps turns out to be the most computational demanding part of the split-merge sampling procedure, the performance of both sampling strategies benefits from most of the same optimizations. We store data in appropriate structures such that the sampling algorithms access data elements from sequential memory. In this way the access pattern takes advantage of the memory cache structure allowing for significantly faster memory accesses. To further speed up the Gibbs sampler we store and update the sufficient statistics, N^+ and N^-, instead of recalculating them in every Gibbs sweep. To ensure numeric stability within machine precision, the posterior in Eq. 5 is calculated in the log domain. The key operation then becomes calculating the logarithm of the beta function which relies on the gamma-function, $\Gamma(a)$, as:

$$\log B(a,b) = \log\Gamma(a) + \log\Gamma(b) - \log\Gamma(a+b) \tag{7}$$

As we only allow integer values for the hyperparameters, we use a lookup table of precalculated values for $\log\Gamma(a)$ which speeds up the evaluation of the posterior.

III. Data

To validate our proposed method, we used a dMRI data set previously described in [23], [22]. The data was collected at Danish Research Center for Magnetic Resonance and the study was approved by the local ethics committee. One healthy subject was scanned. The images were acquired on a Siemens VERIO 3T scanner using a 32-channel head coil. Two high resolution T1-weighted MRI images were acquired using a TR of 1,900 ms, TE of 2.32 ms, a FA of 9°, and 0.9mm^3 isotropic resolution. Two sets of whole brain diffusion weighted images (DWI) were acquired in 61 non-collinear directions with a b-value of b = 1500 s/mm^2, and ten non-diffusion weighted images (b = 0 s/mm^2). For this the twice refocused spin echo sequence with a TR of 11,440 ms and a TE of 89 ms. 61 axial slices with a resolution of 2.3 mm^3 isotropic voxels and Grappa = 2 were acquired [21]. A field map was acquired using a double gradient echo sequence with a TR of 479 ms, TE1 of 4.92 ms, TE2 of 7.38 ms, and a resolution of 3mm^3 isotropic voxels. The diffusion weighted images (DWI) were pre-processed using SPM8 (www.fil.ion.ucl.ac.uk/spm). To reduce motion artifacts and eddy current induced distortions an affine transformation between the DWIs based on normalized mutual information was applied. The voxel displacement map (VDM) was calculated based on the field map resliced to DWI resolution using the field map toolbox of SPM8 [16]. The VDM was applied to minimize geometric distortions due to susceptibility artifacts. Finally the DWIs were aligned and resliced with affine matrix to a T1 weighted MRI using 7th degree B-spline interpolation [10]. The 61 non-collinear diffusion weighting gradient directions were updated using the same rotations and transformations as the resliced

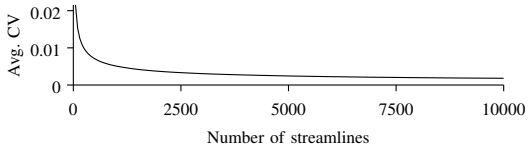

Fig. 2. Average voxel-wise coefficient of variation (CV) as function of number of streamlines in the tractography. The CV and the SNR are based on tractography results repeated five times for each number of streamlines.

images [18]. Segmentation of the white and gray matter was performed based on the high resolution structural T1w images using Freesurfer (surfer.nmr.mgh.harvard.edu) [6], [12], [11]. The Freesurfer reconstruction outputs, among others, the white matter segmentation and the gray-white matter boundary. The gray-white matter boundary for both hemispheres was converted to volumes and transformed from Freesurfer conformed space to native space. Likewise, the white matter segmentation from the Freesurfer reconstruction was transformed to native space. The diffusion parameters were estimated using FSL's BedpostX and probabilistic tractography was performed using FSL's Probtrackx2 with the omatrix3 option [4]. The transformed white matter volume was used as seed in the tractography and the transformed cortex labels as both target and stop mask in the tractography. For all other options the default settings were used. The cortex to cortex connectivity graph were output from FSL's probtrackx2 using the omatrix3 option. We obtained four 167,635×167,635 connectivity graphs (i.e., scan and rescan for 1000 and 5000 streamlines per seed voxel). Each link in the graphs took on the value of the number of streamlines connecting the two voxels in the target mask (gray/white matter boundary). The graphs were symmetrized and binarized (i.e., for each graph the graph and its transpose were added together and entries that were subsequently above zero set to one).

IV. Experiments and Results

A. Number of streamlines

To ensure that the network obtained by tractography is robust, probabilistic tractography was performed with different number of streamlines: Between 50 and 10,000 streamlines per seed voxel were used. Each number of streamlines was run five times. The voxel-wise coefficient of variation (CV) between voxels within the seed mask in the images with equal number of streamlines was calculated as $\mathrm{CV} = \frac{\sigma}{\mu}$, where σ is the standard deviation and μ is the mean. The average CV across all voxels was calculated [9] and is shown as function of number of streamlines in Fig. 2. The number of streamlines used in the subsequent experiments was selected on the basis of the average CV: As the average CV seems to have reached a stable level when using 1000 streamlines, and definitely when using 5000 streamlines (Fig. 2) we compare these two values.

B. Model parameters, inference, and convergence

For each network we performed 10 separate runs, all with the hyper parameters $\beta^+ = \beta^- = 1$ and $\alpha = \lfloor \log(J) \rfloor$, where J is the total number of nodes. For each run, we performed 100 iterations of the following sampling procedure: Each iteration began with a complete Gibbs sweep over all nodes. It was then followed by the same number of split-merge operations as the current number of clusters. In each split-merge operation we performed 10 restricted Gibbs sweeps. Each of these iterations took several hours to compute. Fig. 3 shows the logarithm of the joint distribution for the different runs. It is clear that the MCMC sampler does not converge (which was also not to be expected [1]), but even when the sampler does not converge, the inferred grouping captures suboptimal but relevant structures in the network. In the following we used the inferred group structure after the last MCMC iteration.

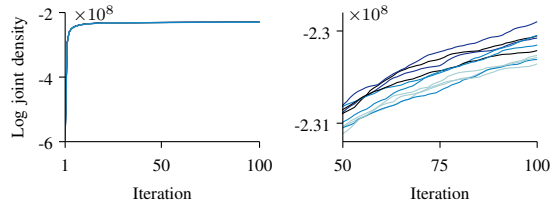

Fig. 3. Logarithm of the joint distribution for the MCMC inference procedure for the network based on 5000 streamlines. A zoom of the last 50 iterations is shown to the right.

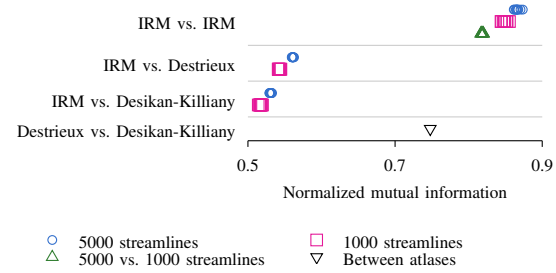

Fig. 4. Normalized Mutual Information (NMI) between 10 independent runs of the IRM and two atlases for network based on 1000 and 5000 streamlines.

C. Comparison and stability of estimated group structure

To compare the unsupervised groupings found by IRM with the groupings provided by the two atlases, we use the normalized mutual information (NMI) as a measure of similarity between 0 and 1. For two groupings $\boldsymbol{z}$ and $\boldsymbol{z}'$, we use: $\mathrm{NMI}(\boldsymbol{z}, \boldsymbol{z}') = \frac{2 \cdot \mathrm{I}(\boldsymbol{z}, \boldsymbol{z}')}{\mathrm{H}(\boldsymbol{z}) + \mathrm{H}(\boldsymbol{z}')}$ where $\mathrm{I}(\boldsymbol{z}, \boldsymbol{z}')$ is the mutual information between the groupings and $\mathrm{H}(\boldsymbol{z})$ is the entropy of $\boldsymbol{z}$. Fig. 4 shows NMI between all runs as well as between the runs and the two atlases. It is evident that the inferred groupings are very similar in the 10 runs as evidenced by the relatively high NMI, both within and between the networks based on 1000 and 5000 streamlines, respectively. Also, the inferred grouping is somewhat similar to the two atlases with an NMI score around 0.5-0.6.

D. Predictive performance

To assess how well the inferred structure fits the data, we use a second structural connectivity network based on a rescan of the same subject. Since any differences between the two scans are due to noise in the processes of generating the network, measuring how well we can predict the links in the second graph can be used to quantify the utility of the inferred structural units. To measure the predictive performance we use the area under the receiver operating characteristic curve (AUC) which allows us to compare predictions from the IRM

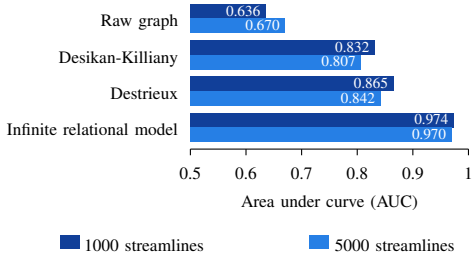

Fig. 5. Performance as measured by the area under the receiver operating characteristic curve (AUC) when predicting links in a network of structural connectivity based on data from a second scan of the same subject.

model with predictions made using other existing atlases or predicting directly from the raw network data. The results in Fig. 5 show that the IRM model outperforms predictions from the raw graph as well as both the Desikan-Killiany and Destrieux atlases both for networks based on 1000 and 5000 streamlines. However, when inspecting the extracted structural units (not shown) they were more diffuse compared to the atlases which may hamper their interpretation. This may be attributed both to the lack of convergence as well as lack of spatial constraints in the modeling.

V. Conclusion

When analyzing whole brain structural connectivity in full image resolution in the order of one thousand salient structural units were identified by our large scale implementation of the infinite relational model. The network based on 5000 streamlines had more structural units compared to the network based on 1000 streamlines. However, the estimated group structures were quite similar as quantified by NMI. Although the MCMC sampler did not reach convergence the identified groups were fairly robust to initialization while having some similarity to the Destrieux and Desikan-Killiany atlases. Notably, the extracted structural units provided significantly better predictive performances than predicting using the structural connectivity graph itself or the two considered atlases.

The present paper is to the best of our knowledge the first attempt at clustering structural connectivity in full resolution and provides a promising tool for a more detailed account of structural connectivity in general. In future work the influence of image resolution and choice of hyper-parameters should be investigated as should better sampling strategies.

Acknowledgment

This project was funded by the Lundbeck Foundation. We thank Andreas Leon Aagaard Moth for help with the large scale implementation.

References

[1] Kristoffer Jon Albers, Andreas Leon Aagard Moth, Morten Mørup, and Mikkel N. Schmidt. Large scale inference in the infinite relational model: Gibbs sampling is not enough. In *Machine Learning for Signal Processing (MLSP), 2013 IEEE International Workshop on*, pages 1–6. IEEE, 2013.

[2] D. Aldous. Exchangeability and related topics. *École d'Été de Probabilités de Saint-Flour XIII1983*, pages 1–198, 1985.

[3] Karen S Ambrosen, Tue Herlau, Tim Dyrby, Mikkel N Schmidt, and Morten Mørup. Comparing structural brain connectivity by the infinite relational model. In *Pattern Recognition in Neuroimaging (PRNI), 2013 International Workshop on*, pages 50–53. IEEE, 2013.

[4] TEJ Behrens, H Johansen Berg, Saad Jbabdi, MFS Rushworth, and MW Woolrich. Probabilistic diffusion tractography with multiple fibre orientations: What can we gain? *Neuroimage*, 34(1):144–155, 2007.

[5] TEJ Behrens, MW Woolrich, M Jenkinson, H Johansen-Berg, RG Nunes, S Clare, PM Matthews, JM Brady, and SM Smith. Characterization and propagation of uncertainty in diffusion-weighted mr imaging. *Magnetic resonance in medicine*, 50(5):1077–1088, 2003.

[6] Anders M Dale, Bruce Fischl, and Martin I Sereno. Cortical surface-based analysis: I. segmentation and surface reconstruction. *Neuroimage*, 9(2):179–194, 1999.

[7] Rahul S Desikan, Florent Ségonne, Bruce Fischl, Brian T Quinn, Bradford C Dickerson, Deborah Blacker, Randy L Buckner, Anders M Dale, R Paul Maguire, Bradley T Hyman, et al. An automated labeling system for subdividing the human cerebral cortex on mri scans into gyral based regions of interest. *Neuroimage*, 31(3):968–980, 2006.

[8] Christophe Destrieux, Bruce Fischl, Anders Dale, and Eric Halgren. Automatic parcellation of human cortical gyri and sulci using standard anatomical nomenclature. *Neuroimage*, 53(1):1–15, 2010.

[9] Annette J Dobson. *An introduction to generalized linear models*. CRC press, 2001.

[10] TB Dyrby, HM Lundell, MG Liptrot, MW Burke, M Ptito, and HR Siebner. Interpolation of dwi prior to dti reconstruction, and its validation. In *Proc. Intl. Soc. Mag. Reson. Med*, volume 19, 2011.

[11] Bruce Fischl, David H Salat, Evelina Busa, Marilyn Albert, Megan Dieterich, Christian Haselgrove, Andre van der Kouwe, Ron Killiany, David Kennedy, Shuna Klaveness, et al. Whole brain segmentation: automated labeling of neuroanatomical structures in the human brain. *Neuron*, 33(3):341–355, 2002.

[12] Bruce Fischl, Martin I Sereno, and Anders M Dale. Cortical surface-based analysis: Ii: Inflation, flattening, and a surface-based coordinate system. *Neuroimage*, 9(2):195–207, 1999.

[13] Bruce Fischl, André van der Kouwe, Christophe Destrieux, Eric Halgren, Florent Ségonne, David H Salat, Evelina Busa, Larry J Seidman, Jill Goldstein, David Kennedy, et al. Automatically parcellating the human cerebral cortex. *Cerebral cortex*, 14(1):11–22, 2004.

[14] Patric Hagmann, Leila Cammoun, Xavier Gigandet, Reto Meuli, Christopher J Honey, Van J Wedeen, and Olaf Sporns. Mapping the structural core of human cerebral cortex. *PLoS biology*, 6(7):e159, 2008.

[15] S. Jain and Radford M Neal. A split-merge markov chain monte carlo procedure for the dirichlet process mixture model. *Journal of Computational and Graphical Statistics*, 13(1), 2004.

[16] Peter Jezzard and Robert S Balaban. Correction for geometric distortion in echo planar images from b0 field variations. *Magnetic resonance in medicine*, 34(1):65–73, 1995.

[17] C. Kemp, J. B. Tenenbaum, T. L. Griffiths, T. Yamada, and N. Ueda. Learning systems of concepts with an infinite relational model. In *AAAI*, volume 3, page 5, 2006.

[18] Alexander Leemans and Derek K Jones. The b-matrix must be rotated when correcting for subject motion in dti data. *Magnetic Resonance in Medicine*, 61(6):1336–1349, 2009.

[19] Krzysztof Nowicki and Tom A B Snijders. Estimation and prediction for stochastic blockstructures. *Journal of the American Statistical Association*, 96(455):1077–1087, 2001.

[20] J. Pitman et al. Combinatorial stochastic processes. Technical report, Springer, 2002.

[21] TG Reese, O Heid, RM Weisskoff, and VJ Wedeen. Reduction of eddy-current-induced distortion in diffusion mri using a twice-refocused spin echo. *Magnetic Resonance in Medicine*, 49(1):177–182, 2003.

[22] Nina Linde Reislev, Ron Kupers, Hartwig R. Siebner, Maurice Ptito, and Tim B. Dyrby. Blindness differentially affects the integrity of the dorsal and ventral visual streams, 2013.

[23] Nina Linde Reislev, Maurice Ptito, Ron Kupers, Hartwig R. Siebner, and Tim B Dyrby. Alterations of the inferior longitudinal fasciculus in congenital and late blindness, 2012.

[24] Z. Xu, V. Tresp, K. Yu, and H.P. Kriegel. Learning infinite hidden relational models. *Uncertainty in Artificial Intelligence (UAI2006)*, 2006.

Paper C

Ambrosen, K. S.*, Albers, K. J.*, Liptrot, M. G., Dyrby, T. B., Schmidt, M. N., Mørup, M. (2016), 'Predictive Validation of Human Brain Parcellations', *in preparation*

** These authors contributed equally to the manuscript.*

Predictive Validation of Human Brain Parcellations

Karen S. Ambrosen[a,b,1,2], **Kristoffer J. Albers**[a,1], **Matthew G. Liptrot**[a], **Tim B. Dyrby**[a,b], **Mikkel N. Schmidt**[a], **and Morten Mørup**[a]

[a]Department of Applied Mathematics and Computer Science, Technical University of Denmark, Richard Petersens Plads, Building 324, DK-2800 Kgs. Lyngby, Denmark; [b]Danish Research Centre for Magnetic Resonance, Centre for Functional and Diagnostic Imaging and Research, Copenhagen University Hospital Hvidovre, Kettegaard Allé 30, DK-2650 Hvidovre, Denmark

The organization of the human brain remains elusive, yet is known to be of great importance to the mechanisms of integrative brain function. At the macroscale, its structural and functional interpretation is conventionally assessed at the level of cortical units, permitting inference across a population. However, the definition and validation of such a cortical parcellation is problematic due to the absence of a true gold standard. We propose a framework for quantitative validation of brain parcellations via statistical prediction on independent brain connectivity data. Using this framework we assess the pertinence of three existing parcellations to account for structural connectivity (SC) data, and compare them to random parcellations and data-driven parcellations optimized for SC. We find that all three atlases perform better than random, and the multi-modal atlas recently proposed by Glasser et al. provides superior characterisation of SC compared with those based solely upon surface morphology. Our analysis further suggests that the SC data is better characterized using more parcels than contained in the considered atlases.

Brain parcellation | Diffusion magnetic resonance imaging (dMRI) | whole brain structural connectivity | human connectome | link prediction

The vast complexity of the human brain [1, 2] and the incomplete and noisy measurements available through neuroimaging modalities require a pragmatic approach to the analysis of the human connectome [3, 4]. Segregation into anatomical or functional units provides interpretable and noise reduced network nodes whose inter-connections approximate the brain's organizational structure [5, 6]. Much research is underway to delineate the structural and functional organization of the human brain [7, 8] but it remains unclear which parcellation best accounts for such organization and how this is quantified.

To provide a sound basis for analysis, the nodes provided by a given parcellation method must be robust across a population, and fully represent their local infrastructure, microscopical properties and connectional "fingerprint" — their unique pattern of inputs and outputs [9]. For example, when defining cortical regions at the macroscale it has been suggested that specific functions of the areas, such as connectivity, reproducibility, convergence, multimodality, evolutionary coherence, and inter-subject variability, should all be taken into account [10]. However, there still remains a lack of gold standard evaluation strategies against which any particular parcellation can be tested.

The exact method of parcellation employed depends upon the application. Hence a wide variety of parcellation schemes are currently available, including cortical surface morphology (Desikan-Killiany [11], Destrieux [12]), functional activation (AAL [13, 14]), structural connectivity (SC) [15–17], and combinations thereof (Brainnetome [18], HCP_MMP1.0 [19]).

The various parcellation schemes exhibit considerable differences, e.g. number of parcels and parcel border locations, and no single parcellation appears to be universally accepted. The situation is exacerbated by studies showing that subsequent graph measures are sensitive to the chosen parcellation scheme, both for structural [20] and functional [21, 22] analyses.

The differences in both the size, extent and downstream effects of a parcellation illustrate that it is important to validate its relevance to the application in question. Whilst reliability is often purported as a proxy for validation, it is not sufficient because a method can be arbitrarily reliable yet poorly account for brain organization. In contrast, the use of data on brain organization that is independent of how a parcellation is derived can permit a true validation of a parcellation. To achieve this, we herein describe how parcellations can be validated using statistical prediction based upon independent brain connectivity data.

Our statistical prediction framework poses quantification of parcellation quality as a link-prediction problem [15, 23–25]. A parcellation is thereby assessed by its ability to characterize brain connectivity data from an independent modality. In particular, the approach quantifies how well network structure is preserved in the independent modality by the network organization induced by the parcellation. Herein, we have used independent high-resolution SC data from the Human Connectome Project (HCP) [26–30] to validate three atlases: Desikan-Killiany (68 parcels) [11], Destrieux (148 parcels) [12] and Human Connectome Project multi-modality parcellation

Significance Statement

Analysis of brain connectivity is commonly based on a parcellation defined from an anatomical atlas; however, there is no consensus as to what constitutes a good parcellation for characterising brain connectivity, and a well-founded strategy that can quantify the quality of such parcellations is lacking. Here we demonstrate how parcellations can be validated using statistical prediction on independent connectivity data. Our predictive validation framework confirms that three prominent atlases capture the complexity of structural connectivity (SC) much better than random. In particular, a recent atlas combining multiple modalities and using substantially more parcels displays superior performance over those based solely on surface morphology. Finally, using data-driven parcellations optimized for SC we find support for more parcels than currently used.

The authors declare no conflict of interest.

[1]Karen S. Ambrosen and Kristoffer J. Albers contributed equally to this work.

[2]To whom correspondence should be addressed. E-mail: kmsa@dtu.dk

(HCP_MMP1.0, 360 parcels) [19]. Whereas the first two are based upon surface morphology, the latter is a multi-modality atlas which includes fMRI (both resting-state and task-based), cortical thickness and myelin mapping. We contrast the predictive performance of these atlases to SC-informed parcellations as well as to spatial homogeneous random parcellations.

Using this validation framework we find that all three atlases perform far better than random parcellations. We further find that the HCP_MMP1.0 atlas better accounts for SC data than the atlases derived from surface morphology. Furthermore, the framework permits estimation of the number of parcels supported by the data and we find that the SC data supports more parcels than employed in existing atlases.

1. Results

Figure 1 outlines the proposed predictive procedure. Input to the procedure is a parcellation $\boldsymbol{z}$ ($z_i = m$ indicates that node i belongs to parcel number m) and the SC networks of the training and test population considered. The average density ρ_{lm} of links for the training graphs is computed between each pair of parcels ($l \neq m$) and within each parcel ($l = m$), thereby representing the SC data in terms of the aggregated average connectivities between parcels. These average connectivites are then used to predict the SC of the test graphs, by predicting a link between node i and j by the score $s_{ij} = \rho_{z_i z_j}$ for all $i > j$. As measure of performance, the area under curve (AUC) of the receiver operator characteristic (range $[0, 1]$) is used. The AUC is 1 if links and non-links in the test graph are perfectly separated according to the scores s_{ij}, whereas a random prediction would give an AUC of 0.5 (for further details see supporting information (SI)).

We validate the three non-SC based parcellation schemes of Desikan-Killiany [11], Destrieux [32], and HCP_MMP1.0 [19].

To provide values of reference for the scale of the AUC scores, we estimate upper and lower bounds on the predictive performance: Upper bounds were estimated using data-driven SC parcellations, based on the stochastic block model (SBM) [15, 25, 33–36] and Ward clustering [37] as proposed in [17, 38, 39]. These methods cluster nodes into homogeneous parcels according to their structural similarity and are derived to optimally account for the SC profile of the whole brain. They thereby provide an estimate of the upper bound for the predictive performance that can be obtained on SC data using a parcellation. To provide an estimate of the lower bound of predictive performance, we generated a parcellation based on k-means clustering [40] that grouped nodes based solely upon their Cartesian coordinates thereby forming spatially homogeneous random parcels uninformed by anatomy and SC. Finally, to ascertain that no substantial information about SC is lost by representing SC data in terms of parcels, we contrast the performance of parcellations to conventional non-parametric link-prediction methods [23]. Background information on all the above methods is provided in SI.

SC graphs ($n = 59,412$ vertices) covering the cerebral cortex of both hemispheres were generated for 26 subjects using data from the Human Connectome Project (HCP) [26–30]. The graphs were constructed using ProbtrackX2 based probabilistic tractography from FSL [41–43] with 1000 streamlines seeded from each white-matter voxel [15]. Each subject's SC graph was binarised by thresholding at a connectivity strength of 200 streamlines (see SI regarding the choice of threshold level).

The predictive framework was applied independently on: three single subjects, three populations of five subjects, two populations of ten subjects, and one population of 20 subjects. For all analyses the same six subjects were held-out for prediction.

Validation of three existing atlases. Figure 2, left panel, shows the impact of the amount of training data on the attainable upper and lower bounds. The figure shows the AUC curves for all the parcellations as more training subjects are included (different line styles). The results for single subjects show large uncertainty and predictive performance substantially below population based prediction (SBM: AUC=0.9486 (22), Ward: AUC=0.9615 (19)), and hence training with a single subject is insufficient to characterize SC. However, already with five training subjects there is a large reduction in variability and increase in AUC (SBM: AUC=0.9790 (1), Ward: AUC=0.9799 (1)), and the inclusion of 10 (SBM: AUC=0.9831 (2), Ward: AUC=0.9833 (2)) and 20 subjects (SBM: AUC=0.9857, Ward: AUC=0.9857) only adds minor improvements. Furthermore, for five or more training subjects, the ranking of the atlases predictive performance remains constant, see Figure S7 in SI. Consequently, even a limited sample of 20 training subjects provides sufficient robustness for predictive accuracy.

Using 20 subjects as our training population, the predictive assessment of the different parcellation schemes is investigated in Figure 2, right panel. The predictive performance of the three tested atlases are represented by the red symbols and the corresponding performance of the random (k-means) parcellation and data driven parcellations given by the blue, yellow and green curves respectively. For the performance at the same number of parcels as the three tested atlases we find for 68 parcels (Desikan-Killiany: AUC=0.9535, k-means: AUC=0.8886, Ward: AUC=0.9654, SBM: AUC=0.9701), for 148 parcels (Destrieux: AUC=0.9687, k-means: AUC=0.9153, Ward: AUC=0.9777, SBM: AUC=0.9787), and for 360 parcels (HCP_MMP1.0: AUC=0.9807, k-means: AUC=0.9339, Ward: AUC=0.9836, SBM: AUC=0.9841). The vertical gap between the atlases and the random parcellations demonstrates that all three atlases perform far better than what would be expected by random if their parcels did not comply with the SC data. When considering the differences in predictive performance to the data-driven SC parcellations we find that both Desikan-Killiany (downward-pointing triangle) and Destrieux (upward-pointing triangle) have suboptimal performance. However, the HCP_MMP1.0 atlas (diamond) is not only superior to the surface morphology-based atlases but also almost on par with the best of the data-driven parcellations optimized to account for SC. We find these results to be robust to the applied threshold level and size of training population (considering at least five subjects for training), see SI (Figure S7).

To estimate the parcellation resolution supported by the SC data, we determined the beginning of the plateau regions (green and yellow stars), above which the predictive performance does not improve significantly (assessed using a paired t-test). These points can be interpreted as the minimum number of clusters required to sufficiently describe the SC data. The two data-driven models, SBM [15, 25, 33–36] (green curves) and Ward clustering [37] (yellow curves), show the same optimal predictive performance (AUC=0.9857). As they

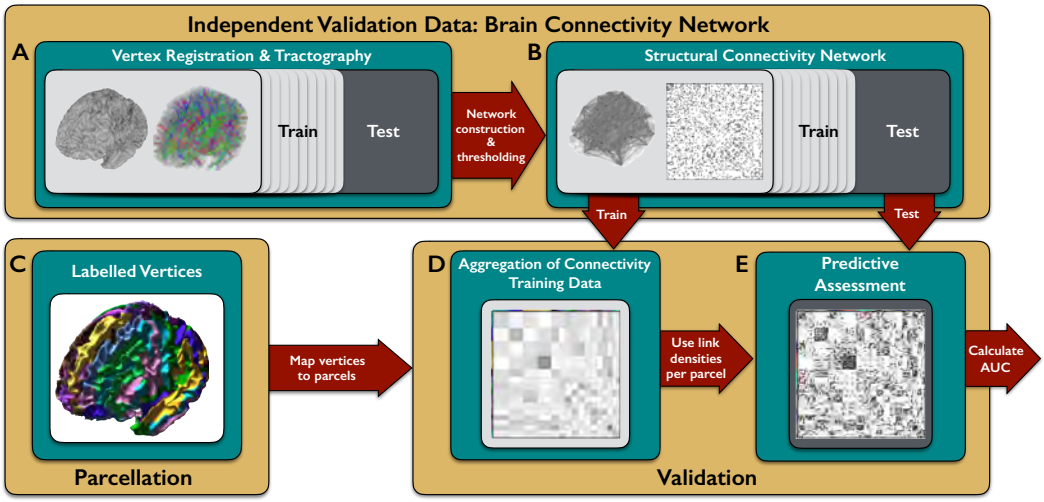

Fig. 1. The predictive validation framework using SC data. A) The native surfaces of all subjects are co-registered to a standard vertex mesh to obtain one-to-one correspondance between the surface vertices of every subject [31]. Tractography is performed between all vertices of the surface by initialising 1000 streamlines in all white-matter voxels resulting in a weighted symmetric SC network for each subject. B) The networks are thresholded to obtain binary links of SC (connections in left panel, dots in right panel). C) The considered parcellation. D) The training networks are permuted according to the parcellation π in question and the link densities ρ_{lm} between and within parcels calculated by aggregating all the training networks. E) The predictive performance is assessed by calculating the area under the curve (AUC) of the receiver operator characteristics using the scores obtained from the training link-densities (grey background) to predict the links of the test network (overlaid dots).

are based on different modeling approaches (SBM: Bayesian model with MCMC inference, Ward: deterministic agglomerative hierarchical clustering) this implies that the estimated upper bound is robust. In addition, both models approach the AUC of the best non-parametric link-predictor (shortest path, AUC=0.9875), shown as a black horizontal line, suggesting that no important information regarding the structural organization is lost when employing data-driven parcellations.

To investigate the effect of increasing the number of parcels to the maximum possible, we considered the limit where each node is given its own (singleton) cluster. This gave a much lower predictive performance (AUC=0.9336) than all considered atlases and SC parcellations.

Additional scores for single subjects and populations of 5 and 10 as well as scores obtained using standard non-parametric link-prediction methods [23] are given in Table 1 and in SI (Table S1).

Visualization of the parcellation structure. Figure 3 compares the parcellations from the three tested atlases together with the best performing SC parcellations using a population of 20 training subjects, both at the matching number of parcels and the SBM parcellation with 700 parcels, beyond which no significant improvement is found. Note how the parcellations found by SBM are spatially homogeneous even though the considered SBM does not incorporate any knowledge of spatial location. Additional parcellations are visualised in SI, Figures S2-S4. The data-driven parcellations comply better with the existing atlases than the random parcellations (SI, Figure S8).

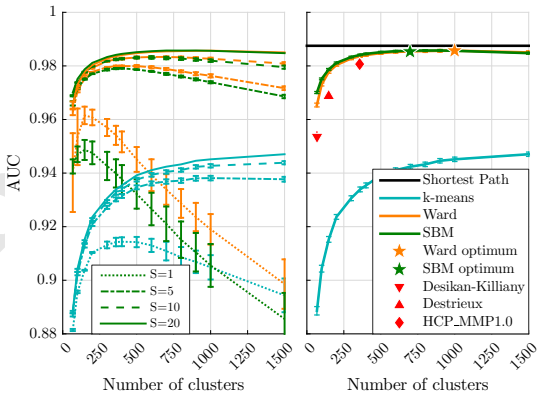

Fig. 2. Predictive performance measured by average AUC. Left panel: Predictive performance of the two data-driven SC parcellations as well as the random k-means parcellation (different colors), when using 1, 5, 10, and 20 subjects in the training set (different line styles). The error bars show the standard deviation of the mean across the training graphs. Right panel: Predictive performance using 20 training subjects of the three considered atlases: Desikan-Killiany (downward-pointing triangle), Destrieux (upward-pointing triangle), and HCP_MMP1.0 (diamond), as well as k-means random parcellations (blue) and data-driven SC parcellations Ward (yellow) and SBM (green). The stars indicate the optimal number of clusters, above which no significant increase in performance is observed for the two data-driven SC parcellations, based on a paired t-test. The predictive performance of shortest path is shown as a black horizontal line. The error bars show the standard deviation of the mean across the six test subjects.

2. Discussion

We here present a validation framework that permits quantitative assessment of any given parcellation scheme in the absence of a gold standard reference (ground truth parcellation). The

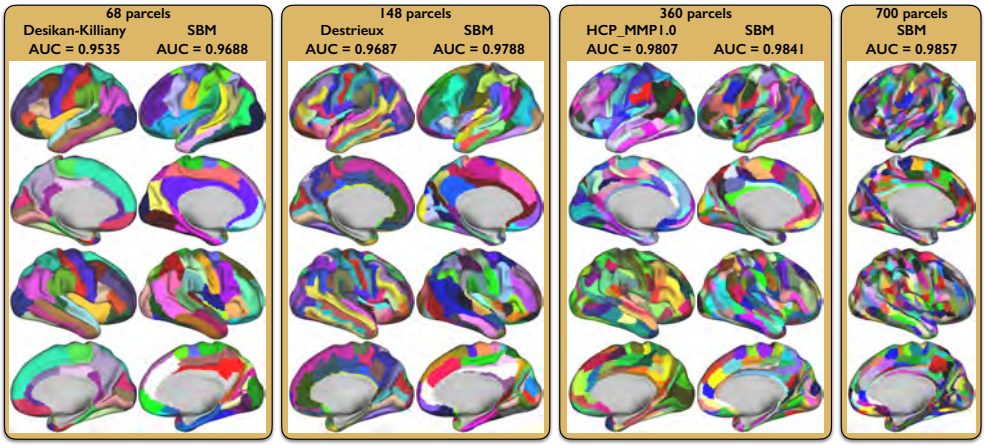

Fig. 3. Parcellations from the (left to right) Desikan-Killiany atlas and SBM with 68 parcels, the Destrieux atlas and SBM with 148 parcels, HCP_MMP1.0 and SBM with 360 parcels, and SBM with 800 parcels (green star in Figure 2 (right panel)), all visualised on the inflated surface. SBM was trained on 20 subjects. The AUC score is the average score across the six test subjects for the specific parcellation shown. The standard deviation of the mean is below 0.002 for all shown parcellations.

Table 1. Average AUC across six test subjects and five restarts when predicting unseen connectivity graphs using data-driven parcellations including the singleton parcellation in which each node is given its own cluster, as well as the best performing non-parametric link predictor (shortest path) and the three considered atlases. The scores are given for the optimal number of parcels (SI, Figure S7). For k-means clustering, the single subject score is given for 360 parcels, while remaining scores are given for 1000 parcels. In parentheses is given the standard deviation of the mean on last digit across different training networks.

	Population size			
	Single (n=3)	5 (n=3)	10 (n=2)	20 (n=1)
UPPER BOUND ESTIMATES				
Shortest path	0.9453 (25)	0.9830 (3)	0.9862 (2)	0.9875
SBM	0.9486 (22)	0.9790 (1)	0.9831 (2)	0.9857
Ward clustering	0.9615 (19)	0.9799 (1)	0.9833 (2)	0.9857
BRAIN ATLASES				
HCP_MMP1.0	0.9595 (9)	0.9777 (1)	0.9796 (5)	0.9807
Destrieux	0.9599 (9)	0.9670 (2)	0.9681 (9)	0.9687
Desikan-Killiany	0.9479 (7)	0.9524 (6)	0.9530 (14)	0.9535
LOWER BOUND ESTIMATES				
k-means	0.9143 (9)	0.9381 (5)	0.9427 (4)	0.9451
Singleton	0.7027 (120)	0.8541 (27)	0.9016 (1)	0.9336

framework uses statistical prediction to validate a parcellation by its ability to characterize the structure of independent brain connectivity data. Using this framework we validated three existing parcellations (not based on SC data) in their ability to characterize the organization of SC data.

Our framework, in being able to rank the performance of the prospective parcellations, shows that all three evaluated atlases are able to capture many of the features of SC and much better than would be expected by random. The framework further permits quantification of the improvement in predictive performance achieved by a recent multi-modality approach by Glasser et al. [19] over those based solely upon surface morphology. In particular, we find that the multi-modality approach has performance almost on par with data-driven SC parcellations that are tailored to account for the organization of SC. These results are robust to the level of threshold of streamlines applied to generate the SC networks and consistent for the population based analyses, i.e. when at least five subjects are used in the training population.

As the three tested atlases perform far better than the lower-bound provided by the k-means random parcellations this implies that the organization of SC is in compliance with the atlases. The difference in predictive performance between the atlases and the estimated upper-bound for prediction given by the data-driven parcellations can be interpreted as the predictive loss due to the mismatch between SC and atlas parcel boundaries. As the two surface morphology-based atlases are unable to match the performance of the data-driven methods this implies reduced co-dependence between SC and surface morphology. However, the HCP_MMP1.0 atlas, being almost on par with the data-driven parcellations, emphasizes the utility of having multiple modalities.

Number of subjects. An important question answered by our framework is determining the number of subjects necessary to characterize SC data. Although it is recommended to use as many training subjects as possible, our validation framework demonstrates that even with limited data (20 training subjects) the predictive performance is sufficient to evaluate parcellations and the ranking of the atlases remains constant for five or more subjects. Furthermore, the poor performance of data-driven SC parcellations when trained on a single subject emphasizes the importance of inference at the population level in order to well account for the organization of SC.

Parcellations preserve SC information. The best performing standard link prediction measure, shortest path, provides an estimate of the predictive performance that can be obtained taking all the SC information into account rather than resorting to aggregated information at the level of parcels when predicting. The minor difference between the performance of

shortest path and the data-driven parcellations implies that the latter are able to maintain the prominent information regarding the connectivity structure present in the data. We thereby find that the SC data is well represented using structural units defined by parcels supporting analysis of SC at the level of much coarser structural units.

Number of parcels supported by SC data. In this work, we determined the optimum number of parcels supported by SC by locating the point beyond which no significant increase occurred in the data-driven SC parcellations. We here found that the data-driven parcellations in general supports more parcels than provided by the recently proposed HCP_MMP1.0 atlas. Glasser et al. accordingly state that their parcellation may still underestimate the true number of parcels at the macroscale, as their sub-divisioning of areas such as the primary visual cortex are coarser than reported previously [19]. However, care must be taken when interpreting the estimated numbers of clusters supported by the SC data as we find that it is dependent upon the number of subjects included in the training data as well as the graph threshold level. Furthermore, an exact estimate of the optimal number of clusters is non-trivial due to the broad range of resolutions that produce similar predictive performance. The optimum may also be influenced by biases in the SC data as discussed below that can potentially lead to overestimating of the number of structural units. However, as the results for the k-means parcellations show, simply using a high number of clusters is not sufficient to capture the complexity of the SC data. Furthermore, we observed that the AUC did not continue to increase with more clusters: In particular, the extreme case where all the clustering models coincide (singleton clustering) exhibited poor predictive performance (AUC=0.9336 for 20 subjects). Even so, we observed that the performance of the singleton parcellations substantially improved when including more subjects in the training set, and we anticipate that with unlimited training data the averaging across training subjects may reduce the noise of the data to such an extent that the observed performance drop of singleton clusters may disappear. Thus, although our results point to the need for substantially more parcels than available in the considered atlases, these results may be heavily influenced by the level of noise and the biases, as discussed below.

Biases in the surface registration between subjects. A possible limitation to the results reported herein is the accuracy of the initial vertex-to-vertex registration framework, as provided by the HCP pipeline [31]. As this is driven by surface topology [44], there exists the possibility that the subsequent vertex alignment is biased towards anatomical landmarks (and therefore provide atlases based upon surface morphology with an inherent prediction boost). As anatomy may not be an optimal predictor of SC, this means that the assumed vertex-to-vertex correspondence may not fully reflect the nature of the SC data. Hence, such a bias would exhibit itself as noise in the vertex labeling, which would in turn propagate to the adjacency matrix (graph). As a consequence, it would be more difficult for a data-driven model to produce large homogeneous clusters of vertices which all possess similar patterns of SC. This would make larger clusters less likely, and so our predictive framework could therefore support an over-parcellation. Advanced vertex registration procedures, such as that employed in [19], may improve matters as the imposed predictive bias will be balanced between multiple modalities.

Tractography biases. SC is established from dMRI data by integrating the derived local estimates of fibre bundle orientations obtained with standard tractography methods [45]. However, just as for all other methods that estimate connectivity, tractography has its own challenges and limitations, e.g. gyral crown bias [46–48], which could affect the precise location of parcel borders, path length dependencies [49] and other factors which together are known to impose unknown levels of Type I and Type II errors on the estimated connections [50–53]. These confounds, biases and shortcomings of tractography are as yet not fully quantifiable due to the lack of a gold-standard reference [54], and indeed are not detectable as they will be present in both training and test datasets. Yet, despite all the challenges in tractography, we find that the existing atlases in general comply well with the SC data and that the best performing atlas is almost on par with the data-driven parcellations tailored for SC. This indeed points to compliance of the organization of SC with other modalities.

Other biases. No matter which connectivity modality is employed within our prediction framework, the inclusion of more training subjects, whilst increasing the signal-to-noise ratio, will not be able to compensate for modality-specific biases present in both training and test populations. However, the framework introduced herein can easily be extended to include multi-modality data such as fMRI, tracer studies, or histological reconstruction of axonal trajectories [10]. As demonstrated by Glasser et al. [19], the incorporation of many independent data-sources can mollify the effects of their individual biases. Indeed, sufficiently many sources may even render the manually-intensive verification of individual parcels unnecessary.

Thresholding of SC networks. As with any graph model of connectivity, false positives and false negatives will occur as the incorrect presence or absence of links. Herein, as is common practice [20, 55, 56], we attempt to remove many of the false positive connections by thresholding the SC graphs prior to modeling. However, this uniformly-applied strategy also increases the false negative rate. Unfortunately, whilst the false positive rate can be reduced to zero by increasing the threshold, the minimum false negative rate, achieved at null thresholding, will be non-zero and can only be improved by better data acquisition and processing strategies. As such, it must be noted that the chosen threshold level determines the balance between a model's specificity and sensitivity, and no optimal threshold exists [54, 57–59]. Even though the applied threshold of 200 streamline counts seems reasonable for this data set, as different initialisations of the tractography are able to predict each other very well (see Figure S1), the threshold is still arbitrarily chosen. However, as discussed earlier, the ranking of the considered atlases is maintained across all tested thresholds, demonstrating robustness of the proposed predictive validation procedure to the chosen threshold level.

Outlook. Our predictive validation procedure shows that the recently proposed HCP_MMP1.0 atlas provides a reasonable model of SC parcellation, and should be preferred to those based solely upon surface morphology. We validated parcellations using independent SC data, but the proposed validation

framework is generic and therefore applicable to any other brain connectivity mapping approach. As the number of data-sources and data-derived approaches to structural and functional connectivity, and thereby also parcellation schemes, will only increase in the future, we foresee that the prediction framework presented herein will prove to be an important tool in assessing their quality.

Materials and Methods

The data used in the preparation of this work were obtained from the MGH-USC Human Connectome Project (HCP) database (https://ida.loni.usc.edu/login.jsp). For additional descriptions of the materials and methods used in this study, see SI.

ACKNOWLEDGMENTS. This project was supported by the Lundbeck Foundation, grant no. R105-9813.
Data were provided by the Human Connectome Project, WU-Minn Consortium (Principal Investigators: David Van Essen and Kamil Ugurbil; 1U54MH091657) funded by the 16 NIH Institutes and Centers that support the NIH Blueprint for Neuroscience Research; and by the McDonnell Center for Systems Neuroscience at Washington University.

References.

1. Braitenberg V, Schüz A (1991) *Anatomy of the cortex: Statistics and geometry.* (Springer-Verlag Publishing).
2. Murre J, Sturdy D (1995) The connectivity of the brain: multi-level quantitative analysis. *Biological cybernetics* 73(6):529–545.
3. Sporns O, Tononi G, Kötter R (2005) The human connectome: a structural description of the human brain. *PLoS computational biology* 1(4):e42.
4. Hagmann P (2005) From diffusion mri to brain connectomics [phd thesis]. *Lausanne: Ecole Polytechnique Fédérale de Lausanne (EPFL)*. 127 p.
5. Bullmore E, Sporns O (2009) Complex brain networks: graph theoretical analysis of structural and functional systems. *Nature Reviews Neuroscience* 10(3):186–198.
6. Sporns O (2012) *Discovering the human connectome.* (MIT press).
7. Smith S (2013) Introduction to the neuroimage special issue "mapping the connectome". *NeuroImage* 80(Complete).
8. Van Essen DC et al. (2013) The wu-minn human connectome project: an overview. *Neuroimage* 80:62–79.
9. Passingham RE, Stephan KE, Kötter R (2002) The anatomical basis of functional localization in the cortex. *Nature Reviews Neuroscience* 3(8):606–616.
10. Amunts K, Zilles K (2015) Architectonic mapping of the human brain beyond brodmann. *Neuron* 88(6):1086–1107.
11. Desikan RS et al. (2006) An automated labeling system for subdividing the human cerebral cortex on mri scans into gyral based regions of interest. *Neuroimage* 31(3):968–980.
12. Fischl B et al. (2004) Automatically parcellating the human cerebral cortex. *Cerebral cortex* 14(1):11–22.
13. Tzourio-Mazoyer N et al. (2002) Automated anatomical labeling of activations in spm using a macroscopic anatomical parcellation of the mni mri single-subject brain. *Neuroimage* 15(1):273–289.
14. Gong G et al. (2009) Mapping anatomical connectivity patterns of human cerebral cortex using in vivo diffusion tensor imaging tractography. *Cerebral cortex* 19(3):524–536.
15. Ambrosen KS, Albers KJ, Dyrby TB, Schmidt MN, Morup M (2014) Nonparametric bayesian clustering of structural whole brain connectivity in full image resolution in *Pattern Recognition in Neuroimaging, 2014 International Workshop on.* (IEEE), pp. 1–4.
16. Parisot S, Arslan S, Passerat-Palmbach J, Wells WM, Rueckert D (2016) Group-wise parcellation of the cortex through multi-scale spectral clustering. *NeuroImage*.
17. Baldassano C, Beck DM, Fei-Fei L (2015) Parcellating connectivity in spatial maps. *PeerJ* 3:e784.
18. Fan L et al. (2016) The human brainnetome atlas: A new brain atlas based on connectional architecture. *Cerebral Cortex* p. bhw157.
19. Glasser MF et al. (2016) A multi-modal parcellation of human cerebral cortex. *Nature* 536(7615):171–178.
20. Hagmann P et al. (2008) Mapping the structural core of human cerebral cortex. *PLoS biology* 6(7):e159.
21. Zalesky A et al. (2010) Whole-brain anatomical networks: does the choice of nodes matter? *Neuroimage* 50(3):970–983.
22. Fornito A, Zalesky A, Bullmore ET (2010) Network scaling effects in graph analytic studies of human resting-state fmri data. *Frontiers in systems neuroscience* 4.
23. Liben-Nowell D, Kleinberg J (2007) The link-prediction problem for social networks. *Journal of the American society for information science and technology* 58(7):1019–1031.
24. Clauset A, Moore C, Newman ME (2008) Hierarchical structure and the prediction of missing links in networks. *Nature* 453(7191):98–101.
25. Andersen KW et al. (2014) Non-parametric bayesian graph models reveal community structure in resting state fmri. *NeuroImage* 100:301–315.
26. Van Essen DC et al. (2012) The human connectome project: a data acquisition perspective. *Neuroimage* 62(4):2222–2231.
27. Moeller S et al. (2010) Multiband multislice ge-epi at 7 tesla, with 16-fold acceleration using partial parallel imaging with application to high spatial and temporal whole-brain fmri. *Magnetic Resonance in Medicine* 63(5):1144–1153.
28. Feinberg DA et al. (2010) Multiplexed echo planar imaging for sub-second whole brain fmri and fast diffusion imaging. *PloS one* 5(12):e15710.
29. Setsompop K et al. (2012) Blipped-controlled aliasing in parallel imaging for simultaneous multislice echo planar imaging with reduced g-factor penalty. *Magnetic Resonance in Medicine* 67(5):1210–1224.
30. Xu J et al. (2012) Highly accelerated whole brain imaging using aligned-blipped-controlled-aliasing multiband epi in *Proceedings of the 20th Annual Meeting of ISMRM.* Vol. 2306.
31. Glasser MF et al. (2013) The minimal preprocessing pipelines for the human connectome project. *Neuroimage* 80:105–124.
32. Destrieux C, Fischl B, Dale A, Halgren E (2010) Automatic parcellation of human cortical gyri and sulci using standard anatomical nomenclature. *Neuroimage* 53(1):1–15.
33. White HC, Boorman SA, Breiger RL (1976) Social structure from multiple networks. i. blockmodels of roles and positions. *American journal of sociology* pp. 730–780.
34. Holland PW, Laskey KB, Leinhardt S (1983) Stochastic blockmodels: First steps. *Social networks* 5(2):109–137.
35. Nowicki K, Snijders TAB (2001) Estimation and prediction for stochastic blockstructures. *Journal of the American Statistical Association* 96(455):1077–1087.
36. Schmidt MN, Morup M (2013) Nonparametric bayesian modeling of complex networks: An introduction. *Signal Processing Magazine, IEEE* 30(3):110–128.
37. Ward Jr JH (1963) Hierarchical grouping to optimize an objective function. *Journal of the American statistical association* 58(301):236–244.
38. Eickhoff SB et al. (2011) Co-activation patterns distinguish cortical modules, their connectivity and functional differentiation. *Neuroimage* 57(3):938–949.
39. Thirion B, Varoquaux G, Dohmatob E, Poline JB (2014) Which fmri clustering gives good brain parcellations? *Frontiers in neuroscience* 8(167):13.
40. MacQueen J, et al. (1967) Some methods for classification and analysis of multivariate observations in *Proceedings of the fifth Berkeley symposium on mathematical statistics and probability.* (Oakland, CA, USA.), Vol. 1, pp. 281–297.
41. Jenkinson M, Beckmann CF, Behrens TE, Woolrich MW, Smith SM (2012) Fsl. *Neuroimage* 62(2):782–790.
42. Behrens T et al. (2003) Characterization and propagation of uncertainty in diffusion-weighted mr imaging. *Magnetic resonance in medicine* 50(5):1077–1088.
43. Behrens T, Berg HJ, Jbabdi S, Rushworth M, Woolrich M (2007) Probabilistic diffusion tractography with multiple fibre orientations: What can we gain? *Neuroimage* 34(1):144–155.
44. Fischl B (2012) Freesurfer. *Neuroimage* 62(2):774–781.
45. Behrens T et al. (2003) Non-invasive mapping of connections between human thalamus and cortex using diffusion imaging. *Nature neuroscience* 6(7):750–757.
46. Van Essen DC et al. (2013) Mapping connections in humans and nonhuman primates: aspirations and challenges for diffusion imaging. *Diffusion MRI, 2nd edition (eds. Johansen-Berg, H. & Behrens, TEJ)* pp. 337–358.
47. Reveley C et al. (2015) Superficial white matter fiber systems impede detection of long-range cortical connections in diffusion mr tractography. *Proceedings of the National Academy of Sciences* 112(21):E2820–E2828.
48. Donahue CJ et al. (2016) Using diffusion tractography to predict cortical connection strength and distance: a quantitative comparison with tracers in the monkey. *The Journal of Neuroscience* 36(25):6758–6770.
49. Liptrot MG, Sidaros K, Dyrby TB (2014) Addressing the path-length-dependency confound in white matter tract segmentation. *PloS one* 9(5):e96247.
50. Jones DK (2010) Challenges and limitations of quantifying brain connectivity in vivo with diffusion mri. *Imaging in Medicine* 2(3):341–355.
51. Morris DM, Embleton KV, Parker GJ (2008) Probabilistic fibre tracking: differentiation of connections from chance events. *Neuroimage* 42(4):1329–1339.
52. Le Bihan D, Poupon C, Amadon A, Lethimonnier F (2006) Artifacts and pitfalls in diffusion mri. *Journal of magnetic resonance imaging* 24(3):478–488.
53. Jones DK, Knösche TR, Turner R (2013) White matter integrity, fiber count, and other fallacies: the do's and don'ts of diffusion mri. *Neuroimage* 73:239–254.
54. Knösche TR, Anwander A, Liptrot M, Dyrby TB (2015) Validation of tractography: comparison with manganese tracing. *Human brain mapping* 36(10):4116–4134.
55. Drakesmith M et al. (2015) Overcoming the effects of false positives and threshold bias in graph theoretical analyses of neuroimaging data. *NeuroImage* 118:313–333.
56. Hagmann P et al. (2007) Mapping human whole-brain structural networks with diffusion mri. *PloS one* 2(7):e597.
57. Zalesky A et al. (2016) Connectome sensitivity or specificity: which is more important? *NeuroImage*.
58. Qi S, Meesters S, Nicolay K, ter Haar Romeny BM, Ossenblok P (2015) The influence of construction methodology on structural brain network measures: a review. *Journal of neuroscience methods* 253:170–182.
59. Dyrby TB et al. (2007) Validation of in vitro probabilistic tractography. *Neuroimage* 37(4):1267–1277.
60. Sotiropoulos S et al. (2013) Effects of image reconstruction on fiber orientation mapping from multichannel diffusion mri: reducing the noise floor using sense. *Magnetic resonance in medicine* 70(6):1682–1689.
61. Milchenko M, Marcus D (2013) Obscuring surface anatomy in volumetric imaging data. *Neuroinformatics* 11(1):65–75.
62. Hernández M et al. (2013) Accelerating fibre orientation estimation from diffusion weighted magnetic resonance imaging using gpus. *PLoS One* 8(4):e61892.
63. Miller K, Jordan MI, Griffiths TL (2009) Nonparametric latent feature models for link prediction in *Advances in neural information processing systems.* pp. 1276–1284.

Supporting Information (SI).

Diffusion imaging, tractography and construction of connectivity graphs.

MRI acquisition The MRI data used in the preparation of this work were obtained from the MGH-USC Human Connectome Project (HCP) database (https://ida.loni.usc.edu/login.jsp) in the "500 subjects" release. The HCP project (Principal Investigators: Bruce Rosen, M.D., Ph.D., Martinos Center at Massachusetts General Hospital; Arthur W. Toga, Ph.D., University of California, Los Angeles, Van J. Weeden, MD, Martinos Center at Massachusetts General Hospital) is supported by the National Institute of Dental and Craniofacial Research (NIDCR), the National Institute of Mental Health (NIMH) and the National Institute of Neurological Disorders and Stroke (NINDS). Collectively, the HCP is the result of efforts of co-investigators from the University of California, Los Angeles, Martinos Center for Biomedical Imaging at Massachusetts General Hospital (MGH), Washington University, and the University of Minnesota.

Acquisition parameters are described in full for dMRI in [27–30, 60], and for the structural scans in [61], and are listed in brief here. The dMRI was acquired with a mulitband factor of 3, covering 270 directions distributed over 3 diffusion shells of b-values 1000, 2000 and 3000 s/mm^2, plus 18 $b = 0$ (non-diffusion weighted) scans. The nominal voxel size was $1.25mm$ isotropic. Both T_1-weighted and T_2-weighted structural scans at $0.7mm$ isotropic resolution were also acquired.

Segmentation, surface reconstruction and one-to-one correspondance All pre-processing of the data, including correction for sequence-dependent artefacts such as eddy-current distortion, was performed by the "minimal preprocessing pipeline" provided by the HCP project [31]. This included the generation of native pial and white-matter surfaces, and their coregistration to a standard vertex mesh. This provides a one-to-one correspondance between the surface vertices of every subject, and hence permits vertex-wise analysis of tractography results across the HCP population.

White matter tractography and network construction Tractography was performed using FSL's BedpostX [62] and ProbtrackX2 [41–43]. BedpostX parameters included a specification of up to 3 fibres per voxel, and a deconvolution model using zeppelins [42, 43]. Probtrackx2 was run in "matrix3" mode, with all voxels in the white matter (as specified by a structural imaging mask) as seed points. The GM-WM surface boundary and all subcortical grey-matter voxels were specified as tractography target masks. Streamlines were kept and entered into the resultant connectivity matrix if they succeeded in traversing opposite directions from a seed voxel and reaching two different vertices on the target surface. One thousand streamlines were generated from every seed voxel. The result of tractography is therefore a connectivity matrix of size $[(\textit{number of target surface vertices}) + (\textit{number of target subcortical voxels})]^2$. In this study, only the surface vertices are analysed.

Threshold The structural connectivity graphs are binarised by zeroing everything below a chosen threshold. If the threshold chosen is too low the connectivity graphs are dominated by false positives. On the other hand, if a too high threshold is chosen then true connections are removed, leading to many false negatives. As probabilistic tractography is a probabilistic process, re-running the tractography on the same dataset gives a slightly different result. To investigate the effect of the chosen threshold and to find the optimum, tractography was re-run on two subjects and the connectivity graphs were created. The AUC between re-runs of the tractography were calculated for a range of thresholds between zero and 5300 counts. Figure S1 shows how well the runs pairwise predict each other for different thresholds. For low thresholds the performance is low due to all the false positives in the graphs. Around a threshold of 200 the predictive performance stabilises with only a small increase in the performance for higher thresholds. Based on this result we chose a threshold of 200. To investigate the effect of our choice we also ran all analyses with a threshold of 50 and 1000. This method to find the threshold of the graphs can be applied in other studies, but the specific threshold will depend upon the number of streamlines seeded per voxel, the resolution of the data and parameters of the tractography method.

Construction of population networks Population graphs are constructed by aggregating the binary graphs for the subjects included in the population. In this way population graphs become weighted graphs with weights representing the number of subjects in which a link is present.

The stochastic block model. The stochastic block model (SBM) clusters vertices together into homogeneous clusters according to their structural similarity. The generative model is:

$$\begin{aligned} \text{Links between nodes} \quad & A_{ij} \sim Bernoulli(\eta_{z_i z_j}) \\ \text{Link densities between clusters} \quad & \eta_{lm} \sim Beta(\beta^+, \beta^-) \\ \text{Clustering} \quad & \mathbf{z} \sim Categorical(\boldsymbol{\pi}) \\ & \boldsymbol{\pi} \sim Dirichlet(\boldsymbol{\alpha}) \end{aligned}$$

The nodes are partitioned into a given finite number of clusters K based on the Dirichlet distribution, allowing for flexible cluster sizes. The probability of links in the graph are generated according to a Bernoulli distribution, depending only upon the probability of observing links between clusters, which in turn follows a Beta distribution.

A structural connectivity graph can be represented by a binary $J \times J$ adjacency matrix $\boldsymbol{A}$. For all pairs of nodes i, j of the graph, $A_{ij} = 1$ and $A_{ij} = 0$ respectively denotes the existence or absence of a path in either direction from the tractography between i and j. Limited to undirected networks, A obeys that $A_{ij} = A_{ji}$.

When clustering for a population of S subjects, we consider $\boldsymbol{A} = \{A^1, ..., A^S\}$ the joint set of the individual graphs for the subjects that makes up the population.

To solve the clustering problem we seek a partition $\boldsymbol{z}$ of $\boldsymbol{A}$ into K clusters of nodes with similar structural connectivity pattern. Let $\boldsymbol{\pi}$ denote the probability distribution of any node belonging to the individual clusters, such that $p(z_i = k|\boldsymbol{\pi}) = \pi_k$, where $\boldsymbol{\pi} = \{\pi_1, ..., \pi_K\}$ and $\sum_{k=1}^K \pi_k = 1$.

To allow flexible cluster sizes, $\boldsymbol{\pi}$ is considered generated from a Dirichlet distribution:

$$p(\boldsymbol{\pi}|\boldsymbol{\alpha}) = \frac{1}{\mathrm{B}(\boldsymbol{\alpha})} \prod_{k=1}^K \pi_k^{\alpha_k - 1}, \qquad [1]$$

where B is the multivariate beta function:

$$\mathrm{B}(\boldsymbol{\alpha}) = \frac{\prod_{k=1}^K \Gamma(\alpha_k)}{\Gamma(\sum_{k=1}^K \alpha_k)}. \qquad [2]$$

This reveals the following joint prior over $\boldsymbol{z}$ and π:

$$p(\boldsymbol{\pi}, \boldsymbol{z}|\boldsymbol{\alpha}) \;=\; p(\boldsymbol{\pi}|\boldsymbol{\alpha}) \prod_{i=1}^J p(z_i|\pi) \;=\; \frac{1}{\mathrm{B}(\boldsymbol{\alpha})} \prod_{k=1}^K \pi_k^{m_k + \alpha_k - 1}, \qquad [3]$$

where m_k denotes the number of nodes belonging to cluster k, such that $\sum_{k=1}^K m_k = J$.

Imposing equal concentration parameter on all clusters $\frac{C}{K} = \alpha_1 = ... = \alpha_K$ and marginalizing over $\boldsymbol{\pi}$ we obtain the effective prior over $\boldsymbol{z}$, resulting in a so-called multivariate Pólya distribution:

$$p(\boldsymbol{z}|C) \;=\; \int p(\boldsymbol{\pi}, \boldsymbol{z}|C) d\boldsymbol{\pi} \;=\; \frac{\Gamma(C)}{\Gamma(C+J)} \prod_{k=1}^K \frac{\Gamma(\frac{C}{K} + m_k)}{\Gamma(\frac{C}{K})} \qquad [4]$$

For a given partition $\boldsymbol{z}$ the prior distribution on the probability η_{lm} of observing a link between nodes of cluster l and cluster m is imposed using the Beta distribution:

$$p(\eta_{lm}|\beta^+, \beta^-) = \frac{\Gamma(\beta^+ + \beta^-)}{\Gamma(\beta^+)\Gamma(\beta^-)} \eta_{lm}^{\beta^+ - 1} (1 - \eta_{lm})^{\beta^- - 1}.$$

The probability of observing a link between node i and j for subject s follows the Bernoulli distribution such that the likelihood of $\boldsymbol{A}$ is

given by (see also [25]):

$$p(\boldsymbol{A}|\boldsymbol{\eta},\boldsymbol{z}) = \prod_{s=1}^{S}\prod_{i>j}\eta_{z_i z_j}^{A_{ij}^s}(1-\eta_{z_i z_j})^{1-A_{ij}^s} = \prod_{l\geq m}\eta_{lm}^{N_{lm}^+}(1-\eta_{lm})^{N_{lm}^-}, \quad [5]$$

where N_{lm}^+ and N_{lm}^- respectively denotes the sum of all links and nonlinks between cluster l and m for all graphs in the population.

The conjugacy of the Beta prior and Bernoulli likelihood allows $\boldsymbol{\eta}$ to be analytically marginalized, revealing the following joint distribution:

$$\begin{aligned} p(\boldsymbol{A},\boldsymbol{z}|C,\beta^+,\beta^-) &= \int p(\boldsymbol{z}|C)\cdot p(\boldsymbol{A}|\boldsymbol{\eta},\boldsymbol{z})\cdot\prod_{l\geq m}p(\eta_{lm}|\beta^+,\beta^-)\,d\boldsymbol{\eta} \\ &= p(\boldsymbol{z}|C)\cdot\prod_{l\geq m}\frac{B(N_{lm}^+ + \beta^+, N_{lm}^- + \beta^-)}{B(\beta^+,\beta^-)}, \quad [6] \end{aligned}$$

where B denotes the beta function:

$$B(a,b) = \int \theta^{a-1}(1-\theta)^{b-1}d\theta = \frac{\Gamma(a)\Gamma(b)}{\Gamma(a+b)}$$

MCMC inference in the stochastic block model For a particular data set the model parameters are inferred using a sequence of independent Markov Chain Monte Carlo methods to sample from the posterior distribution.

The clustering is inferred using a combination of full and restricted Gibbs sampling procedures. In the full Gibbs sampling procedure, each node i is in turn proposed to be re-assigned, based on the posterior distribution of the single node assignment, obtained using Bayes' theorem for equation 6:

$$p(z_i = l|\boldsymbol{A},\boldsymbol{z}^{\backslash i},\beta^+,\beta^-,C) = \frac{p(\boldsymbol{A},\boldsymbol{z}^{\backslash i},z_i=l|\beta^+,\beta^-,C)}{\sum_m^K p(\boldsymbol{A},\boldsymbol{z}^{\backslash i},z_i=m|\beta^+,\beta^-,C)} \quad [7]$$

where $\boldsymbol{z}^{\backslash \boldsymbol{i}}$ denotes the cluster assignments for all nodes ignoring node i

In the restricted Gibbs sampling procedure, two clusters are randomly selected and three Gibbs sweeps are conducted, restricted to re-partitioning the nodes within the two selected clusters.

The three hyperparameters β^+,β^-,C are sampled individually using a Metropolis-Hastings procedure, where proposals are drawn from a Gaussian distribution with variance 1, centered at the current value of the parameter.

For all results in the paper, the following sampling procedure was utilized: one complete Gibbs sweep over all nodes followed by K restricted Gibbs proposals, followed by 10 Metropolis-Hastings proposals for each of the hyperparameters. A total of 100 sweeps of the above sampling procedure was performed. Following the last sweep of the MCMC sampling, the clustering was optimized towards a local posterior maximum using a hill-climbing procedure to repeatedly reassign the nodes one at a time to the cluster resulting in the highest posterior gain.

Ward clustering. Ward clustering [37] is initialised by assigning all nodes to their own cluster. In each step the two clusters are merged that produces the least reduction of the optimal value of the objective function, constrained to only merging adjacent clusters. The procedure can be continued until all nodes are in the same cluster. We use the dissimilarity measure $\mathbf{W}$ between the connectivity patterns of elements i and j of the connectivity matrix $\mathbf{A}$ as the objective function, as suggested by [17].

$$W_{ij} = \sqrt{\sum_{a\neq i,j}(A_{ia}-A_{ja})^2 + \sum_{a\neq i,j}(A_{ai}-A_{aj})^2} \quad [8]$$

K-means clustering. K-means clustering gives spatial homogeneous clusters solely based on the location of the vertices. Hence, the k-means clustering is not based on structural connectivity. Given the vertices of the average surface $(v_1, v_2, ..., v_n)$, where each observation is a 3-dimensional real vector containing the (x, y, z)-coordinates of a vertex, k-means clustering [40] partitions the n observations into k spatial homogeneous clusters $C = C_1, C_2, ..., C_k$ in which each observation belongs to the cluster with the nearest mean. The k-means clustering assigns an observation to a cluster by minimizing the within-cluster sum of squares.

$$\arg\min_{\mathbf{C}}\sum_{i=1}^{k}\sum_{\mathbf{x}\in C_i}\|\mathbf{x}-\boldsymbol{\mu}_i\|^2 \quad [9]$$

where μ_i is the mean of C_i.

Link prediction by area under receiver operator characteristics curve (AUC). We use the ability to predict links in holdout data to quantify how well structure is accounted for. A common procedure to quantify this performance is the area under curve (AUC) of the receiver operator characteristics (ROC) curve [24, 63]. AUC is used to measure the predictive performance, i.e., how well a given parcellation predicts a second structural connectivity graph. By using the AUC score it is possible to compare predictions made using different parcellations as well as non-parametric link prediction measures. Links and non-links are scored using a given modeling approach, and the AUC then quantifies how well the two classes of non-links and links are separated according to this score, where an AUC score of 0.5 indicates that the scoring procedure is no better than chance, and where an AUC score of 1 indicates that a threshold value of the scoring procedure exists which provides a perfect separation of links from non-links.

Parcellation based prediction. The score when predicting holdout data using a parcellation is given by

$$s_{ij}^{\text{Parcellation}} = \frac{N_{z_i z_j}^+}{N_{z_i z_j}}, \quad [10]$$

where $N_{z_i z_j}^+$ is the number of links between nodes in cluster z_i and nodes in cluster z_j and $N_{z_i z_j} = N_{z_i z_j}^+ + N_{z_i z_j}^-$ is the total number of possible links between nodes in cluster z_i and nodes in cluster z_j. The score $s_{ij}^{\text{Parcellation}}$ corresponds to the maximum likelihood estimate of $\eta_{z_i z_j}$ in equation 5.

Non-parametric link prediction measures. Let $d_i = \sum_j A_{ij}$ be the degree of node i and $\boldsymbol{A}$ define the $J \times J$ adjacency matrix of the training data. We use the following well-established measures to score for the existence of a link between node i and j [23, 24]:

$$\begin{aligned} s_{ij}^{\text{Common Neighbor}} &= \sum_t A_{it}A_{jt} & [11] \\ s_{ij}^{\text{Jaccard}} &= \frac{\sum_t A_{it}A_{jt}}{J - \sum_t (1-A_{it})(1-A_{jt})} & [12] \\ s_{ij}^{\text{Adamic/Adar}} &= \sum_t \frac{A_{it}A_{jt}}{\log(d_t)} & [13] \\ s_{ij}^{\text{Preferential Attachment}} &= d_i d_j & [14] \\ s_{ij}^{\text{ShortestPath}} &= \frac{1}{\text{ShortestPath}(\boldsymbol{A},i,j)}, & [15] \end{aligned}$$

where $\text{ShortestPath}(\boldsymbol{A}, i, j)$ gives the shortest path in the structural connectivity graph $\boldsymbol{A}$. The above scores are averaged over the S training subjects and evaluated on holdout test data from six test subjects.

Reliability estimation by Mutual Information. In order to quantify similarity between two partitions $\boldsymbol{z}$ and $\boldsymbol{z'}$ we use normalized mutual information (NMI), defined as:

$$NMI(\boldsymbol{z},\boldsymbol{z'}) = \frac{2\cdot MI(\boldsymbol{z},\boldsymbol{z'})}{MI(\boldsymbol{z},\boldsymbol{z}) + MI(\boldsymbol{z'},\boldsymbol{z'})},$$

where the mutual information (MI) is given as:

$$MI(\boldsymbol{z}, \boldsymbol{z'}) = \sum_{kk'} P(k,k') \log(\frac{P(k,k')}{P(k)P(k')}),$$

with $P(k,k')$ being the probability that a node in cluster k in the first partition is in cluster k' in the second partition. NMI takes values between zero and one where one indicates that a permutation of the groups exists such that the partitions are identical, and zero indicates that the partitions are perfectly independent.

The Atlases. The Desikan-Killiany atlas [11] and the Destrieux atlas [32] are both generated using manually labeled data as the basis for a subsequent automated parcellation procedure [12]. The procedure incorporates both geometric information derived from the cortical model, and neuroanatomical convention, as found in the training set. This improves the parcellation in regions in which geometry alone is not predictive of a parcellation label.

The two atlases differ in the definition of the gyri. The Desikan-Killiany atlas is a gyral based atlas, i.e., a gyrus is defined as running between the bottoms of two adjacent sulci. That is, a gyrus includes the part visible on the pial view and the adjacent banks of the sulci limiting this gyrus. The Destrieux atlas is a mixed, sulco-gyral-based parcellation: the gyral cortex is defined as the part visible on the pial view, the remaining hidden part being conversely labeled sulcal.

The Desikan-Killiany atlas The Desikan-Killiany atlas [11] is based on a dataset of 40 MRI scans from a variety of subjects including young, middle-aged and elderly controls, as well as patients with Alzheimer's disease. Full details are available elsewhere ([11]), but are repeated here in brief for completeness. A total of 34 cortical regions were manually identified in each hemisphere on volumetric T1-weighted MRI images using a 'sulcal' approach (manually tracing from the depth of one sulcus to another, thus incorporating the gyrus within) to define most structures, guided by standard neuroanatomical conventions based on brain atlases, modifications to previous published definitions and expert knowledge.

The volumetric ROIs were transposed onto the inflated cortical surface of each reconstructed brain and the final anatomic labels were generated using anatomic information regarding local curvature (e.g. the presence of sulci).

A cortical atlas was generated using a registration procedure that aligns the cortical folding patterns and probabilistically assigns a neuroanatomical region to every point in the cortical surface. This was done by generating a spherical representation of each brain by minimizing the metric distortion between the cortical and the spherical representations. Second, the spherical surfaces were registered together. This established a spherical surface-based coordinate system that was adapted to the folding pattern of each individual subject, thus allowing for increased precision in registering anatomic features of the human brain across subjects. Third, a spherical statistical atlas was used to label the cortical surfaces into neuroanatomical regions of interest.

The Destrieux atlas The Destrieux atlas [32] is based on a parcellation scheme that first divided the cortex into gyral and sulcal regions, the limit between both being given by the values of local mean curvature or average convexity of the surfaces. Full details are available elsewhere ([32]), but are repeated here in brief for completeness. A gyrus was defined to be only the portion of the cortex that was visible on the pial view, whereas the remaining, hidden cortex (banks of sulci) were defined as belonging to a sulcus. For a few large structures, an additional sub-parcellation was used based on estimated cytoarchitectonic and functional criteria and some parcellations that were very small or very variable were grouped with a larger neighboring parcellation unit. Finally, each hemisphere was segmented into 74 different sulco-gyral cortical units.

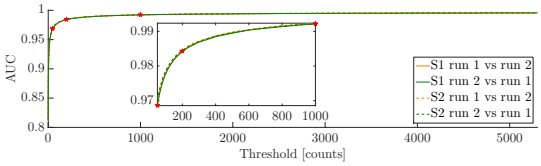

Fig. S1. AUC vs. threshold. For two subjects the tractography procudure was performed twice with different initialisation. The figure shows how well the two runs predict each other for a range of thresholds between zero and 5300 measured by AUC. The red stars indicate the tested thresholds.

Table S1. Average AUC across six test subjects and five restarts when predicting unseen connectivity graphs using data-driven parcellations including the singleton parcellation in which each node is given its own cluster, as well as the considered non-parametric link predictors and the three considered atlases. The scores are given for the optimal number of parcels (SI, Figure S7). For k-means clustering, the single subject score is given for 360 parcels, while remaining scores are given for 1000 parcels. In parentheses is given the standard deviation of the mean on last digit across different training networks.

	Population size			
	Single (n=3)	5 (n=3)	10 (n=2)	20 (n=1)
SBM	0.9486 (22)	0.9790 (1)	0.9831 (2)	0.9857
Ward clustering	0.9615 (19)	0.9799 (1)	0.9833 (2)	0.9857
k-means	0.9143 (9)	0.9381 (5)	0.9427 (4)	0.9451
Singleton	0.7027 (120)	0.8541 (27)	0.9016 (1)	0.9336
Shortest path	0.9453 (25)	0.9830 (3)	0.9862 (2)	0.9875
Common neighbor	0.9339 (63)	0.9792 (9)	0.9843 (4)	0.9865
Jaccard	0.9368 (64)	0.9816 (2)	0.9855 (2)	0.9874
Adamic/Adar	0.9346 (63)	0.9798 (8)	0.9848 (3)	0.9869
Preferential attach.	0.5756 (25)	0.6100 (6)	0.6188 (2)	0.6247
HCP_MMP1.0	0.9595 (9)	0.9777 (1)	0.9796 (5)	0.9807
Destrieux	0.9599 (9)	0.9670 (2)	0.9681 (9)	0.9687
Desikan-Killiany	0.9479 (7)	0.9524 (6)	0.9530 (14)	0.9535

A set of 12 subjects was used to develop and test the anatomical rules which labeled every point of the cerebral cortex, while another dataset of 12 subjects was used to train the automated labeling software.

The probability of a label at a certain vertex is based on a number of pieces of information, including the curvature and average convexity of the cortical surface, prior labeling probability for that vertex, as well as the labels of vertices in a local neighborhood.

The Human Connectome Project Multi-model Parcellation (HCP_MMP1.0) atlas This recently released atlas [19] comprises 180 parcels per hemisphere, and was generated using a novel combination of machine-learning and interactive editing by neuroanatomists. Using a combination of modalities, including fMRI, myelin maps and structural imaging, 210 subjects were aligned using an areal-matching algorithm, and subsequently the surface gradients of the different modalities were used to propose parcel borders. These were then edited and documented by neuroanatomists, and the subsequent parcellations used, together with the multimodality data, to train a classifier for automatic delineation of similar borders on a validation set. The final group maximum probability map (MPM) parcellation was then formed from the individual probabilistic areal maps.

Supporting Figures.

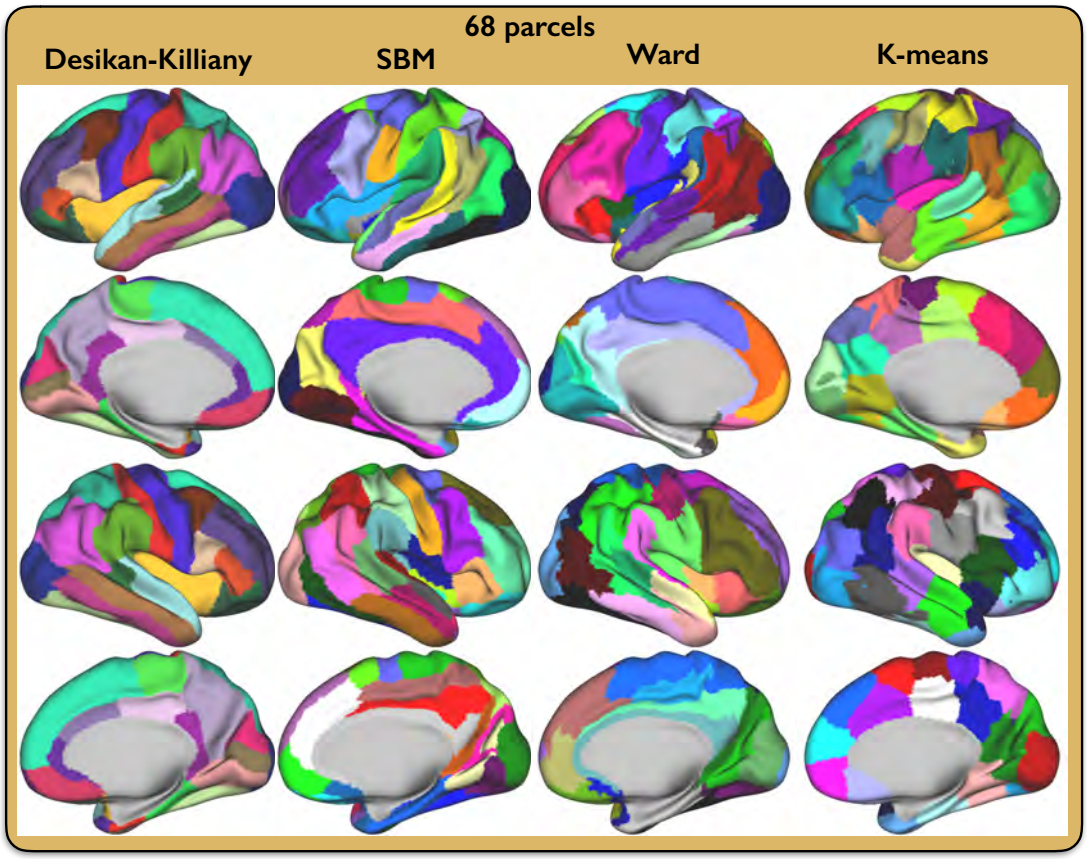

Fig. S2. Parcellations with 68 clusters for a population of 20 subjects and a threshold of 200, shown on the inflated surface. From left: The Desikan-Killiany atlas, SBM parcellation, Ward clustering, and K-means clustering.

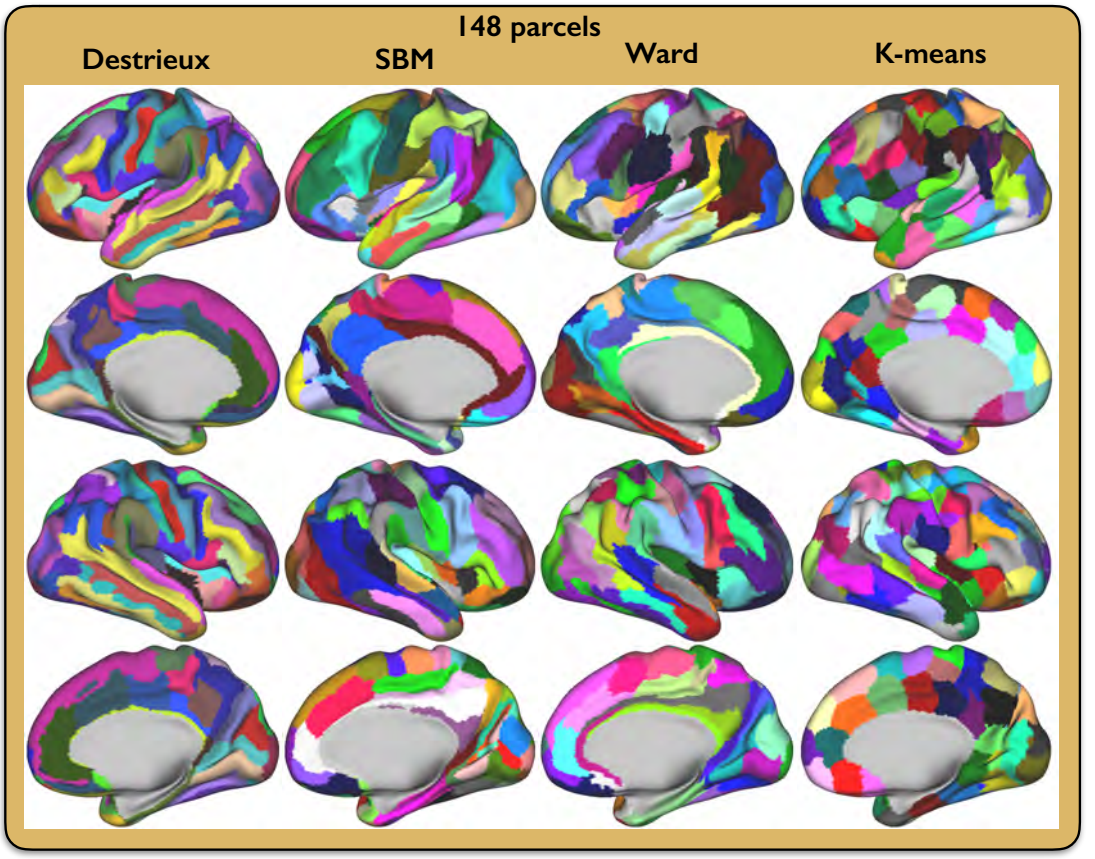

Fig. S3. Parcellations with 148 clusters for a population of 20 subjects and a threshold of 200, shown on the inflated surface. From left: The Destrieux atlas, SBM parcellation, Ward clustering, and K-means clustering.

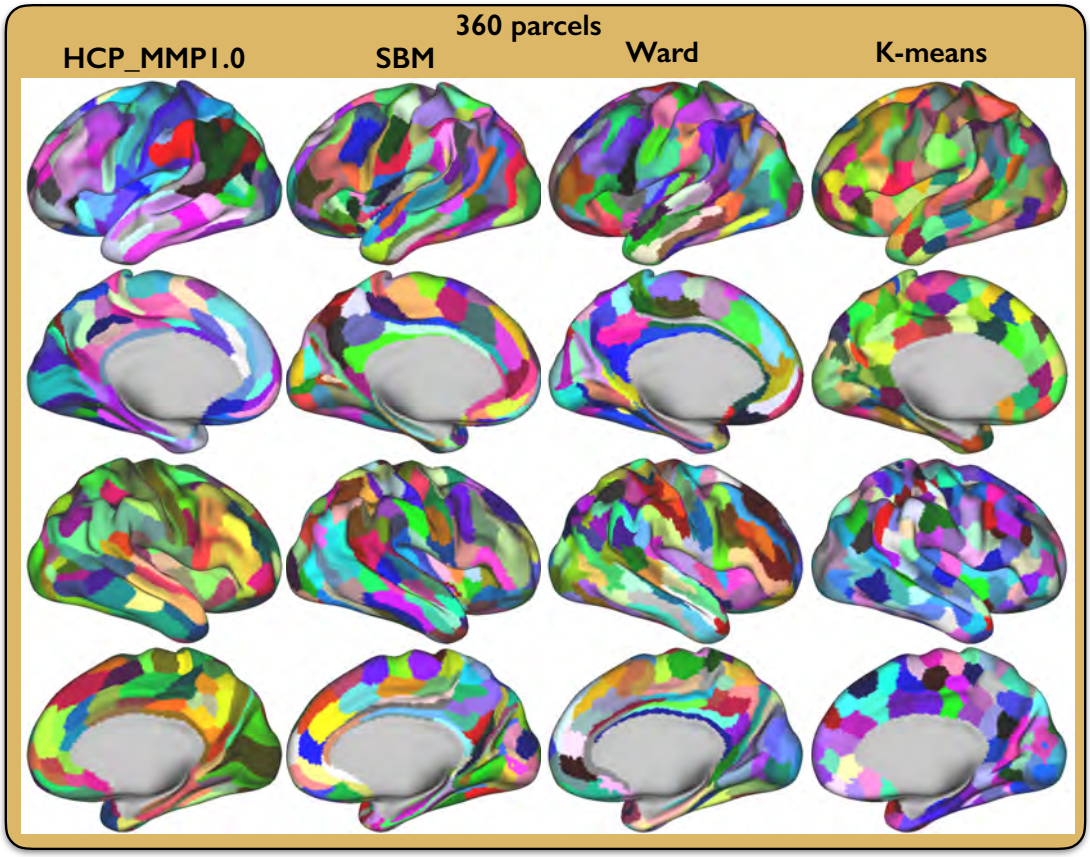

Fig. S4. Parcellations with 360 clusters for a population of 20 subjects and a threshold of 200, shown on the inflated surface. From left: The Human Connectome Project multi-modal parcellation (HCP_MMP1.0), SBM parcellation, Ward clustering, and K-means clustering.

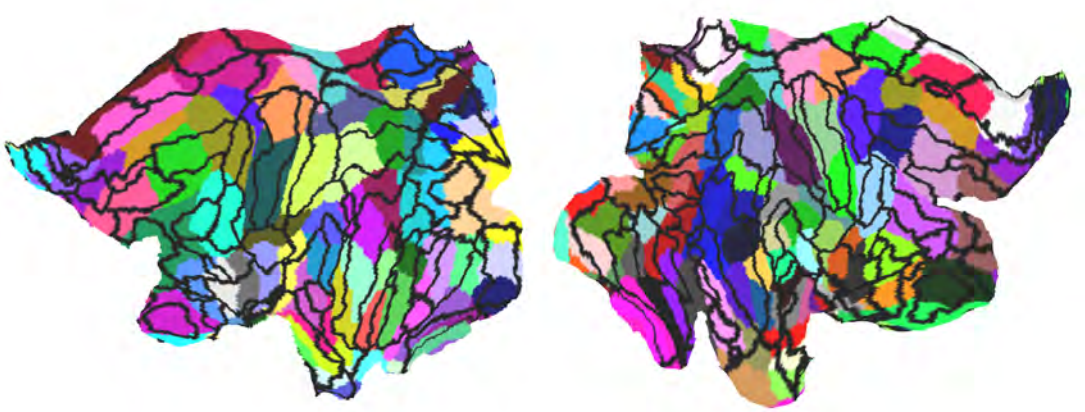

(a)

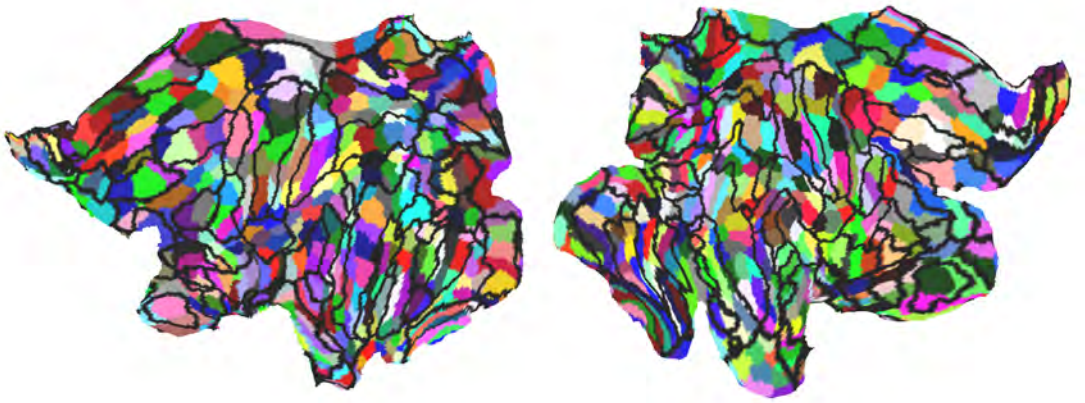

(b)

Fig. S5. Flatmaps of the SBM parcellations with (a) 148 clusters and (b) 700 clusters overlaid with the borders of the Destrieux atlas.

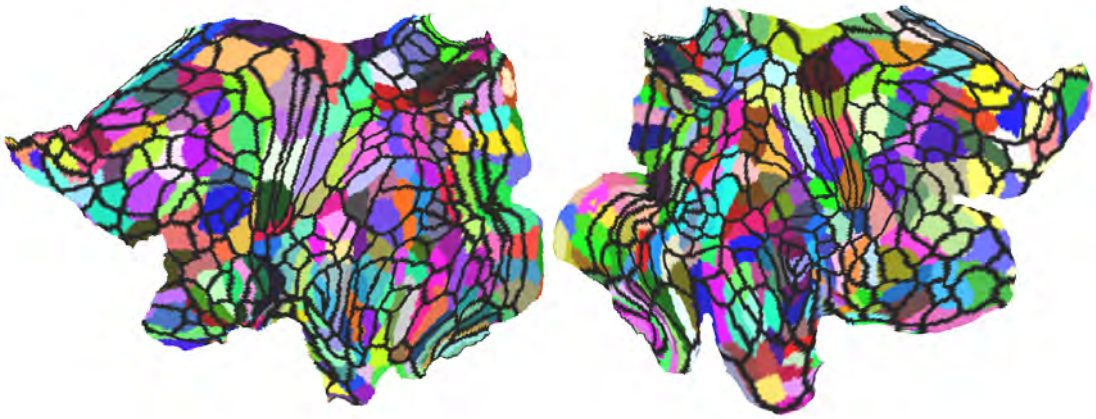

(a)

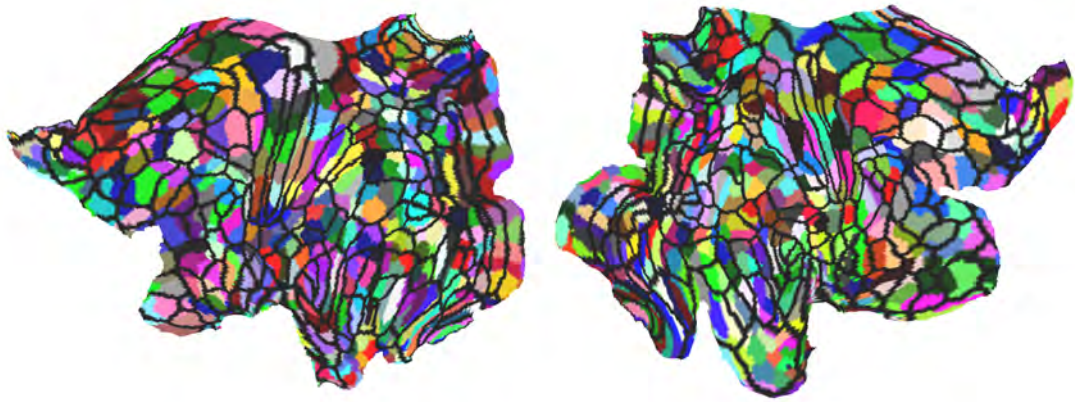

(b)

Fig. S6. Flatmaps of the SBM parcellations with (a) 360 clusters and (b) 700 clusters overlaid with the borders of the HCP_MMP1.0 atlas.

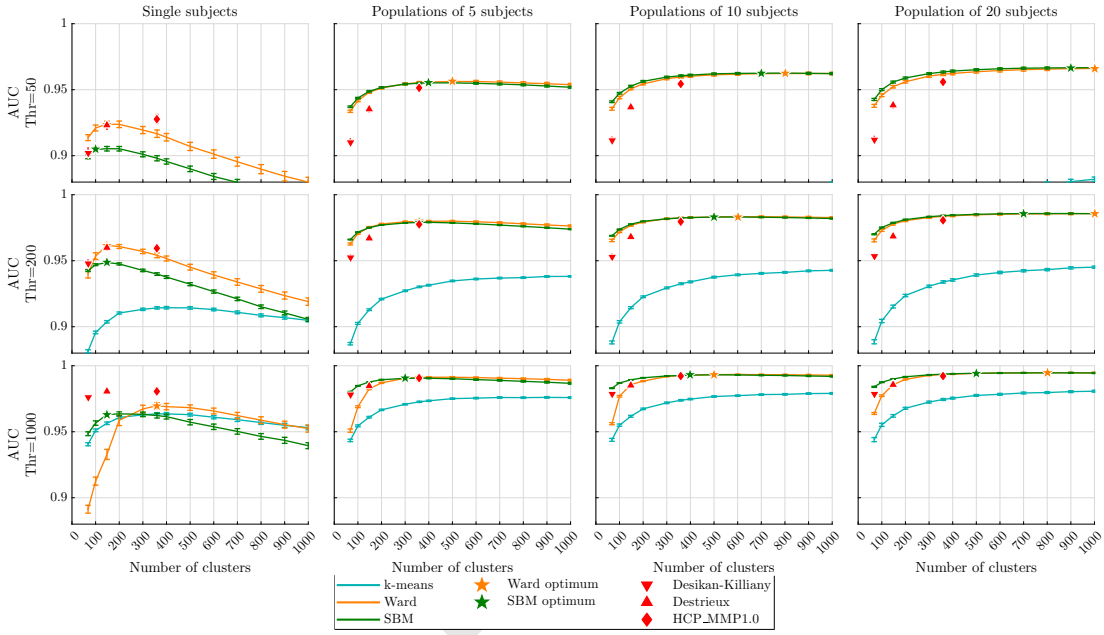

Fig. S7. Average AUC across the six test subjects vs the number of clusters for thresholds of 50, 200 and 1000, and population sizes of 1, 5, 10 and 20. The error bars indicate the standard deviation of the mean across the six test subjects. The stars mark the optimal number of clusters for the stochastic block model (green) and ward clustering (yellow), as no significant increase in performance is observed by using more clusters. The optimal number of clusters are found using a paired t-test.

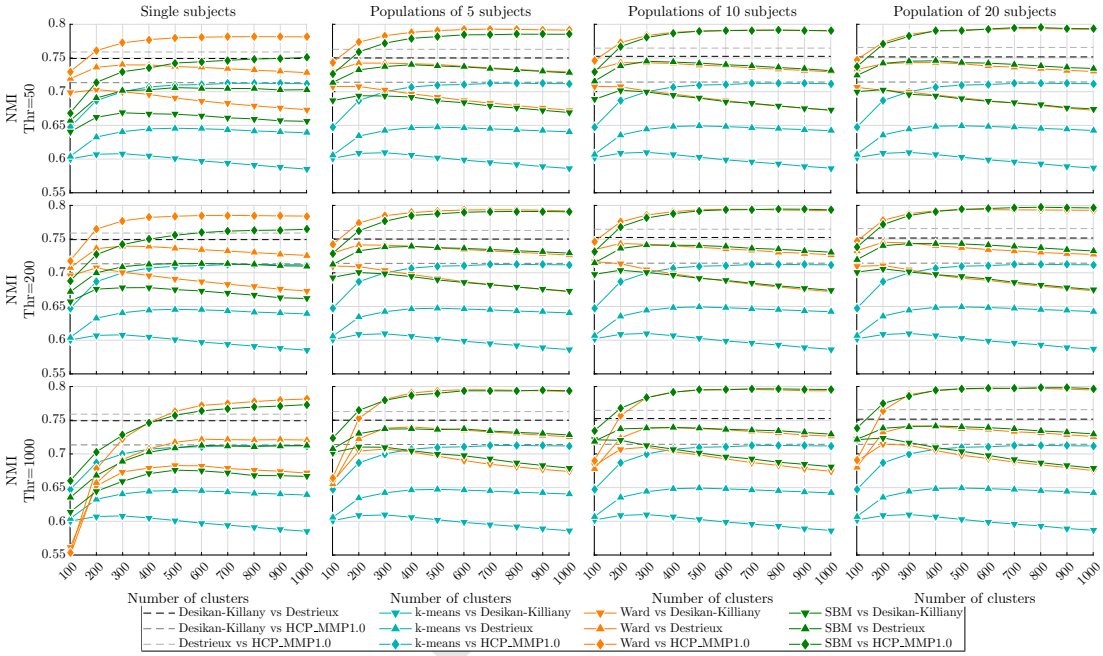

Fig. S8. Normalised mutual information (NMI) vs the number of clusters for thresholds of 50, 200 and 1000, and populations of of 1, 5, 10 and 20 subjects. Dashed lines show the reliability of the methods, NMI between Desikan-Killiany and Destrieux (black), between Desikan-Killiany and HCP_MMP1.0 (gray), and between Destrieux and HCP_MMP1.0 (light gray). Solid lines show NMI between the three parcellation approaches, the stochastic block model (green), ward clustering (yellow) and k-means clustering (blue), and Desikan-Killiany (downward-pointing triangles), Destrieux (upward-pointing triangles) and HCP_MMP1.0 (diamonds).

Paper D

Ambrosen, K. S., Eskildsen, S. F., Hinne, M., Krug, K., Lundell, H., Schmidt, M. N., van Gerven, M. A. J., Mørup, M., Dyrby, T. B., 'Validation of Structural Brain Connectivity Networks', *in preparation*

Validation of Structural Brain Connectivity Networks

Karen S. Ambrosen(a,b,*), Simon F. Eskildsen(c), Max Hinne(d), Kristine Krug(e), Henrik Lundell (b), Mikkel N. Schmidt(a), Marcel A. J. van Gerven(d), Morten Mørup(a) and Tim B. Dyrby(a,b)

a) Department of Applied Mathematics and Computer Science, Technical University of Denmark, Richard Petersens Plads, Building 324, DK-2800 Kgs. Lyngby, Denmark
b) Danish Research Centre for Magnetic Resonance, Center for Functional and Diagnostic Imaging and Research, Copenhagen University Hospital Hvidovre, Kettegaard Allé 30, DK-2650 Hvidovre, Denmark
c) Center of Functionally Integrative Neuroscience (CFIN), Institute of Clinical Medicine, Aarhus University, Nørrebrogade 44, DK-8000 Aarhus C, Denmark
d) Donders Institute for Brain, Cognition and Behaviour, Radboud University, Nijmegen, The Netherlands
e) Department of Physiology, Anatomy and Genetics, University of Oxford, Oxford OX1 3PT, UK.

Abstract

Diffusion magnetic resonance imaging based tractography is a unique non-invasive tool for studying the brain's structural connectivity (SC) in vivo. However, the derivation of SC networks is dependent on multiple parameters, from scan acquisition parameters to tractography algorithm specific parameters. So far, the focus has mainly been on the choice of diffusion model, tractography algorithm and parameters specific to those. Herein we validate SC networks derived from data acquired from a post mortem monkey brain that span a wide range of acquisition parameters, i.e. spatial resolution, angular resolution and b-value. As gold standard for SC the invasive tracer network obtained in monkeys by Markov et al. (2014) was used. Interestingly, we find that SC networks derived from data with low spatial resolution (1 mm^3) are in better agreement with the tracer network, than those derived from high resolution data (0.5 mm^3). High angular resolution and SNR are key, especially when the spatial resolution is low, to extract the rich but compressed anatomical details provided in the data. How to define the sufficient image resolution, to ensure that the generated SC network agrees with ground truth, might be closely related to the coarseness of the employed cortical parcellation.

Introduction

Tractography based on diffusion magnetic resonance imaging (dMRI) is an unique tool for studying both specific brain connections (i.e. tracts) as well as the structural brain network (i.e. structural connectivity (SC)) and its organization non-invasively (Le Bihan & Johansen-Berg 2012; Van Essen et al. 2014). Tractography can be used to estimate the fiber bundles in the brain and hence estimate the brain's structural organization, i.e. the connectome (Sporns et al. 2005; Hagmann 2005). Analyzing whole brain SC using graph theoretic measures have been shown useful for classification of healthy and diseased subjects (Iturria-Medina 2013). When using tractography to study specific tracts, diffusion tensor imaging (DTI) (Pierpaoli et al. 1996; Basser et al. 1994) or other local microstructural estimates can be related to clinical scores, brain maturation (Lebel et al. 2008) or ageing (Bennett et al. 2010). Furthermore, tractography enables parcellation of the cortex (Baldassano et al. 2015; Parisot et al. 2016; Ambrosen et al. 2014; Fan et al. 2016) or

subcortical structures based on SC (Behrens, Johansen-Berg, et al. 2003; Wiegell et al. 2003).

The estimation of the brain's structural organization consists of a comprehensive data processing pipeline, including correction of acquisition related artifacts, fiber reconstruction and streamline tractography (Meskaldji et al. 2013; Jones & Cercignani 2010; Jones et al. 2013; Jbabdi et al. 2015; Qi et al. 2015). The fiber orientation distributions are modelled from the diffusion weighted images and the connectivity between gray matter (GM) regions are estimated using a tractography algorithm. Although tractography is a unique tool for mapping the connections between cortical regions, it does not relate to the features of the connections, such as conduction velocity and delays. All these methodological choices and parameter settings, both in the acquisition (i.e. scanner parameter settings), in the estimation of the diffusion orientation distributions (model selection), and in the tractography (algorithm selection, number of streamlines, curvature threshold, step length, and definition of seeding strategy and target regions, etc.), as well as in the post-tractography stage (threshold, normalization), introduce different uncertainties in the estimation of the connections and impacts the final SC network. Indeed tractography uniquely allows non-invasive mapping of the brain network but is challenged by the generation of multiple false-positive connections (Maier-Hein et al. 2016; de Reus & van den Heuvel 2013; Thomas et al. 2014). It has been shown that only 60-65% of the connections estimated using tractography are correct (Calabrese et al. 2015; Donahue et al. 2016). Recently the ISMRM diffusion challenge on diffusion tractography, based on a human brain phantom with ground truth-connections, showed how dependent the tractography results are on the individual processing steps (Maier-Hein et al. 2016). Despite these limitations, there exist a vast literature of tractography studies demonstrating its potential for studying the brain's structural organization in both health (Gong et al. 2009; Robinson et al. 2010; Wen et al. 2011; Scholz et al. 2009) and disease (Shu et al. 2011; Lo et al. 2010; Jahanshad et al. 2015; Skudlarski et al. 2010; Zalesky et al. 2011). Although all these methodological choices and parameter settings affect the tractography, hence the final SC network, the key is the anatomical information present in the data determined by the chosen scan parameters.

Validation of the derived SC networks is therefore of great importance. Invasive tracers can be used to verify both the connectivity (i.e. whether or not two regions are connected) and the projection (i.e. the route and shape of the tract). Tractography and structural connectomes have previously been validated using invasive tracer (Dyrby et al. 2007; Knösche et al. 2015; Thomas et al. 2014; Dauguet et al. 2007; van den Heuvel et al. 2015; Azadbakht et al. 2015; Donahue et al. 2016), but the impact of the data acquisition parameters on the derived connectome have not been investigated. Previous studies have tested how different parameters affect the estimated connectome, either by investigating how different graph measures, such as graph density, shortest paths, etc., are affected (Bastiani et al. 2012), by investigating variations in the derived connectivity networks (Jones 2004; Zhan et al. 2012; Gigandet et al. 2013) or in the estimated WM tracts (Vos et al. 2016; Gigandet et al. 2013) or by validating tractography by comparison to tracer studies, either by comparing specific tracts (Thomas et al. 2014; Knösche et al. 2015; Dyrby et al. 2007; Dauguet et al. 2007) or by comparing the SC network with a network obtained using invasive tracers (van den Heuvel et al. 2015; Azadbakht et al. 2015; Donahue et al. 2016). Until now

the validation of tractography/SC have been focused on the validation of the tractography method and their cross-comparison, both for extracting specific tracts and for networks (Bastiani et al. 2012; Thomas et al. 2014; Villalon-Reina et al. 2016), as well as the influence of tractography specific parameters, such as the FA threshold (Bastiani et al. 2012; Azadbakht et al. 2015; Dauguet et al. 2007), the curvature threshold (Bastiani et al. 2012; Dauguet et al. 2007; Azadbakht et al. 2015), the integration step length (Dauguet et al. 2007), and the probabilistic thresholding (Bastiani et al. 2012). Although, image quality of the diffusion MRI data used often is concluded of possible importance for the results no studies have yet validated the impact of key acquisition parameters i.e. angular resolution, b-value and image resolution. Zhan et al. (Zhan et al. 2012) shows that the final connectome is affected by spatial and angular resolutions, but does not validate the estimated connectomes.

Here we provide an extensive validation of the impact of such key data acquisition parameters using an extensive ex vivo acquisition setup by comparison to a SC network based on invasive tracers (Markov et al. 2014). We quantify how key acquisition parameters: image resolution, angular resolution, i.e. number of directions, and b-value impact the final connectome. Furthermore, the effect of streamline count threshold, seeding strategy, number of acquisitions versus SNR and the integration step-length in the tractography algorithm are quantified. The generated connectomes across the different combinations of parameters are validated by comparison to the state-of-the-art 91x29 tract tracing graph of the macaque brain generated using invasive retrograde tracers (Markov et al. 2014). In the comparison, cross entropy is used as a similarity measure, together with sensitivity and specificity, where the tracer graph is assumed ground truth.

Materials and Methods

Retrograde tract tracing data

As a ground truth SC network, we used a unique tracer connectivity dataset collected on macaque monkeys by Markov et al. (Markov et al. 2014), quantifying the intrahemispheric interareal connectivity of the macaque cerebral cortex using retrograde tracer injections. Retrograde tracer was injected into 29 regions and labeled neurons were counted in 91 regions, generating a 91 x 29 weighted and directed connectivity graph. The volume of the injections varied across injection areas. The regions were defined by a reference atlas containing 91 cortical regions mapped to the left hemisphere of an individual macaque (M132). The M132 parcellation was based on a combination of histological criteria and atlas-based landmarks. The M132 macaque was registered to the F99 reference space using landmark-based surface registration (Markov et al. 2014). Although tracer was injected in both hemispheres, all injection and target sites were mapped to the left hemisphere. The weights in the graph are the extrinsic fraction of labeled neurons (FLNe). The FLNe value of an area was estimated by the number of labeled neurons in that area relative to the total number of labeled neuron excluding the labeled neurons intrinsic to the injected area (Markov et al. 2014; Markov et al. 2011).

$$FLNe = \frac{|i|}{|k| - |j|}$$

where |*i*| is the number of labeled neurons in the source area, |*k*| is the total number of labeled neurons in the brain, and |*j*| is the number of labeled neurons in the target area (injection area). As the FLNe values were normalized per injection site the number of labeled neurons from each injection area sum to one and can thus be treated as a probability distribution. The FLNe values in the tracer graph are assumed ground truth in our validation of SC graphs. The tracer data has been downloaded from http://core-nets.org.

Animal

One postmortem monkey brain from a male Rhesus macaque (M105) was scanned using dMRI. The animal was 4 years and 10 months old and weighted 10.1 kg at the time of perfusion. M105 was perfused at Oxford University. When the brain was removed from the skull (post mortem), a small incision was made in the brain tissue of the occipital lobe in the left hemisphere, causing that the white matter tract to the occipital region was cut. Since the tract was cut post mortem, the integrity of the axons in vivo is normal hence so ex vivo. The incision can be seen on high resolution MRI. Although the left hemisphere was damaged, it was included in the analyses as an additional validation of our setup, expecting it to be in less agreement with the tracer graph, than the intact hemisphere. All animal procedures were carried out in accordance with Home Office (UK) Regulations and European Union guidelines (EU directive 86/609/EEC; EU Directive 2010/63/EU).

MRI acquisition

Imaging of the ex vivo monkey brain was performed on an experimental 4.7 T Agilent scanner with a quadrature volume RF coil and a maximum gradient strength of 400 mT/m. Free fixative was washed out to increase T2-relaxation using phosphate buffered saline (PBS) following the preparation stages in the setup in (Dyrby et al. 2011). The brain was placed in a sealed plastic bag with minimal PBS surrounding the brain tissue and stabilised to room temperature before scanning. Using a mechanically stable setup, the brain was placed in the middle of the volume coil. To ensure constant temperature while scanning, a conditioned flow of air around the brain was used and the temperature was measured at the end of the magnet (19±1 ºC). To ensure removal of any short-term mechanic and thermal instabilities, a diffusion weighted pre-scan with a duration of 18 hours was acquired (Dyrby et al. 2011).
The scanning protocol used a spin-echo sequence with single-line readout. Whole-brain coverage with high-resolution isotropic 0.5³ mm³ voxels was obtained with a matrix size of 128x256, field-of-view: 64 x 128 mm², 91 slices and slice thickness of 0.5 mm. Three shells with different b-values were acquired: b = [1610, 4100, 7700] s/mm² by varying the gradient strength, G = [150, 250, 350] mT/m and keeping constant delta = 8.4 ms, DELTA = 15 ms as well as the echo time TE = 30 ms. The repetition time; TR = [8000, 7900, 8600] ms. Each b-value was acquired using a shell that included in total 180 directions, generated using electrostatic repulsion (Jones 2004). The 180 shell was designed to include a subset of 20 and 60 uniformly distributed non-collinear directions; First, 20 uniformly distributed non-collinear directions were generated. These were held fixed and 40 additional directions

were generated such that in total 60 directions were uniformly distributed. The same procedure was applied for generating in total 180 directions by keeping the optimal distributed 60 directions fixed.

Data processing

Visual quality inspection of the ex vivo dMRI dataset revealed no need for any post processing. Low resolution datasets with 1.0 mm^3 isotropic spatial resolution was generated by linearly downsampling of the acquired high-resolution dataset with a sampling factor of 2 using the FSL tool (Woolrich et al. 2009; Smith et al. 2004; Jenkinson et al. 2012). The sampling factor ensured that new voxels were centered on old voxels emulating the acquisition of that image resolution. Finally, a brain mask was made by averaging, thresholding and binarizing the diffusion weighted images (i.e. excluding the non-diffusion weighted images (b=0 s/mm^2)) and subsequently manually edited.

Template creation

Standard space was defined using the Paxinos Rhesus monkey atlas. We created an average template of 15 vervet MPRAGE scans in standard space using a series of linear and non-linear registrations as described in (Fonov et al. 2011).

Surface extraction

We extracted cortical surfaces by applying Fast Accurate Cortex Extraction (FACE) on the average b0 image (Eskildsen et al. 2005; Eskildsen & Ostergaard 2006; Eskildsen & Ostergaard 2007). First, a brain mask was generated using a simple threshold followed by morphological operations to remove noise and fill holes. Then, the b0 image was denoised (Coupe et al. 2008), bias field corrected (Sled et al. 1998), and spatially normalized to the template in standard space by applying linear (Collins et al. 1994) and non-linear (Collins et al. 1994; Collins & Evans 1997) registrations. Probability maps for white matter (WM), gray matter (GM), and cerebro-spinal fluid (CSF) were calculated using a fuzzy clustering algorithm. The WM probability map was thresholded, amended with a mask of deep GM structures obtained from the template, and topology corrected (Chen & Wagenknecht 2006). An initial surface was generated by applying marching cubes on the resulting WM component. This initial WM surface was iteratively fitted to the cortical WM-GM interface. The resulting surface was subsequently fitted to the GM-CSF interface by inflating the surface as described in (Eskildsen & Ostergaard 2006). A surface estimating the middle cortical layer was subsequently generated from the WM-GM surface and GM-CSF surface.

In the tractography, the WM surface containing 118,671 vertices in the left hemisphere and 121,818 vertices in the right hemisphere, was used as seed mask (GM seeding) and target mask (both seeding strategies), while the pial surface is used as the termination mask (both seeding strategies). The thresholded WM probability map was used as seed mask in the tractography when WM seeding was used. A mask of the subcortical structures and the ventricles was made by segmenting the average b0 image using FSL's FAST algorithm (Zhang et al. 2001) and manually edited. This mask was used as exclusion mask in the tractography.

Surface parcellation

We used the macaque M132 atlas to define the cortical parcellation. The F99 mid-cortical surface was non-linearly warped to standard space using a deformation field calculated by applying Advanced Normalization Tools (ANTs) (Avants et al. 2008) on the F99 image (Van Essen 2002) and the b0 image in standard space. The F99 T1-weighted image was skull stripped using FSL's brain extraction tool and the eyes were manually removed. The b0 mid-cortical surface was then matched to the F99 surface using a feature driven surface registration algorithm (Eskildsen & Østergaard 2008). The M132 parcellation was mapped to the B0 WM-GM surface via the B0 mid-cortical surface and the inherent correspondence obtained from the FACE process. Coherent labels were ensured by morphologically removing any label-wise "salt-and-pepper noise" in the mapped parcellation. Due to the fact that no vertices on the native WM surface were assigned to the piriform region, this region was excluded and only the 90x29 tracer graph was used in the analysis.

Tractography and connectivity matrices

The fiber orientations were estimated using FSL's bedpostX algorithm allowing up to three crossing fibers per voxel (Jbabdi et al. 2013; Behrens, Woolrich, et al. 2003; Behrens et al. 2007). Probabilistic tractography was performed in native space using the ball and stick probabilistic tractography algorithm implemented in FSL's probtrackx2 (Behrens et al. 2007; Behrens, Woolrich, et al. 2003). In the tractography a step length of ¼ voxel size (Jbabdi et al. 2013; Thomas et al. 2014) with a curvature constraint of 80 degrees was used. Two different seeding strategies were applied, white matter (WM) seeding and gray matter (GM) seeding. In WM seeding, all voxels within WM were seeded with 2000 streamlines and only those streamlines that intersected the WM surface at two locations were kept. In GM seeding, 5000 streamlines are initiated in each vertex of the WM surface and streamlines that reached another vertex of the WM surface was kept. For both seeding strategies, the streamlines were terminated if they crossed the pial surface and excluded if it traversed subcortical structures or ventricles. The retrograde tracer data is only available for intrahemispheric connections and hence the tractography is performed for the two hemispheres separately.

Both seeding strategies result in two SC matrices, **A**, one for each hemisphere. The size of the SC matrices is determined by the number of vertices on the WM surface, yielding a 118,671 x 118,671 matrix for the left hemisphere and a 121,818 x 121,818 matrix for the right hemisphere. The SC matrices obtained using WM seeding is symmetric due to the bidirectional approach, whereas the SC matrices obtained from GM seeding is made symmetric by taking the arithmetic mean of the streamline counts, i.e. $\left(\frac{A_{ij} + A_{ji}}{2}\right)$.

When running tractography for all combinations of the parameters under investigation: 3 b-values (1600, 4100 and 7700 s/mm²), 3 shells (20, 60 and 180 directions), 2 spatial resolutions (0.5 mm³, 1.0 mm³), 2 seeding strategies (WM and GM seeding) and 2 hemispheres, it resulted in 72 different SC graphs to be validated against the tracer graph.

Cross entropy

The goal is to validate different dMRI protocols against ground truth, where ground truth is assumed to be the FLNe values in the tracer graph, denoted as $\boldsymbol{\theta}_j^{tracer}$ for a given target region j. To evaluate the quality of the extracted SC graphs, we calculated the cross entropy (Shannon 1948; Kullback & Leibler 1951) between the tract tracing graph (Markov et al. 2014) and the SC graphs. Cross entropy is an information theoretic measure that measures the average information needed to encode data from a "true" probability distribution (FLNe tracer data) using a "surrogate" distribution (SC graph data). In other words, cross entropy measures how close the estimated distribution is to the true distribution. The cross entropy (H) is calculated column-wise of the connectivity matrices and given by

$$H(\boldsymbol{\theta}_j^{tracer}, \boldsymbol{\theta}_j^{diffusion}) = -\sum_i \theta_{ij}^{tracer} \log(\theta_{ij}^{diffusion}) \tag{1}$$

where $\boldsymbol{\theta}_j^{tracer}$ is the distribution of relative tracer connectivity probabilities and $\boldsymbol{\theta}_j^{diffusion}$ is a distribution of relative SC probabilities derived from the structural connectivity graph. The j index is the target region (columns in the tracer graph) and the i index is the source region (rows in the tracer graph).

In order to quantify the cross-entropy, $\boldsymbol{\theta}_j^{diffusion}$ which is unknown needs to be estimated from the SC graph data. As cross-entropy is not defined in regions where $\theta_{ij}^{diffusion}$ is zero (i.e., $\log(0) = -\infty$) this distribution has to be robustly estimated. We therefore infer $\boldsymbol{\theta}_j^{diffusion}$ using Bayesian inference. The (prior) probability of a streamline reaching one of the $K = 90$ cortical regions in the M132 parcellation is modelled by a Dirichlet distribution with the parameter $\boldsymbol{\alpha}_j$ defined by the relative size of the cortical regions **V**. The SC between a target region and all source regions $\mathbf{a}_j$ (where a_{ij} is the number of of connections between target j and source i) is modelled by a multinomial distribution, where each of the total of N_j connections between the sources and target j has the probability distribution $\boldsymbol{\theta}_j^{diffusion}$. The generative model is thus defined by

$$\begin{aligned} \boldsymbol{\theta}_j^{diffusion} &\sim Dir(\kappa_j \boldsymbol{\alpha}_j), \qquad \alpha_{ij} = \frac{V_i}{\sum_{i' \neq j} V_{i'}} \\ \mathbf{a}_j &\sim Mult(\boldsymbol{\theta}_j^{diffusion}, N_j), \end{aligned} \tag{2}$$

where κ_j is a scaling factor specifying the confidence of the prior.

We learn κ_j by exploiting that the Dirichlet distribution is conjugate to the Multinomial distribution such that $\boldsymbol{\theta}_j^{diffusion}$ can be analytically marginalized:

$$p(\mathbf{a_j}|\kappa_j\boldsymbol{\alpha}_j) = \int p(\mathbf{a}_j \mid \boldsymbol{\theta}_j^{diffusion}) p(\boldsymbol{\theta}_j^{diffusion} \mid \kappa_j\boldsymbol{\alpha}_j) d\boldsymbol{\theta}_j^{diffusion}$$
$$= \frac{N_j!}{\prod_{i'\neq j} a_{i'j}!} \frac{B(\mathbf{a}_j + \kappa_j\boldsymbol{\alpha}_j)}{B(\kappa_j\boldsymbol{\alpha}_j)} \quad (5)$$

The value of κ_j is then found empirically by optimizing the log of this marginalized distribution, i.e. $\log(p(\mathbf{a}_j \mid \kappa_j\boldsymbol{\alpha}_j))$. In the optimization[1] κ_j is constrained to the interval $[0, \sum_{i'\neq j} a_{i'j}]$ such that κ_j always is positive and the prior never can have more influence than the diffusion data.

Using Bayes' theorem the posterior distribution of $\boldsymbol{\theta}_j^{diffusion}$ is then given by the Dirichlet distribution

$$p(\boldsymbol{\theta}_j^{diffusion}|\mathbf{a}_j, \kappa_j, \boldsymbol{\alpha}_j) = \frac{p(\mathbf{a}_j \mid \boldsymbol{\theta}_j^{diffusion}) p(\boldsymbol{\theta}_j^{diffusion} \mid \kappa_j\boldsymbol{\alpha}_j)}{\int p(\mathbf{a}_j \mid \boldsymbol{\theta}_j^{diffusion}) p(\boldsymbol{\theta}_j^{diffusion} \mid \kappa_j\boldsymbol{\alpha}_j) d\boldsymbol{\theta}_j^{diffusion}}$$
$$= Dir(\mathbf{a}_j + \kappa_j\boldsymbol{\alpha}_j) \quad (3)$$

From this distribution we will use the expected value of $\boldsymbol{\theta}_j^{diffusion}$ given by

$$< \boldsymbol{\theta}_j^{diffusion} >= w_j\mathbf{r}_j + (1 - w_j)\boldsymbol{\alpha}_j \quad (4)$$

as estimate of the relative SC probabilities, where

$$\alpha_{ij} = \frac{V_i}{\sum_{i'\neq j} V_{i'}}, \qquad r_{ij} = \frac{a_{ij}}{\sum_{i'\neq j} a_{i'j}},$$
$$w_j = \frac{\sum_{i'\neq j} a_{i'j}}{\sum_{i'\neq j}(a_{i'j}) + \kappa_j}, (1 - w_j) = \frac{\kappa_j}{\sum_{i'\neq j}(a_{i'j}) + \kappa_j}.$$

A three-factor repeated measures ANOVA with Bonferroni correction and Greenhouse-Geisser correction for sphericity was performed in SPSS 19, to investigate the effect of varying the b-value, spatial resolution and angular resolution as well as their interactions.

Sensitivity and specificity

Sensitivity, measures the fraction of true positives, i.e. the number of (binary) connections co-occurring in the tracer and tractography graphs divided by the total number of connections in the SC graph. Specificity, measures the fraction of true negatives, i.e. the

[1] Optimization was performed using the minimum bound optimization *fminbnd* in Matlab v. 8.5.1 (The MathWorks Inc., Natick, MA, 2000).

number of absent connections co-occurring in the tracer and tractography graphs divided by the total number of absent connections in the SC graph.

Results

Figure 1 shows a color-coded fractional anisotropy (FA)-map for different combinations of b-value, angular resolution and spatial resolution. Independent of b-value and directions, the overall anatomical structures that appears in high image resolution are also visible in the eight times lower image resolution. However, clearly even the larger tracts like corpus callosum does not appear to have the same spatial continuous outlined shape as in high resolution. In general, larger tracts appear discontinuous and is often only one voxel thick as seen for the corpus callosum. Therefore, anatomical features in the low resolution image suffers from severe partial volume effects (PVE) and the fine anatomical details visible at the eight times higher resolution are missing in the FA map. The effect of combining low angular resolution and high b-value makes the FA map appear very noisy compared to a FA map with lower b-value even when SNR is similar. The reason for the noise is that higher b-value makes the fiber profile sharper and the lack of angular resolution results in noisy fitting.

Network similarity measured with cross entropy

The cross entropy between the SC and tracer graphs, when using the WM seeding strategy, is reported in Figure 2. Generally, more directions consistently improve cross entropy (cross entropy decreases) between the graphs ($p=0.002$), suggesting that angular resolution is very important for the agreement between the SC graph and the tracer graph. Also, the interaction between the spatial and angular resolution is significant ($p=0.000$). The main effect of the b-value is not significant ($p=0.143$), but the interaction between the b-value and spatial resolution is ($p=0.001$). Increasing the streamline threshold increases the cross entropy systematically (hence lower network agreement) but it has minimal effect on the ranking of the graphs for any scan parameters (difference between the rows in Figure 2). Using the GM seeding strategy show similar overall performance and results, see Figure S1.

Interestingly, lower image resolution improves the cross entropy for any parameter configuration ($p=0.003$). Even for the combination of highest angular resolution (180 directions) and highest b-value ($b=7700$ s/mm²), the low image resolution based networks outperforms those generated from the high image resolution. As expected due to the small incision in the left hemisphere, the right hemisphere generally shows higher agreement with the tracer graph than the left hemisphere. The different nuances of the same color indicate left (dark) and right (bright) hemisphere, respectively. Note however, that the defect hemisphere show very good performance although connections in the occipital region have been compromised. The reason could be that the low image resolution results in such severe partial volume effects (PVE) that the tractography algorithm is able to track the reconstructed fiber orientations across the small incision in the brain. An explanation to the low resolution data performing better could be that fewer steps in the tractography is needed to connect two cortical regions, as the integration step length in the tractography is ¼ voxel size for both image resolutions. To rule out this explanation, graphs derived from both low and high resolution data with both small (0.125 mm) and large (0.25 mm) integration step length are compared for both WM and GM seeding (Figure S4). The result shows that the

cross entropy is almost unaffected by the integration step length for both image resolutions and both seeding strategies. Another possible explanation could be that the low resolution images is better because SNR is eight times higher. This is supported by the fact that more repetitions improve the cross entropy for high resolution data when only few directions are acquired. When performing GM seeding the same dependency on acquisition parameters like image resolution, angular resolution and b-value is observed (Figure S1). In summary, neither integration step length in the tractography (Figure S4) nor averaging acquisition repetitions (i.e. number of acquisitions) (Figure S2 and S3) changes the result that networks based on low image resolution are more in agreement with the tracer graph than the high resolution data sets.

Sensitivity and specificity

The intersection between the sensitivity and specificity indicates the optimal trade-off between the two. Figure 3 shows that for all combinations, except the combination of high b-value (b=7700 s/mm²) and low angular resolution (20 directions), the sensitivity/specificity trade-off is around 0.6. Minor increases are observed with increasing angular resolution. In contrast, the threshold has a great impact on the performance of sensitivity and sensitivity. A high threshold results in high specificity and low sensitivity, whereas a low threshold results in low specificity and high sensitivity, except for the combination of b=7700 s/mm² and low angular resolution (20 directions) that exhibit low sensitivity (<0.47) for any threshold. When increasing the angular resolution, a higher threshold is needed to obtain the optimal trade-off between sensitivity and specificity, but compared to WM seeding, a lower threshold is needed to obtain the optimal trade-off between sensitivity and specificity when using GM seeding (Figure S6).

We investigated how the number of initiated streamlines in the tractography affects the agreement with the tracer graph as this potentially impacts our results. To investigate the effect of the number of initiated streamlines, graphs generated using a fixed b-value of 4100 s/mm², 180 directions and a image resolution of 1.0 mm³ using different streamlines/voxel are compared using the sensitivity and specificity measures. Figure S5 shows the sensitivity and specificity as a function of threshold. The optimal trade-off between sensitivity and specificity (i.e. the intersection of the sensitivity and specificity curves) increases when going from 1 streamline/voxel to 10 streamlines/voxel, but is otherwise more or less constant. To obtain 100% sensitivity (for a threshold of 0%) at least 1000 streamlines/voxel are required.

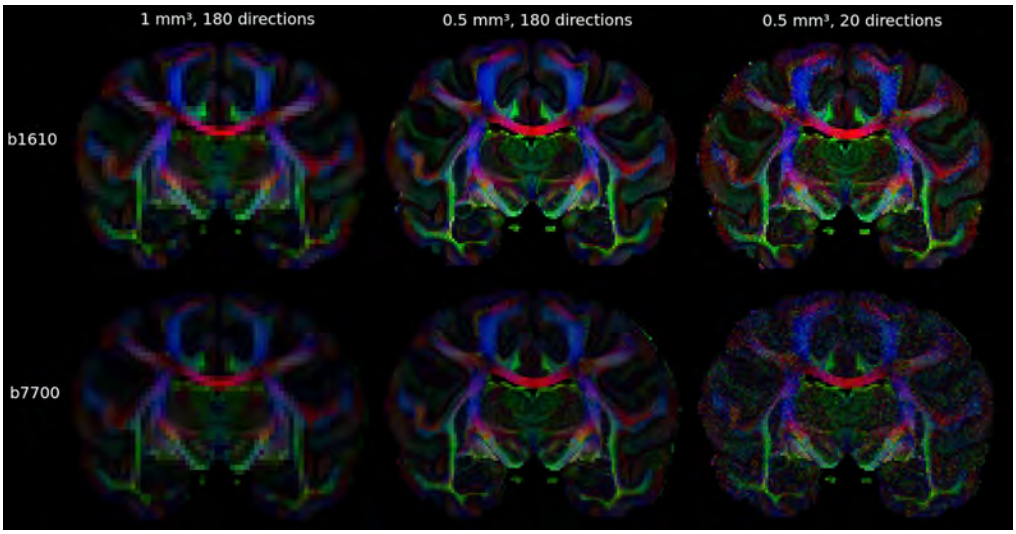

Figure 1: Color-coded fractional anisotropy (FA) map. The top row shows a b-value of 1610 s/mm² and the bottom row shows a b-value of 7700 s/mm². The left column shows low spatial resolution (1.0 mm³) and 180 directions, middle row shows high spatial resolution (0.5 mm³) and 180 directions and the right row shows high spatial resolution (0.5 mm³) and 20 directions.

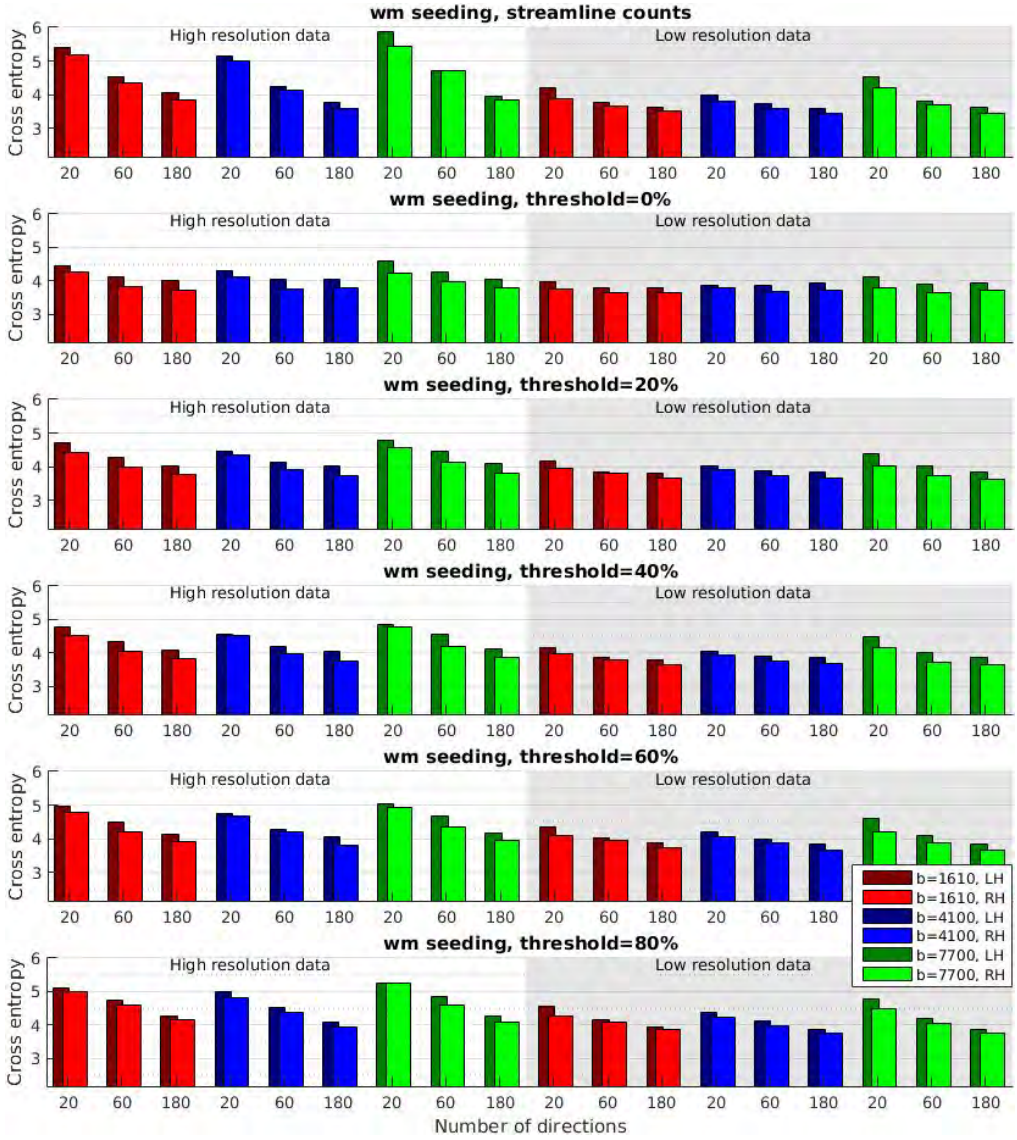

Figure 2: Cross entropy between tracer graph and diffusion graphs generated using different acquisition parameters and WM seeding. The different colors indicate the three different b-values with darker nuances indicating performance of the left hemisphere, whereas bright colors indicate the performance of the right (intact) hemisphere. The background indicates the image resolution, where high resolution is 0.5 mm³ and low resolution is 1.0 mm³. The different rows show different threshold levels. The top row shows the result of using the raw streamline counts as weights instead of binarizing the graphs using a threshold. The threshold is based on the maximum streamline count values in the graphs. The minimum value on the y-axis (2.1656) indicates the entropy of the tracer graph.

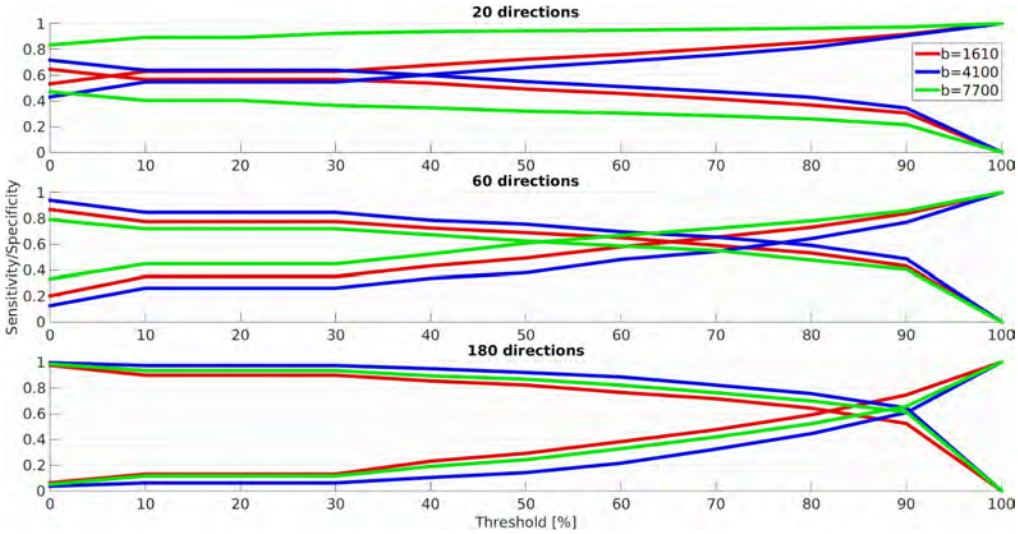

Figure 3: Sensitivity and specificity vs streamline count threshold in % of maximum count value for different combinations of b-value and angular resolution. Results are obtained using WM seeding on the high resolution (0.5 mm³) data. The rows show the three different angular resolutions and the different colors indicate different b-values. The point where two similar lines intersect indicates the optimal trade-off between sensitivity and specificity.

Discussion

Main findings

We have quantified how network graphs from tractography is highly dependent on chosen acquisition parameters, i.e. b-value, image- and angular resolution. Interestingly, previous studies focusing on the effect of model related parameter choices (i.e. fiber model, tractography algorithm, etc.) discuss that improved image- and angular resolution may improve the final connectome (Azadbakht et al. 2015; Donahue et al. 2016). In contradiction, we here find that networks generated from lower image resolution datasets better agree with ground truth than a data set with eight times higher image resolution. This is found for any combination of b-values, angular resolution and seeding strategy.

This suggests that the anatomical details available in the low resolution data is sufficiently to describe the connections in the tracer graph and the performance does not improve by adding information about finer anatomical details as available in higher spatial resolution (Figure 1). An improvement of the generated SC graphs may be obtained by combining multiple spatial resolutions, thereby utilize the information available on all scales as suggested in (Sotiropoulos et al. 2013).

A reason why angular resolution is important is that the SNR is very high in the low image resolution. The anatomical information in the low resolution images is the same as in high resolution, but the information in eight high resolution voxels is integrated into a single voxel in the low resolution data (Dyrby et al. 2014). Therefore in low spatial resolution SNR is the

key to disentangle the angular distribution from noise (Froeling et al. 2016). This means that when one wants to map a structural connectome, then one should use low spatial resolution to get a high SNR and acquire the data using a high angular resolution.

The impact of angular resolution and b-value

The general trend is that more directions are better if the optimal threshold is chosen, in agreement with (Jones 2004), that recommend to use as high angular resolution as time allows. The higher performance with high angular resolution can be due to higher SNR in data with more directions (Zhan et al. 2010). To eliminate this option, graphs generated using the average images of three repetitions of the 20 directions, two repetitions of 60 directions and 2 repetitions of 180 directions are compared to graphs generated using 20, 60 and 180 unique directions, see Figure S2 (WM seeding) and S3 (GM seeding). For high resolution data, the averaging of more repetitions, and hence improving SNR, increases the performance, but does not outperform the performance of graphs generated using unique gradient directions with similar SNR. For low resolution data the averaging of more repetitions has minimal influence on the result, whereas the acquisition of more unique directions significantly improves the result. This suggests that the low resolution data set is more or less saturated in good SNR and contains the necessary anatomical information which can be extracted with higher angular resolution. This further suggests that high image resolution is not needed to generate SC graphs that well corresponds to tracer data in the coarse resolution of the M132 parcellation.

From Figure 1, the data quality seems to improve only if both angular resolution and the b-value increase, suggesting that the data only benefit from higher angular resolution if detailed anatomical information exists, which is the case when using higher b-values. A possible explanation why higher b-values benefit more from increased angular resolution than low b-values, is that when increasing the b-value the estimated orientation distributions get more peaked and therefore more directions are needed to describe the distributions (Frank 2002; Frank 2001; Xie et al. 2015). When increasing the b-value, the number of measured compartments increases. To model the variety of compartments measured with high b-values more directions are needed. At lower b-values the uncertainties are larger and the estimated orientation distributions get broader, allowing the streamlines to take multiple different paths ending in different target locations. However, it should be noted that the interaction effect between b-value and angular resolution was not found to be significant ($p=0.097$).

The impact of step length and seeding strategy

We find that the integration step length in the tractography also have minimal influence on the result, in agreement with (Dauguet et al. 2007; Tournier et al. 2012) and Tournier et al. (Tournier et al. 2012) who recommends to use the largest step length that provides sufficient accuracy. Also, we find that seeding strategy has minimal impact on the network performance, in agreement with previous finding (Donahue et al. 2016), but in contradiction to (Buchanan et al. 2014). It is discussed if large tracts dominate the statistics when using WM seeding as they include more seed voxels compared to smaller tracts, whereas GM tractography only is initiated in the specific tracts of interest and independent of major tract

sizes (Jones 2010). Usually the connectivity graph is more sparse when using GM seeding compared to WM seeding. This means that lower thresholds are needed to ensure an optimal sensitivity/specificity trade-off (Figure S6). One might speculate that major tracts (due to volume) contribute more to the counts in the connectivity matrix than smaller tracts. In this study we did not investigate the specific tracts, but focused on the connectivity between cortical regions.

The impact of threshold

The sensitivity/specificity trade-off (where they intersect) is around 60-64%, independent of threshold, in agreement with other studies (Donahue et al. 2016). An exception is the combination of the lowest angular resolution and the highest b-value, where an optimal sensitivity/specificity trade-off cannot be reached. The reason is that the high b-value provides more angular information than can be captured with low angular resolution. In contrast, the optimal threshold to ensure optimal trade-off between sensitivity and specificity is very dependent on the data in question and depends on the number of streamlines, seeding strategy, b-value, image resolution and number of directions.

Other studies validating brain networks by comparing tracer and tractography graphs use accuracy (percentage of correctly determined binary connections) (Azadbakht et al. 2015), correlation between FLNe (fraction of labeled neurons extrinsic to the target region) and FSe (fraction of streamlines connecting two areas relative to the number of streamlines extrinsic to those areas) (Donahue et al. 2016) or between number of streamlines (NOS) and FLNe (van den Heuvel et al. 2015). Herein we use cross entropy in combination with sensitivity and specificity between FLNe counts and streamline counts normalized with the total number of streamlines reaching any source region from a given target, similar to the normalization of the FLNe counts. Cross entropy as a measure of similarity between the two graphs is very robust to the choice of threshold, as the ranking of the graphs is minimally influenced by the threshold. The cross entropy results in Figure 2 and Figure S1 suggest that a threshold of 0% is optimal for most combinations of parameters in contradiction to the results in Figure 3 which show that a relatively high threshold is needed to obtain optimal sensitivity/specificity trade-off, especially for high angular resolutions. Cross entropy uses all the information available in the graphs in contrast to sensitivity and specificity that only use the binary information whether a connection is present or not. Cross entropy is to some degree dependent on the number of initiated streamlines. If a large number of streamlines are initiated (e.g. 160,000/voxel) the cross entropy decreases with increasing threshold level until a point where too much information is removed by thresholding (results not shown).

Considerations/limitations

The analyses performed herein is limited by the coarse resolution of the M132 parcellation. The substantial subsampling of the tractography graph may limit the amount of information we can extract from the diffusion data, complicating appropriate comparison of different settings. This can also be an explanation of why graphs derived from low resolution images is in better agreement with the tracer graph than graphs derived from high resolution images, as the precise target location of a streamline may not be important as long as it is within the correct region of the atlas. Due to this large subsampling of the diffusion graphs to the size of the tracer graph, the information gained in the high resolution dataset compared to the low

resolution data set disappears. This limitation may be overcome by an even more comprehensive tracer graph, than the one provided by Markov et al. (Markov et al. 2014). It should however be noted that the tracer graph by Markov et al. is the most detailed tracer connectivity study in monkeys currently available. Due to differences in SNR, the initiated number of streamlines and the integration step lengths between the two spatial resolutions and between the two seeding strategies, complicate the direct comparison of the cross entropy scores. However, all settings benefit from higher angular resolution. In the cortical termination of a streamline, partial volume effects influence the point of termination and it may improve matter to correct the SC graphs for gyral crown biases (Van Essen et al. 2014) as done in (Donahue et al. 2016). Herein we have validated the impact of varying the acquisition parameters and we find a sensitivity/specificity trade-off approximately 5% lower than reported in (Donahue et al. 2016), suggesting that correcting for tractography biases improves the SC graph, but the acquisition parameters are likely to have even greater impact on the derived SC graph. Another consideration is whether to use the whole tracer target region as seed/target region in the tractography or only a sphere or gaussian around the injection site. In this study we use the whole area, as some target areas were not connected to anything, when using a sphere or gaussian around the injection site, when increasing the threshold.

Conclusion

The results presented herein show that the increased SNR obtained by repeated measurements of the diffusion encoding directions improve the performance of the tractography graphs derived from high resolution data, though not outperforming graphs from data with similar SNR and unique diffusion encoding directions. In contrast, the graphs derived from low resolution data does not show a performance increase by repeated measurements, but does benefit from acquiring more unique diffusion encoding directions. In conclusion, we find that low spatial resolution is sufficient to derive a SC network that is in agreement with the tracer graph with the coarse resolution of the M132 parcellation. We also find that angular resolution is important to disentangle the anatomical details, especially in low spatial resolution.

References

Ambrosen, K.S. et al., 2014. Nonparametric Bayesian clustering of structural whole brain connectivity in full image resolution. In *2014 International Workshop on Pattern Recognition in Neuroimaging*. Available at: http://dx.doi.org/10.1109/prni.2014.6858507.

Avants, B.B. et al., 2008. Symmetric diffeomorphic image registration with cross-correlation: evaluating automated labeling of elderly and neurodegenerative brain. *Medical image analysis*, 12(1), pp.26–41.

Azadbakht, H. et al., 2015. Validation of High-Resolution Tractography Against In Vivo Tracing in the Macaque Visual Cortex. *Cerebral cortex* , 25(11), pp.4299–4309.

Baldassano, C., Beck, D.M. & Fei-Fei, L., 2015. Parcellating connectivity in spatial maps. *PeerJ*, 3, p.e784.

Basser, P.J., Mattiello, J. & LeBihan, D., 1994. MR diffusion tensor spectroscopy and imaging. *Biophysical journal*, 66(1), pp.259–267.

Bastiani, M. et al., 2012. Human cortical connectome reconstruction from diffusion weighted MRI: the effect of tractography algorithm. *NeuroImage*, 62(3), pp.1732–1749.

Behrens, T.E.J., Woolrich, M.W., et al., 2003. Characterization and propagation of uncertainty in diffusion-weighted MR imaging. *Magnetic resonance in medicine: official journal of the Society of Magnetic Resonance in Medicine / Society of Magnetic Resonance in Medicine*, 50(5), pp.1077–1088.

Behrens, T.E.J., Johansen-Berg, H., et al., 2003. Non-invasive mapping of connections between human thalamus and cortex using diffusion imaging. *Nature neuroscience*, 6(7), pp.750–757.

Behrens, T.E.J. et al., 2007. Probabilistic diffusion tractography with multiple fibre orientations: What can we gain? *NeuroImage*, 34(1), pp.144–155.

Bennett, I.J. et al., 2010. Age-related differences in multiple measures of white matter integrity: A diffusion tensor imaging study of healthy aging. *Human brain mapping*, 31(3), pp.378–390.

Buchanan, C.R. et al., 2014. Test-retest reliability of structural brain networks from diffusion MRI. *NeuroImage*, 86, pp.231–243.

Calabrese, E. et al., 2015. A Diffusion MRI Tractography Connectome of the Mouse Brain and Comparison with Neuronal Tracer Data. *Cerebral cortex* , 25(11), pp.4628–4637.

Chen, L. & Wagenknecht, G., 2006. Automated topology correction for human brain segmentation. *Medical image computing and computer-assisted intervention: MICCAI ... International Conference on Medical Image Computing and Computer-Assisted Intervention*, 9(Pt 2), pp.316–323.

Collins, D.L. et al., 1994. Automatic 3D intersubject registration of MR volumetric data in standardized Talairach space. *Journal of computer assisted tomography*, 18(2), pp.192–205.

Collins, D.L. & Evans, A.C., 1997. Animal: Validation and Applications of Nonlinear Registration-Based Segmentation. *International Journal of Pattern Recognition and Artificial Intelligence*, 11(08), pp.1271–1294.

Coupe, P. et al., 2008. An optimized blockwise nonlocal means denoising filter for 3-D magnetic resonance images. *IEEE transactions on medical imaging*, 27(4), pp.425–441.

Dauguet, J. et al., 2007. Comparison of fiber tracts derived from in-vivo DTI tractography with 3D histological neural tract tracer reconstruction on a macaque brain. *NeuroImage*, 37(2), pp.530–538.

Donahue, C.J. et al., 2016. Using Diffusion Tractography to Predict Cortical Connection Strength and Distance: A Quantitative Comparison with Tracers in the Monkey. *The Journal of neuroscience: the official journal of the Society for Neuroscience*, 36(25), pp.6758–6770.

Dyrby, T.B. et al., 2011. An ex vivo imaging pipeline for producing high-quality and

high-resolution diffusion-weighted imaging datasets. *Human brain mapping*, 32(4), pp.544–563.

Dyrby, T.B. et al., 2014. Interpolation of diffusion weighted imaging datasets. *NeuroImage*, 103, pp.202–213.

Dyrby, T.B. et al., 2007. Validation of in vitro probabilistic tractography. *NeuroImage*, 37(4), pp.1267–1277.

Eskildsen, S.F. & Ostergaard, L.R., 2006. Active surface approach for extraction of the human cerebral cortex from MRI. *Medical image computing and computer-assisted intervention: MICCAI ... International Conference on Medical Image Computing and Computer-Assisted Intervention*, 9(Pt 2), pp.823–830.

Eskildsen, S.F. & Østergaard, L.R., 2008. Evaluation of Five Algorithms for Mapping Brain Cortical Surfaces. In *2008 XXI Brazilian Symposium on Computer Graphics and Image Processing*. Available at: http://dx.doi.org/10.1109/sibgrapi.2008.16.

Eskildsen, S.F. & Ostergaard, L.R., 2007. Quantitative comparison of two cortical surface extraction methods using MRI phantoms. *Medical image computing and computer-assisted intervention: MICCAI ... International Conference on Medical Image Computing and Computer-Assisted Intervention*, 10(Pt 1), pp.409–416.

Eskildsen, S.F., Uldahl, M. & Ostergaard, L.R., 2005. Extraction of the cerebral cortical boundaries from MRI for measurement of cortical thickness. In *Medical Imaging 2005: Image Processing*. Available at: http://dx.doi.org/10.1117/12.595145.

Fan, L. et al., 2016. The Human Brainnetome Atlas: A New Brain Atlas Based on Connectional Architecture. *Cerebral cortex* , 26(8), pp.3508–3526.

Fonov, V. et al., 2011. Unbiased average age-appropriate atlases for pediatric studies. *NeuroImage*, 54(1), pp.313–327.

Frank, L.R., 2001. Anisotropy in high angular resolution diffusion-weighted MRI. *Magnetic resonance in medicine: official journal of the Society of Magnetic Resonance in Medicine / Society of Magnetic Resonance in Medicine*, 45(6), pp.935–939.

Frank, L.R., 2002. Characterization of anisotropy in high angular resolution diffusion-weighted MRI. *Magnetic resonance in medicine: official journal of the Society of Magnetic Resonance in Medicine / Society of Magnetic Resonance in Medicine*, 47(6), pp.1083–1099.

Froeling, M. et al., 2016. “MASSIVE” Brain Dataset: Multiple Acquisitions for Standardization of Structural Imaging Validation and Evaluation. *Magnetic resonance in medicine: official journal of the Society of Magnetic Resonance in Medicine / Society of Magnetic Resonance in Medicine*. Available at: http://dx.doi.org/10.1002/mrm.26259.

Gigandet, X. et al., 2013. A connectome-based comparison of diffusion MRI schemes. *PloS one*, 8(9), p.e75061.

Gong, G. et al., 2009. Age- and Gender-Related Differences in the Cortical Anatomical Network. *Journal of Neuroscience*, 29(50), pp.15684–15693.

Hagmann, P., 2005. *From diffusion MRI to brain connectomics*. Institut de traitement des

signaux PROGRAMME DOCTORAL EN INFORMATIQUE ET COMMUNICATIONS POUR L'OBTENTION DU GRADE DE DOCTEUR ÈS SCIENCES PAR Docteur en médecine, Université de Lausanne.

van den Heuvel, M.P. et al., 2015. Comparison of diffusion tractography and tract-tracing measures of connectivity strength in rhesus macaque connectome. *Human brain mapping*, 36(8), pp.3064–3075.

Iturria-Medina, Y., 2013. Anatomical brain networks on the prediction of abnormal brain states. *Brain connectivity*, 3(1), pp.1–21.

Jahanshad, N. et al., 2015. Seemingly unrelated regression empowers detection of network failure in dementia. *Neurobiology of aging*, 36 Suppl 1, pp.S103–12.

Jbabdi, S. et al., 2013. Human and monkey ventral prefrontal fibers use the same organizational principles to reach their targets: tracing versus tractography. *The Journal of neuroscience: the official journal of the Society for Neuroscience*, 33(7), pp.3190–3201.

Jbabdi, S. et al., 2015. Measuring macroscopic brain connections in vivo. *Nature neuroscience*, 18(11), pp.1546–1555.

Jenkinson, M. et al., 2012. FSL. *NeuroImage*, 62(2), pp.782–790.

Jones, D.K., 2010. *Diffusion MRI*, Oxford University Press.

Jones, D.K., 2004. The effect of gradient sampling schemes on measures derived from diffusion tensor MRI: a Monte Carlo study. *Magnetic resonance in medicine: official journal of the Society of Magnetic Resonance in Medicine / Society of Magnetic Resonance in Medicine*, 51(4), pp.807–815.

Jones, D.K. & Cercignani, M., 2010. Twenty-five pitfalls in the analysis of diffusion MRI data. *NMR in biomedicine*, 23(7), pp.803–820.

Jones, D.K., Knösche, T.R. & Turner, R., 2013. White matter integrity, fiber count, and other fallacies: The do's and don'ts of diffusion MRI. *NeuroImage*, 73, pp.239–254.

Knösche, T.R. et al., 2015. Validation of tractography: Comparison with manganese tracing. *Human brain mapping*, 36(10), pp.4116–4134.

Kullback, S. & Leibler, R.A., 1951. On Information and Sufficiency. *Annals of Mathematical Statistics*, 22(1), pp.79–86.

Lebel, C. et al., 2008. Microstructural maturation of the human brain from childhood to adulthood. *NeuroImage*, 40(3), pp.1044–1055.

Le Bihan, D. & Johansen-Berg, H., 2012. Diffusion MRI at 25: exploring brain tissue structure and function. *NeuroImage*, 61(2), pp.324–341.

Lo, C.-Y. et al., 2010. Diffusion tensor tractography reveals abnormal topological organization in structural cortical networks in Alzheimer's disease. *The Journal of neuroscience: the official journal of the Society for Neuroscience*, 30(50), pp.16876–16885.

Maier-Hein, K. et al., 2016. Tractography-based connectomes are dominated by

false-positive connections. *bioRxiv*. Available at: http://dx.doi.org/10.1101/084137.

Markov, N.T. et al., 2014. A weighted and directed interareal connectivity matrix for macaque cerebral cortex. *Cerebral cortex* , 24(1), pp.17–36.

Markov, N.T. et al., 2011. Weight consistency specifies regularities of macaque cortical networks. *Cerebral cortex* , 21(6), pp.1254–1272.

Meskaldji, D.E. et al., 2013. Comparing connectomes across subjects and populations at different scales. *NeuroImage*, 80, pp.416–425.

Parisot, S. et al., 2016. Group-wise parcellation of the cortex through multi-scale spectral clustering. *NeuroImage*, 136, pp.68–83.

Pierpaoli, C. et al., 1996. Diffusion tensor MR imaging of the human brain. *Radiology*, 201(3), pp.637–648.

Qi, S. et al., 2015. The influence of construction methodology on structural brain network measures: A review. *Journal of neuroscience methods*, 253, pp.170–182.

de Reus, M.A. & van den Heuvel, M.P., 2013. Estimating false positives and negatives in brain networks. *NeuroImage*, 70, pp.402–409.

Robinson, E.C. et al., 2010. Identifying population differences in whole-brain structural networks: A machine learning approach. *NeuroImage*, 50(3), pp.910–919.

Scholz, J. et al., 2009. Training induces changes in white-matter architecture. *Nature neuroscience*, 12(11), pp.1370–1371.

Shannon, C.E., 1948. A Mathematical Theory of Communication. *Bell System Technical Journal*, 27(4), pp.623–656.

Shu, N. et al., 2011. Diffusion tensor tractography reveals disrupted topological efficiency in white matter structural networks in multiple sclerosis. *Cerebral cortex* , 21(11), pp.2565–2577.

Skudlarski, P. et al., 2010. Brain connectivity is not only lower but different in schizophrenia: a combined anatomical and functional approach. *Biological psychiatry*, 68(1), pp.61–69.

Sled, J.G., Zijdenbos, A.P. & Evans, A.C., 1998. A nonparametric method for automatic correction of intensity nonuniformity in MRI data. *IEEE transactions on medical imaging*, 17(1), pp.87–97.

Smith, S.M. et al., 2004. Advances in functional and structural MR image analysis and implementation as FSL. *NeuroImage*, 23 Suppl 1, pp.S208–19.

Sotiropoulos, S.N. et al., 2013. RubiX: combining spatial resolutions for Bayesian inference of crossing fibers in diffusion MRI. *IEEE transactions on medical imaging*, 32(6), pp.969–982.

Sporns, O., Tononi, G. & Kötter, R., 2005. The human connectome: A structural description of the human brain. *PLoS computational biology*, 1(4), p.e42.

Thomas, C. et al., 2014. Anatomical accuracy of brain connections derived from diffusion MRI tractography is inherently limited. *Proceedings of the National Academy of*

Sciences of the United States of America, 111(46), pp.16574–16579.

Tournier, J.-D., Calamante, F. & Connelly, A., 2012. MRtrix: Diffusion tractography in crossing fiber regions. *International journal of imaging systems and technology*, 22(1), pp.53–66.

Van Essen, D.C. et al., 2014. Mapping Connections in Humans and Non-Human Primates. In *Diffusion MRI*. pp. 337–358.

Van Essen, D.C., 2002. Surface-based atlases of cerebellar cortex in the human, macaque, and mouse. *Annals of the New York Academy of Sciences*, 978, pp.468–479.

Villalon-Reina, J.E. et al., 2016. Reliability of Structural Connectivity Examined with Four Different Diffusion Reconstruction Methods at Two Different Spatial and Angular Resolutions. In *Mathematics and Visualization*. pp. 219–231.

Vos, S.B. et al., 2016. Trade-off between angular and spatial resolutions in in vivo fiber tractography. *NeuroImage*, 129, pp.117–132.

Wen, W. et al., 2011. Discrete neuroanatomical networks are associated with specific cognitive abilities in old age. *The Journal of neuroscience: the official journal of the Society for Neuroscience*, 31(4), pp.1204–1212.

Wiegell, M.R. et al., 2003. Automatic segmentation of thalamic nuclei from diffusion tensor magnetic resonance imaging. *NeuroImage*, 19(2 Pt 1), pp.391–401.

Woolrich, M.W. et al., 2009. Bayesian analysis of neuroimaging data in FSL. *NeuroImage*, 45(1 Suppl), pp.S173–86.

Xie, S. et al., 2015. How does B-value affect HARDI reconstruction using clinical diffusion MRI data? *PloS one*, 10(3), p.e0120773.

Zalesky, A. et al., 2011. Disrupted axonal fiber connectivity in schizophrenia. *Biological psychiatry*, 69(1), pp.80–89.

Zhang, Y., Brady, M. & Smith, S., 2001. Segmentation of brain MR images through a hidden Markov random field model and the expectation-maximization algorithm. *IEEE transactions on medical imaging*, 20(1), pp.45–57.

Zhan, L. et al., 2010. How does angular resolution affect diffusion imaging measures? *NeuroImage*, 49(2), pp.1357–1371.

Zhan, L. et al., 2012. HOW DO SPATIAL AND ANGULAR RESOLUTION AFFECT BRAIN CONNECTIVITY MAPS FROM DIFFUSION MRI? *Proceedings / IEEE International Symposium on Biomedical Imaging: from nano to macro. IEEE International Symposium on Biomedical Imaging*, pp.1–6.

Supporting information (SI)

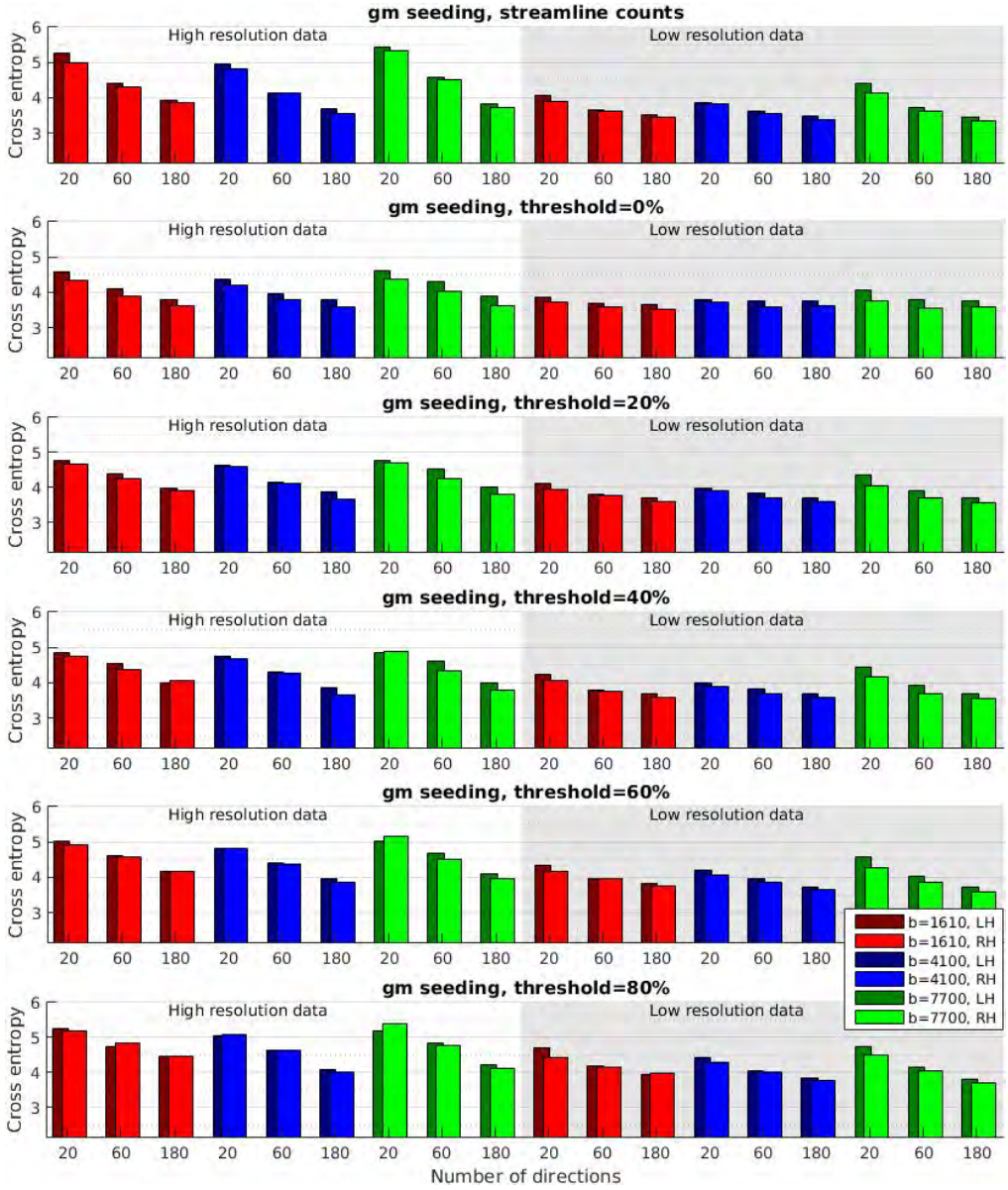

Figure S1: Cross entropy between tracer graph and diffusion graphs generated using different acquisition parameters and GM seeding. The different colors indicate the three different b-values. Darker nuances indicate performance of the left hemisphere, whereas bright colors indicate the right (intact) hemisphere. The background indicates the image resolution, where high resolution is 0.5 mm³ and low resolution is 1.0 mm³. The different rows show different threshold levels. The top row shows the result of using the raw streamline counts as weights instead of binarizing the graphs using a threshold. The

threshold is based on the maximum streamline count values in the graphs. The minimum value on the y-axis (2.1656) indicates the entropy of the tracer graph.

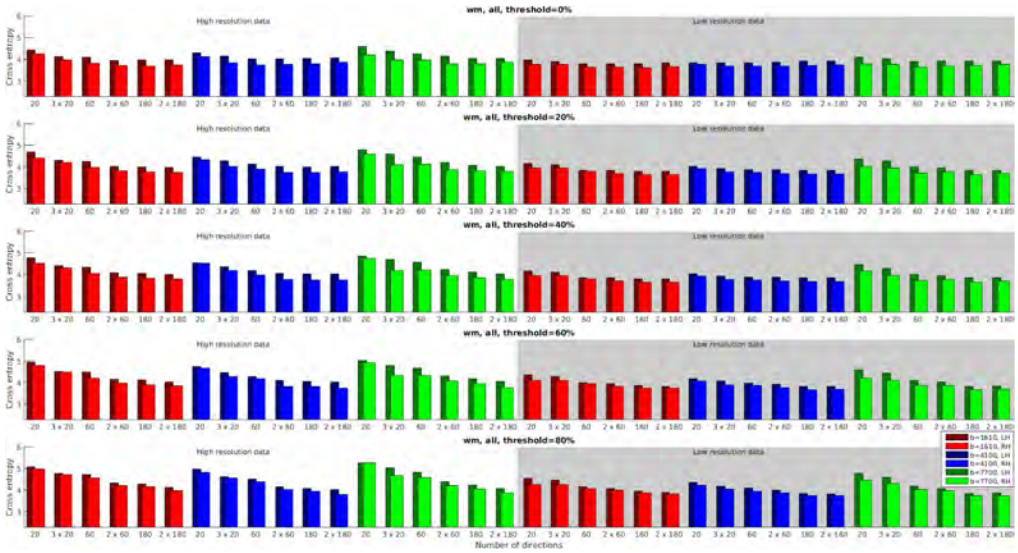

Figure S2: Cross entropy between tracer graph and diffusion graphs with same and different SNR. WM seeding. B-values are shown in different colors and spatial resolutions have different background colors. The labels on the x-axis show the angular resolution, where 3 x 20 means that the network is derived from the average of three acquisition repetitions with 20 directions.

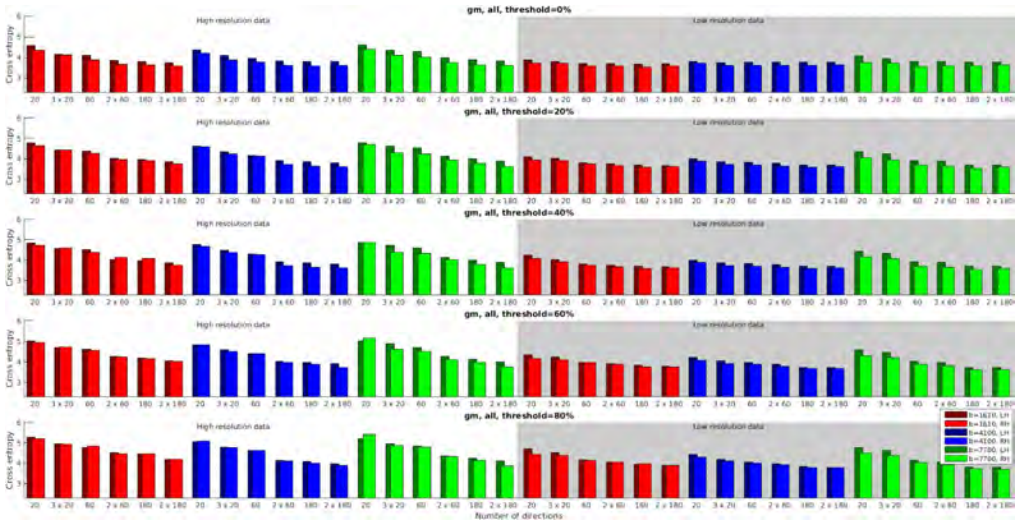

Figure S3: Cross entropy between tracer graph and diffusion graphs with same and different SNR. GM seeding. B-values are shown in different colors and spatial resolutions have different background colors. The labels on the x-axis show the angular resolution, where 3 x

20 means that the network is derived from the average of three acquisition repetitions with 20 directions.

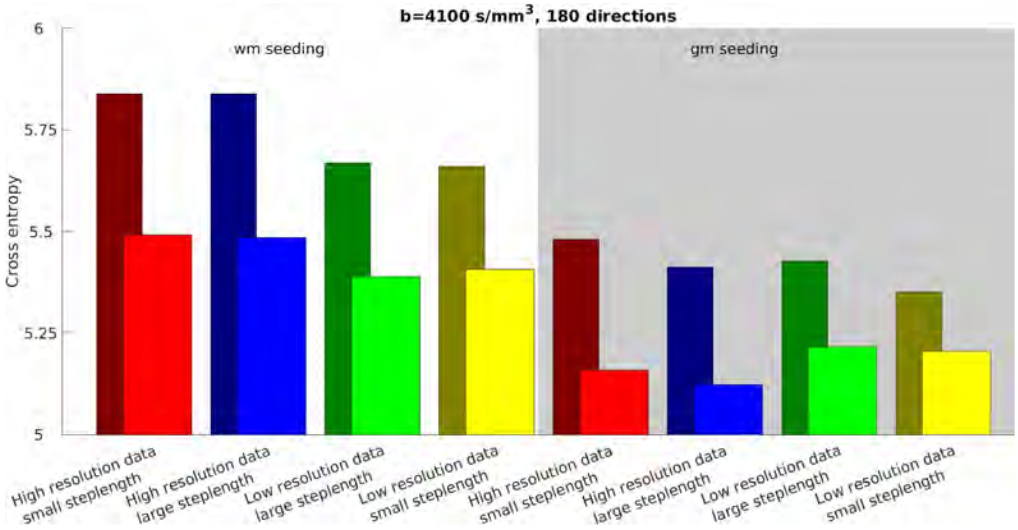

Figure S4: Cross entropy between tracer graph and diffusion graphs generated using different step lengths in the tractography. All the diffusion graphs are generated using a b-value of 4100s/mm³ and 180 directions. Note that the y-axis has changed compared to Figure 1.

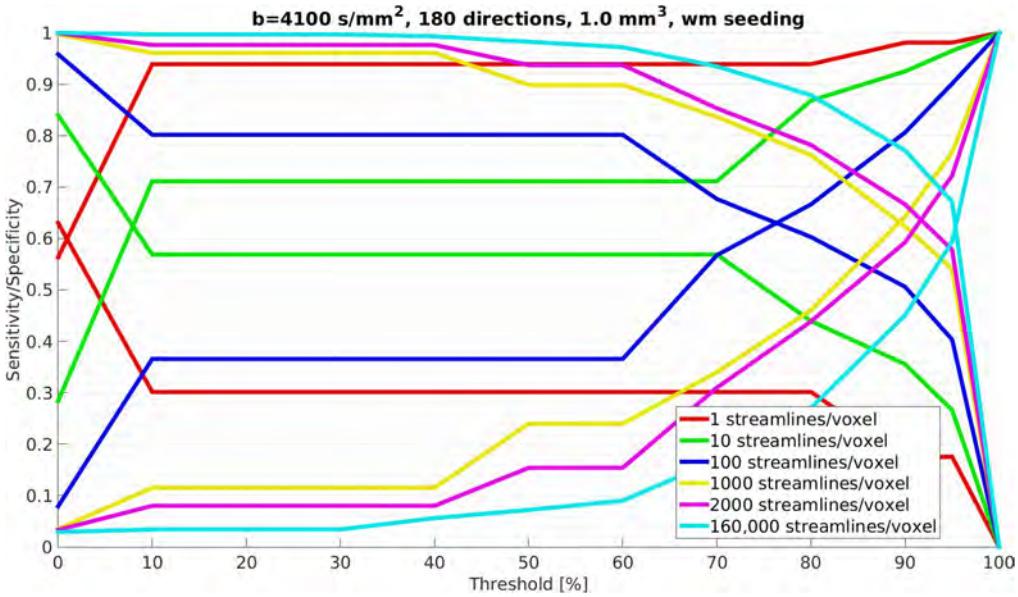

Figure S5: Sensitivity and specificity vs streamline count threshold in % of maximum count value for different number of streamlines. The data used in the analysis is acquired with a b-value of 4100 s/mm², 180 directions and a spatial resolution of 1.0 mm³.

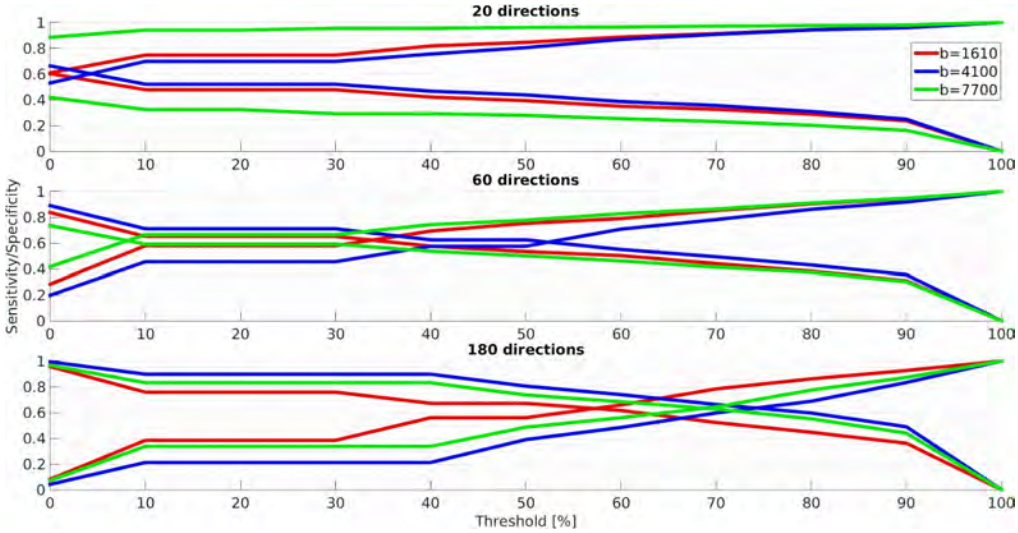

Figure S6: Sensitivity and specificity vs streamline count threshold in % of maximum count value for different combinations of b-value and number of directions. The graphs are derived from the data with high image resolution using GM seeding.